AD-A112 954 ARMY ELECTRONICS RESEARCH AND DEVELOPMENT COMMAND FO--ETC F/G 9/1
SUBTLE PERTURBATIONS AFFECTING QUARTZ RESONATORS USED FOR HIGH---ETC(U)
SEP 81 A BALLATO, T LUKASZEK, G J IAFRATE
UNCLASSIFIED DELET-TR-81-19 NL

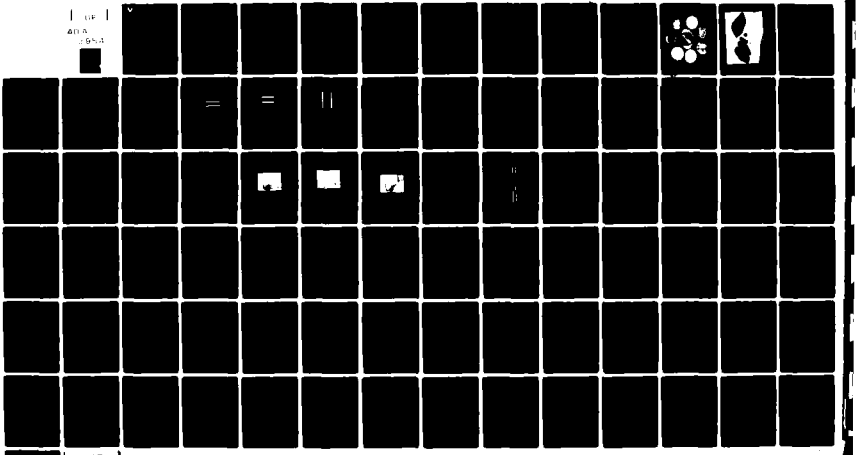

END
DATE FILMED
04-82
DTIC

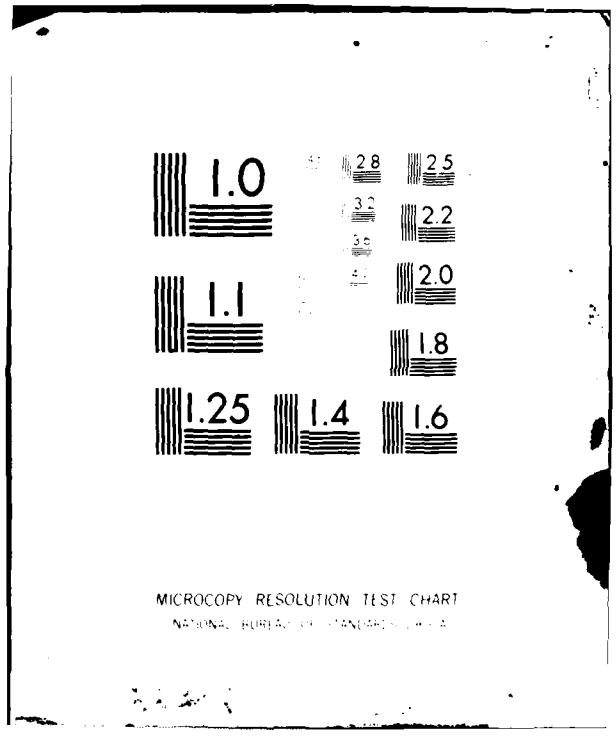
1.0
2.8
2.5
3.2
2.2
3.6
4.0
2.0
1.1
1.8
1.25
1.4
1.6
MICROCOPY RESOLUTION TEST CHART

(12)

RESEARCH AND DEVELOPMENT TECHNICAL REPORT

DELET-TR-81-19

SUBTLE PERTURBATIONS AFFECTING QUARTZ RESONATORS USED FOR HIGH-STABILITY APPLICATIONS

ARTHUR BALLATO
THEODORE LUKASZEK
GERALD J. IAFRATE
ELECTRONICS TECHNOLOGY & DEVICES LABORATORY

SEPTEMBER 1981

ERADCOM
US ARMY ELECTRONICS RESEARCH & DEVELOPMENT COMMAND
FORT MONMOUTH, NEW JERSEY 07703

NOTICES

Disclaimers

The citation of trade names and names of manufacturers in this report is not to be construed as official Government indorsement or approval of commercial products or services referenced herein.

Disposition

Destroy this report when it is no longer needed. Do not return it to the originator.

UNCLASSIFIED

SECURITY CLASSIFICATION OF THIS PAGE *(When Data Entered)*

REPORT DOCUMENTATION PAGE

READ INSTRUCTIONS BEFORE COMPLETING FORM

1. REPORT NUMBER: DELET-TR-81 -19	2. GOVT ACCESSION NO.
3. RECIPIENT'S CATALOG NUMBER:	
4. TITLE *(and Subtitle)*: Subtle Perturbations Affecting Quartz Resonators Used for High-Stability Applications	5. TYPE OF REPORT & PERIOD COVERED: Technical Report
6. PERFORMING ORG. REPORT NUMBER:	
7. AUTHOR(s): Arthur Ballato, Theodore Lukaszek, and Gerald J. Iafrate	8. CONTRACT OR GRANT NUMBER(s):
9. PERFORMING ORGANIZATION NAME AND ADDRESS: US Army Electronics Technology & Devices Laboratory, (ERADCOM) Ft. Monmouth, NJ 07703 DELET-MA	10. PROGRAM ELEMENT, PROJECT, TASK AREA & WORK UNIT NUMBERS: 1L1 62705 AH94 09 011
11. CONTROLLING OFFICE NAME AND ADDRESS: US Army Electronics Research & Development Command, Fort Monmouth, NJ 07703 DELET-MA	12. REPORT DATE: September 1981 13. NUMBER OF PAGES: 75
14. MONITORING AGENCY NAME & ADDRESS *(if different from Controlling Office)*:	15. SECURITY CLASS. *(of this report)*: UNCLASSIFIED 15a. DECLASSIFICATION/DOWNGRADING SCHEDULE

16. DISTRIBUTION STATEMENT *(of this Report)*

Approved for public release; distribution unlimited.

17. DISTRIBUTION STATEMENT *(of the abstract entered in Block 20, if different from Report)*

18. SUPPLEMENTARY NOTES

Key Words (continued)

Acceleration Effects
Vibration Effects
Quartz Resonators
Twinning
Electrode Stresses
Acoustic Viscosity

19. KEY WORDS *(Continue on reverse side if necessary and identify by block number)*

Crystal resonators	AT-cut quartz	Acoustic Waves
Crystal oscillators	Quartz crystals	Bulk Acoustic Waves
Piezoelectric crystals	Frequency control	Surface Acoustic Waves
Piezoelectric vibrators	Frequency-Temperature Characteristics	Doubly Rotated Crystals
		Equivalent Networks

20. ABSTRACT *(Continue on reverse side if necessary and identify by block number)*

The quest for high stability crystal resonators for advanced frequency control applications has led very recently to a number of far-reaching developments. As the level of frequency stability has improved over the years, various factors that were once imperceptible have become nonnegligible, and their influences have had to be eliminated, reduced, or compensated. At present the most obvious contributors to resonator performance have been enumerated. It is important to continue to catalog less obvious effects, and to evaluate critically at what level their influences make an appearance in the error budget of the (over)

DD FORM 1 JAN 73 1473 EDITION OF 1 NOV 65 IS OBSOLETE

UNCLASSIFIED

SECURITY CLASSIFICATION OF THIS PAGE *(When Data Entered)*

Abstract (cont)

resonator.

We consider a number of influences that are more-or-less "subtle". Each is examined to see what contribution it makes to resonator performance. It is apparent that some have to be taken into account in present-day applications; others may become inportant as future stability specifications become even more stringent.

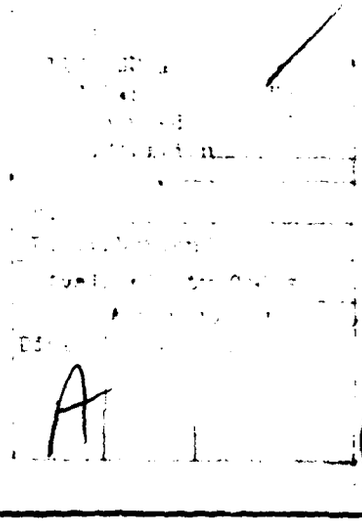

CONTENTS

FIGURES:

INTRODUCTION

The year 1980 marks the centenary of the discovery of piezoelectricity by the brothers Curie, and the fifty-ninth year of the quartz oscillator.[1]* The past thirty years or so have seen the development of cultured quartz from coin-sized pieces, shown in Fig. 1, to large, multi-kilogram crystals that constitute the bulk of the usage today (Fig. 2). Since the introduction of the quartz crystal-controlled oscillator by Cady, each decade of time has seen approximately one order of magnitude frequency stability improvement. Surrounding the development of high-stability oscillators incorporating crystal vibrator control has been the on-going interplay between improvements in resonator technology and causes of ever-smaller perturbations in resonator frequency and equivalent circuit parameters.[1-42]* Progress in timekeeping is shown on a broad time scale in Fig. 3, and a comparison of crystal resonator performance with atomic and molecular frequency standards is shown in Fig. 4; both Figures are adapted from Reference 2.* Further improvements will depend upon less-obvious factors than have been considered to date. This technical report treats a number of such topics.

MAGNETIC FIELDS

Quartz, and other high purity dielectric crystals, can be considered to be nonmagnetic for our purposes here. A vibrating crystal with metallic, nonmagnetic electrodes is, however, affected by external magnetic fields. Eddy currents are produced in the electrodes by their motions in the fields; these change the critical frequencies of the vibrator, and lower its Q. The situation considered is that of a resonator vibrating in a pure shear mode with applied static magnetic field parallel to plate thickness as depicted in Fig. 5. The resonator leads are attached to an active network comprising the remainder of the oscillator, and the combination adjusted in frequency so that the vibrator operates at zero reactance at all times.

For a pure shear mode, the retarding force density at the plate surfaces is

$$- j \omega \sigma B^2 u, \tag{1}$$

with σ the electrical conductivity of the electrode, and u the mechanical displacement at the surfaces. Electrodes of thickness h' will produce resistances of

$$R = A B^2 h' \tag{2}$$

for areas of value A. Using conventional notation[3]*, this leads to an expression for the imput admittance of the single mode vibrator, including the effects of electrode inertia[4]* :

---

*See list of references beginning on page 72.

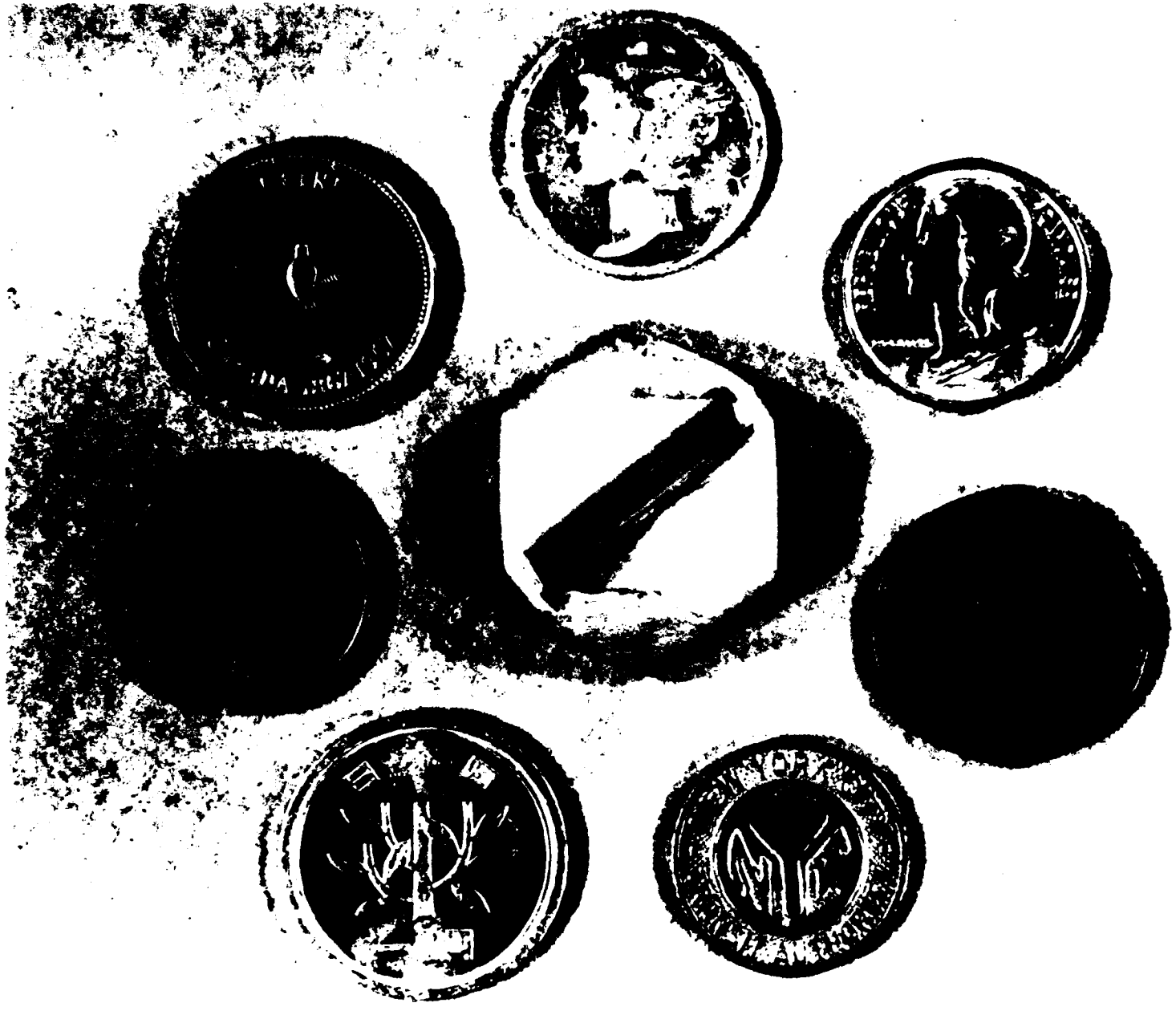

FIGURE 1. Early Example of Quartz Synthesis

FIGURE 2. Examples of Modern Quartz Synthesis

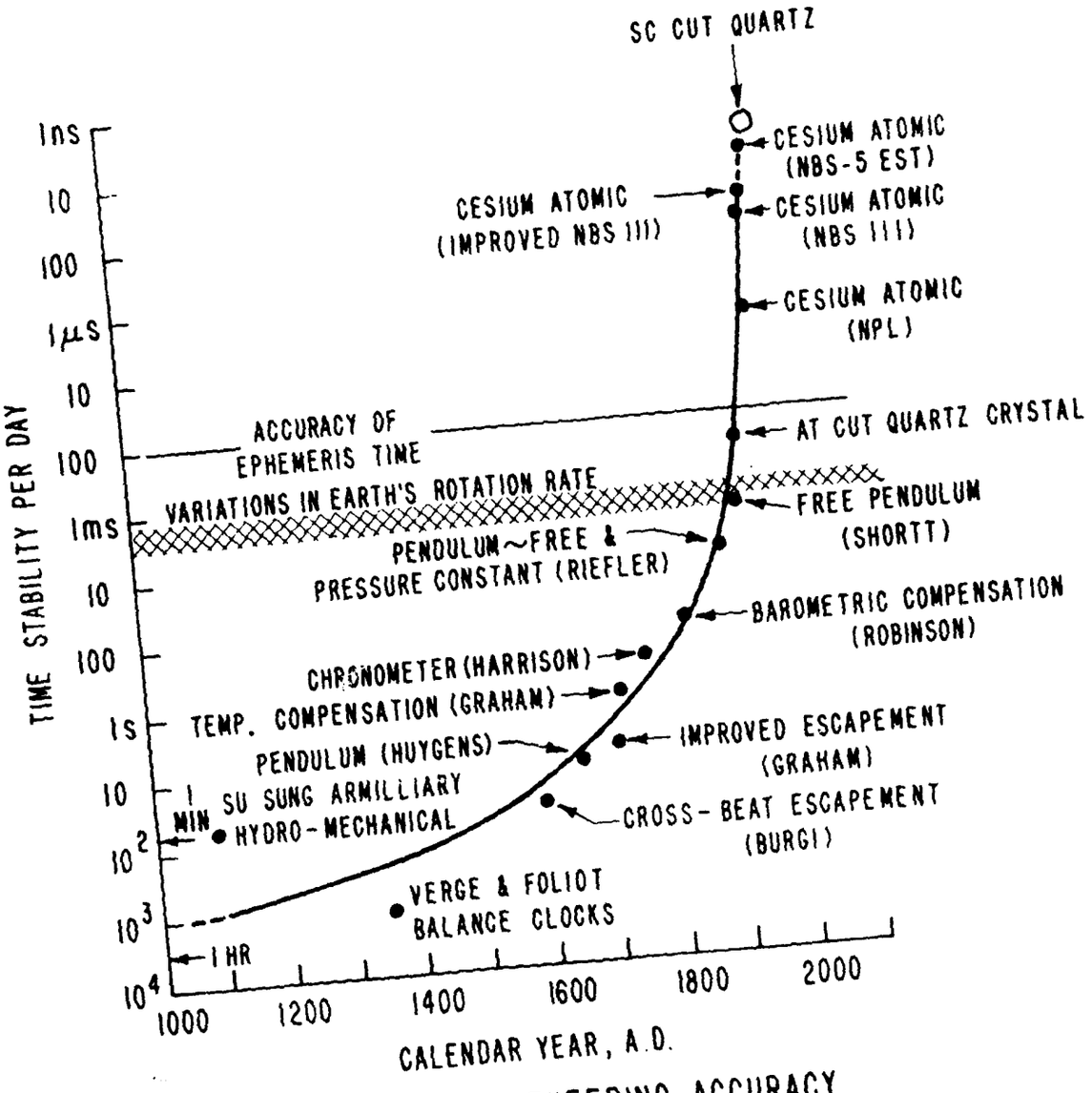

FIGURE 3. PROGRESS IN TIMEKEEPING ACCURACY

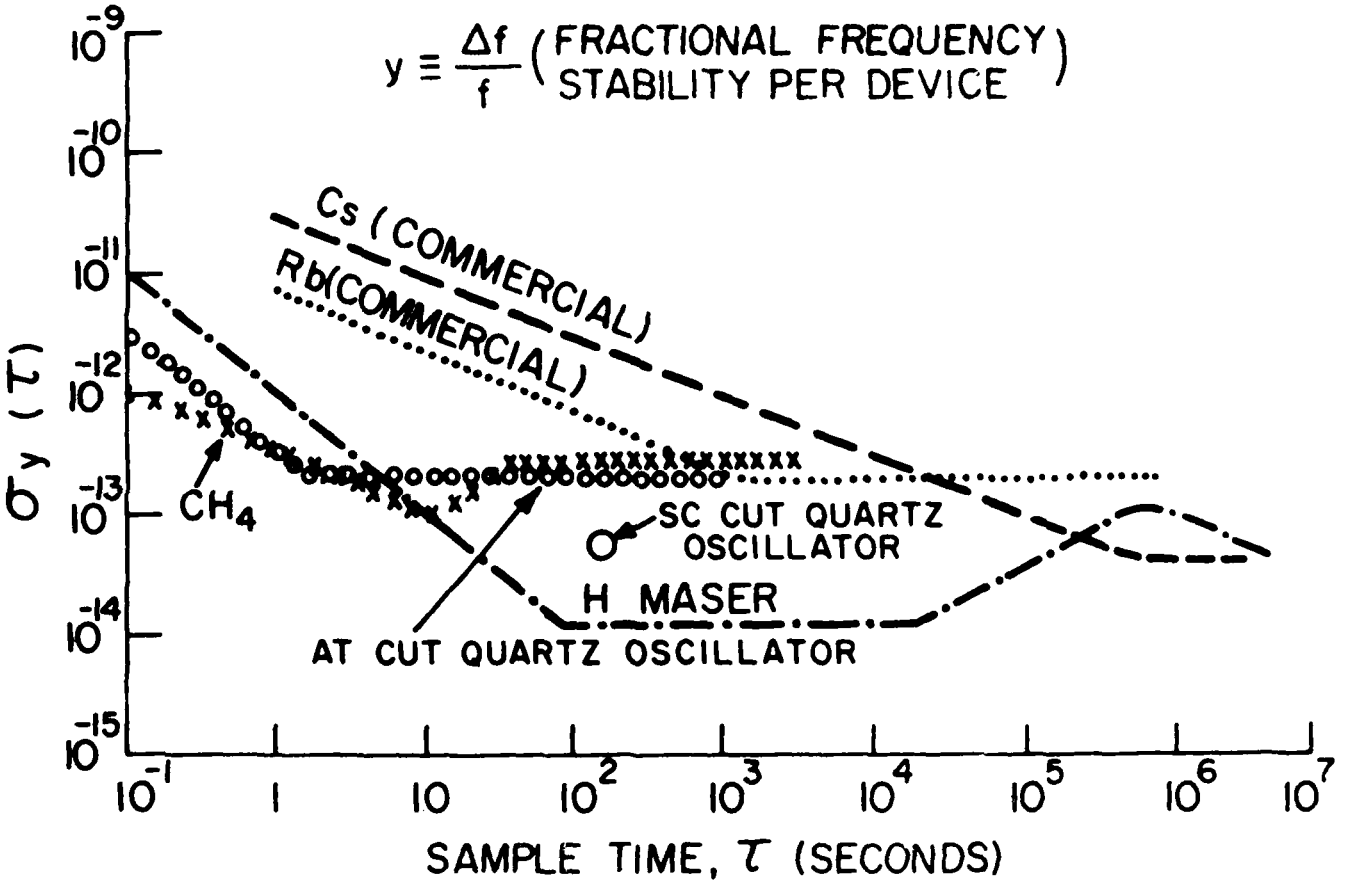

FIGURE 4. FRACTIONAL FREQUENCY STABILITY OF SEVERAL TYPES OF OSCILLATORS AS FUNCTION OF SAMPLE TIME.

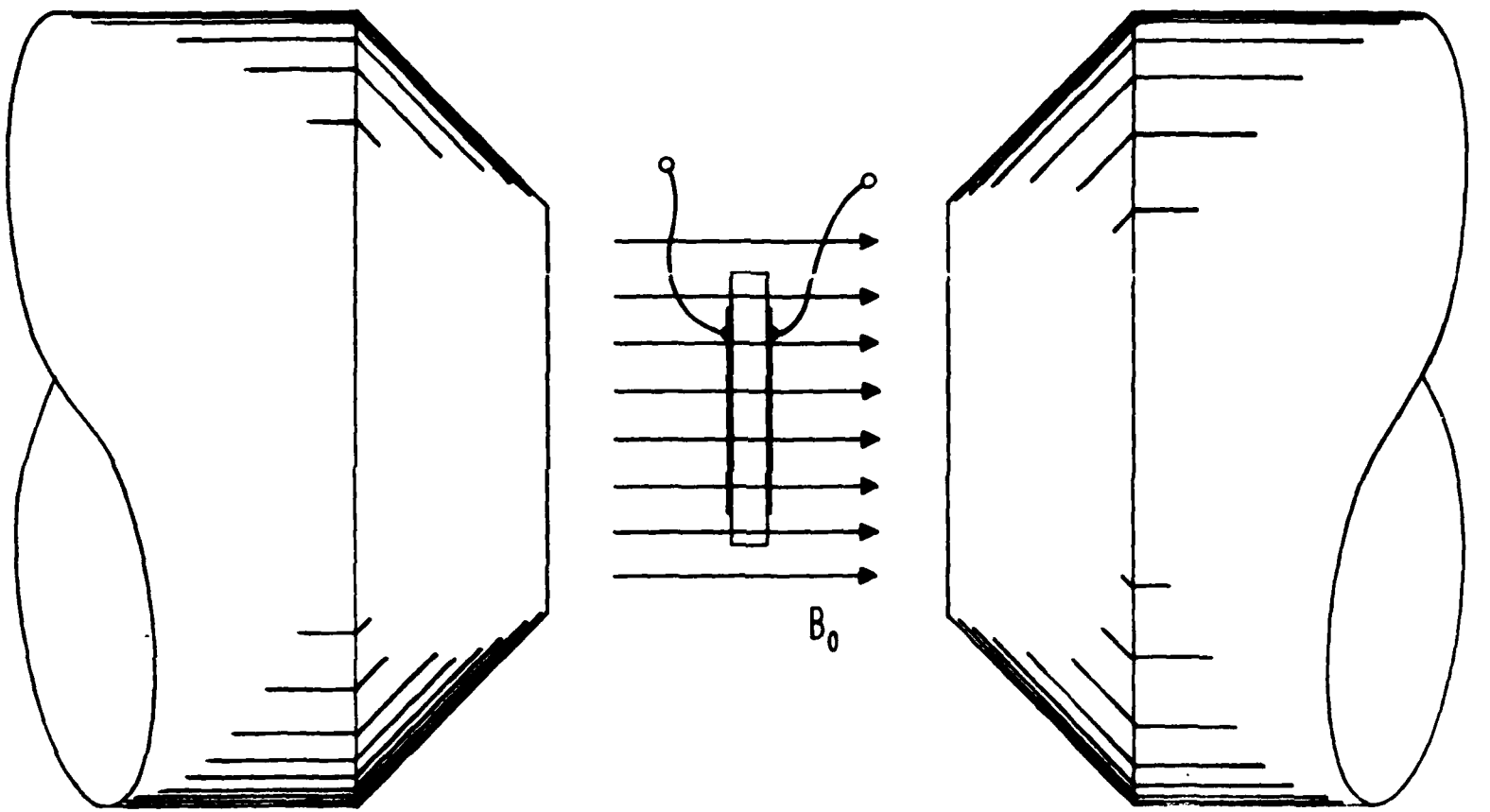

FIGURE 5. CRYSTAL RESONATOR IN MAGNETIC FIELD

$$Y_{in} = j\omega C_2 + j\omega C_0 \cdot \{(X/(k^2 \tan X) - 1 - X^2 \mu/k^2) + (jXRY_0/k^2)\}^{-1}. \quad (3)$$

Resonance and antiresonance frequencies are determined from the zeros of the susceptance function as the roots of

$$(X-(k^2 + \mu X^2) \tan X) \cdot (1- \mu X \tan X) + X \cdot (R Y_0)^2 \cdot \tan^2 X = 0. \quad (4)$$

When R=0, the first expression in brackets yields the condition for resonance, and the second that for antiresonance. From the expression for Y_{in} the network in Fig. 6 is obtained, with the electrode inertia represented by the inductances

$$L_1 = L_2 = L = \rho h \mu A. \quad (5)$$

The network components are labeled with their physically corresponding effects. When R is not zero, the inductances are replaced by series R-L combinations, and when electrode mass-loading is neglected, the circuit appears as given in Fig. 7. Figure 8 is the bisected version of Fig. 7 with massless electrodes (μ=0).

Departures from the resonance frequency as function of R are found by perturbation, with RY_0 the small parameter. The expression for frequency shift is

$$\Delta f/f \simeq - (2/\pi)^2 (RY_0)^2, \quad (6)$$

$$\text{with } RY_0 = \sigma h^2 B^2 / (\rho v), \quad (7)$$

ρ the quartz mass density, and v the acoustic velocity of the mode in question. It is seen from (6) and (7) that the frequency shift is quartic in the magnetic field strength. Figure 9 gives frequency shift values for an AT cut having 10,000 Å copper electrodes; only for fields about ten thousand times larger than that of the earth's (the first entry) is the effect perceptible.

This analysis has been extended to the multimode case, and to the situation of a lateral magnetic field, with corresponding network representations.[4]

RESONATOR ASYMMETRIES

In treatments of resonator electroding, it is usually tacitly assumed that both electrodes are of equal size and thickness. The practical reality is usually just the opposite. It is very difficult to guarantee that the thicknesses are equal in the first place; to make matters worse, final frequency adustment is usually made with a burst of material applied to a

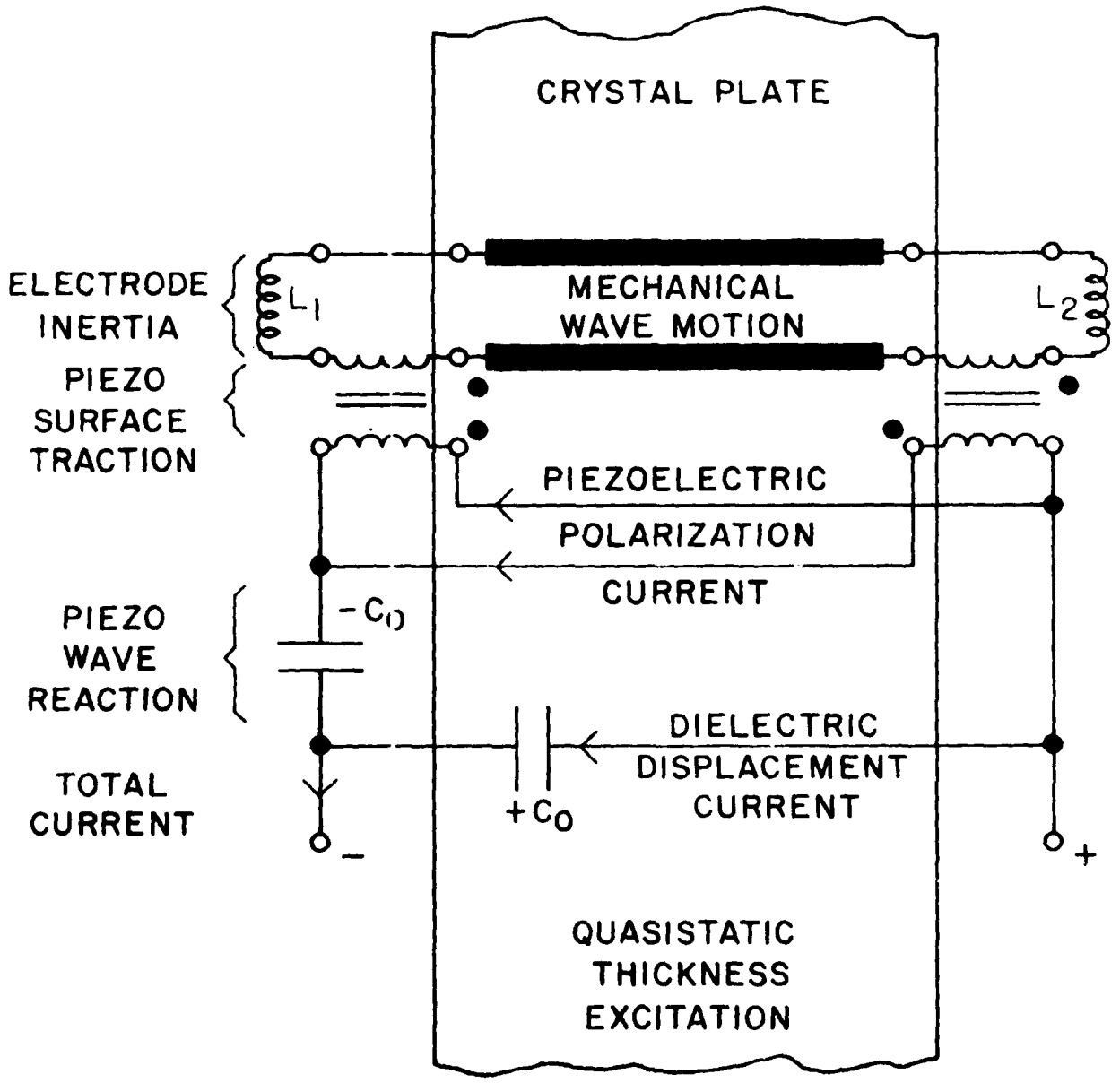

FIGURE 6. Analog Network of Resonator with Electrode Imbalance

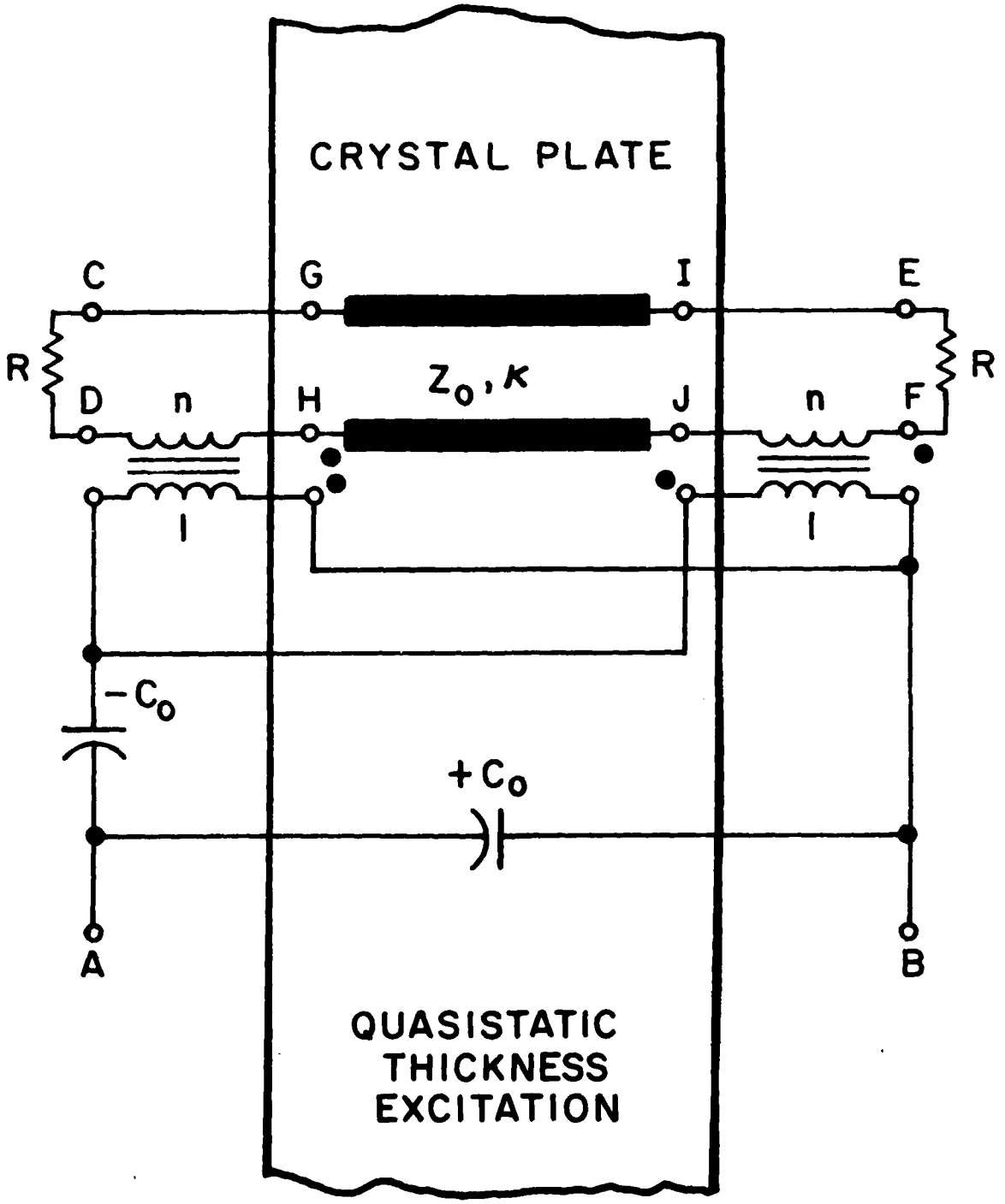

FIGURE 7. Analog Network of Resonator in Magnetic Field

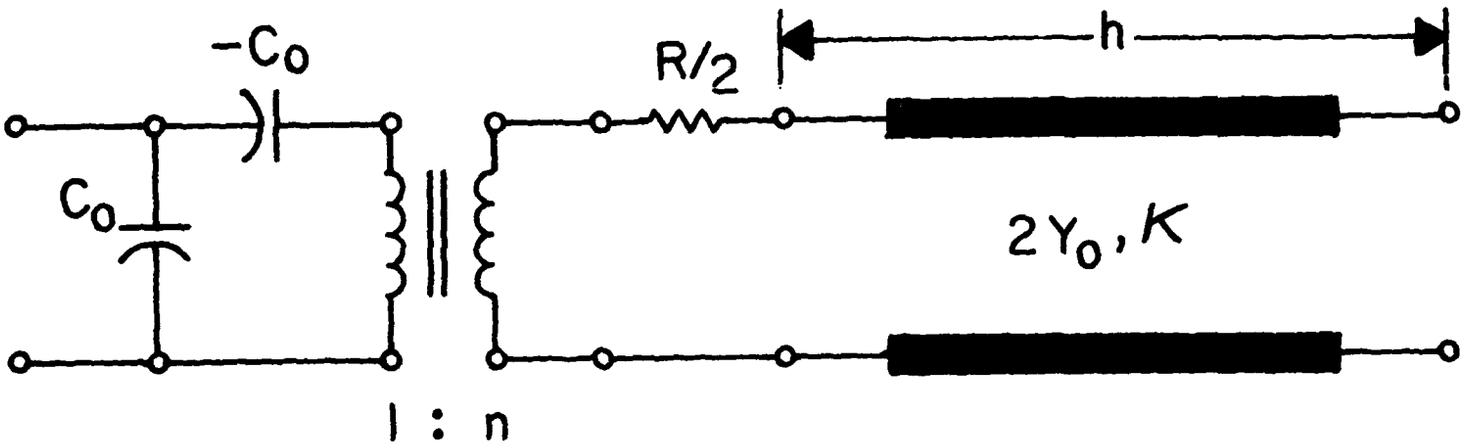

FIGURE 8. Bisected Analog Network

$$\Delta F/F \simeq -(\tfrac{2}{\pi})2*R^2\gamma_0^2$$

$$R\gamma_0 = \sigma h' B^2/(\rho v)$$

B		ΔF/F	H	
TESLA	KILO-GAUSS	AT CUT 1μM Cu ELECTRODES	AMPERE/METER	KILO-OERSTED
5.8 (-5)	0.58 (-3)	-2.2 (-28)	46.2	0.58 (-3)
0.1	1	-1.9 (-15)	7.9 (+4)	1
0.3	3	-1.5 (-13)	2.4 (+5)	3
1	10	-1.9 (-11)	7.9 (+5)	10
3	30	-1.5 (-9)	2.4 (+6)	30

FIGURE 9. Frequency Shifts Due to Magnetic Fields

single side. Add to this situation the facts that registration of both electrodes is never perfect, that the electrode tabs are asymmetrically disposed, and that sometimes a larger electrode is used on one side to improve statistical uniformity of the motional capacitance by compensating for misregistration, then it is seen that symmetry of the plate resonator about the mid-plane is seldom, if ever, achieved.

The single-mode case is treated, by way of example, for a simple electrode mass imbalance in the one-dimensional approximation. The equivalent network is that of Fig. 6 with the mechanical transmission line ports attached to unequal transmission lines representing the thick electrodes. When the electrodes are thin enough for propagation of the acoustic waves within the electrodes to be neglected, the transmission lines are replaced with lumped inductances; the mass imbalance results in unequal inductance values L_1 and L_2, as shown, and prevents the network from being bisected, as in Fig. 8. When bisection can take place, the transmission line representing the crystal plate of thickness 2h is replaced by one of half this value and the construction for the critical frequencies is that given in Fig. 10; the formulas are those of the bracketed terms in (4) separately set to zero. Figure 11 gives the normalized frequency variable

$$X_{RO}^{(M)} = (\pi/2)\ (f_{RO}^{(M)}/f_{AO}^{(1)})$$

versus piezoelectric coupling k for the first three harmonics M=1, 3, and 5. An AT-cut resonator with symmetrical electrodes of equal thickness produced the mode spectrograph at the top of Fig. 12. Strong responses are found at the odd harmonics, and nothing is visible at the even harmonics.

It is appropriate now to quote from Cady[1], p. 308:

> "There are circumstances under which a plate may conceivably vibrate in a thickness mode at or close to an even harmonic frequency. The shape, size and location of the electrodes may be such as to produce a driving field in the plate that varies in the direction of the thickness. Or the plate may be twinned or have other defects such that the excitation is not uniform. Finally, the plate may be in contact with an electrode of considerable mass, so that in effect one has a composite resonator."

When the electrodes are of unequal mass, and circuit bisection is not possible, the construction becomes that of Fig. 13, where the critical frequencies are determined by intersection with a tangent function of argument 2X instead of X. The expression for input impedance is

$$Z_{in} = (1/j\omega C_o) \cdot \{1 - \frac{k^2\ (\tan X/X)}{\left((1-\bar{\mu}X\ \tan X) + \frac{\Delta^2 X^2}{(1+\bar{\mu}X\ \cot X)}\right)}\}, \qquad (8)$$

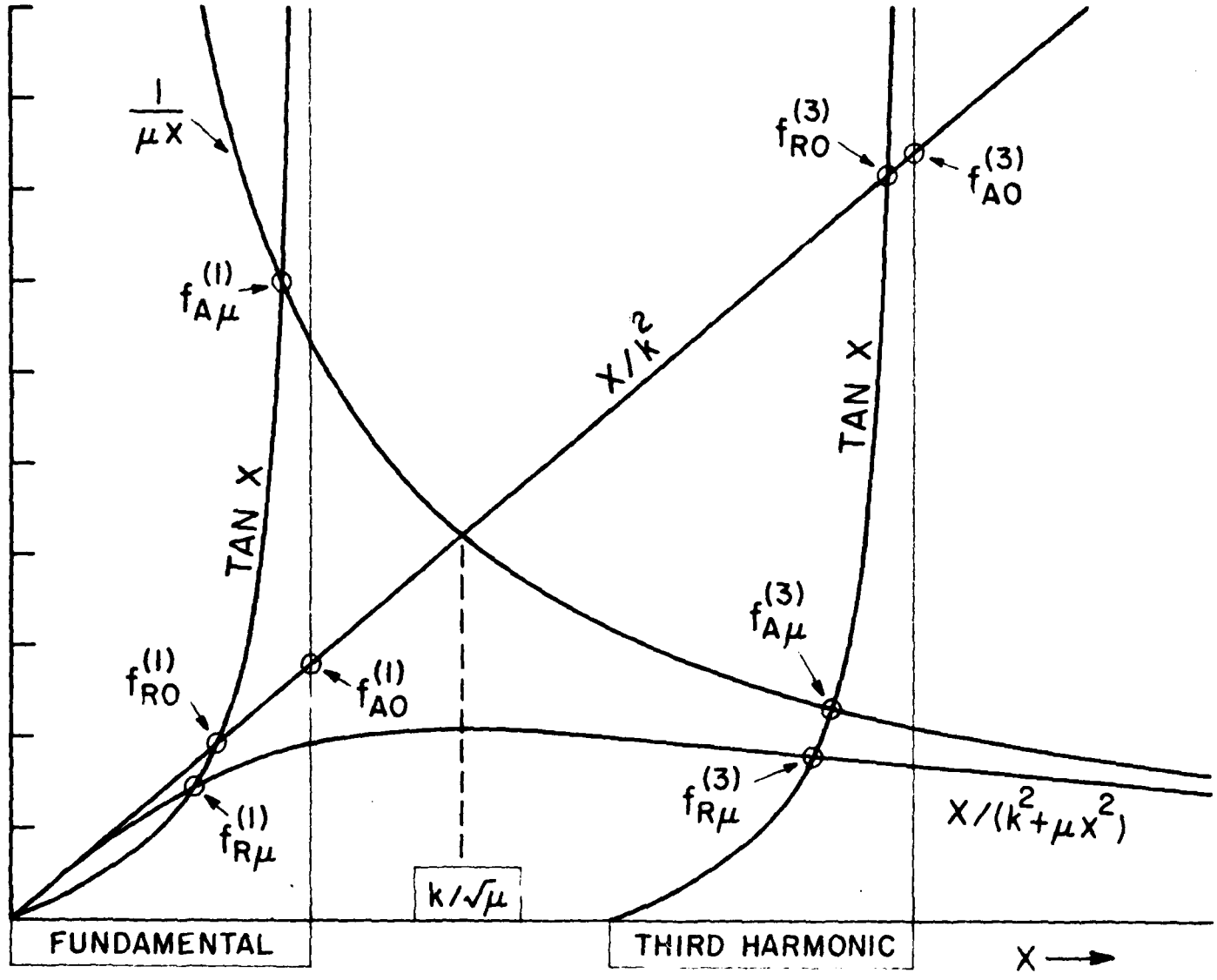

FIGURE 10. Construction for Resonance and Antiresonance Frequencies

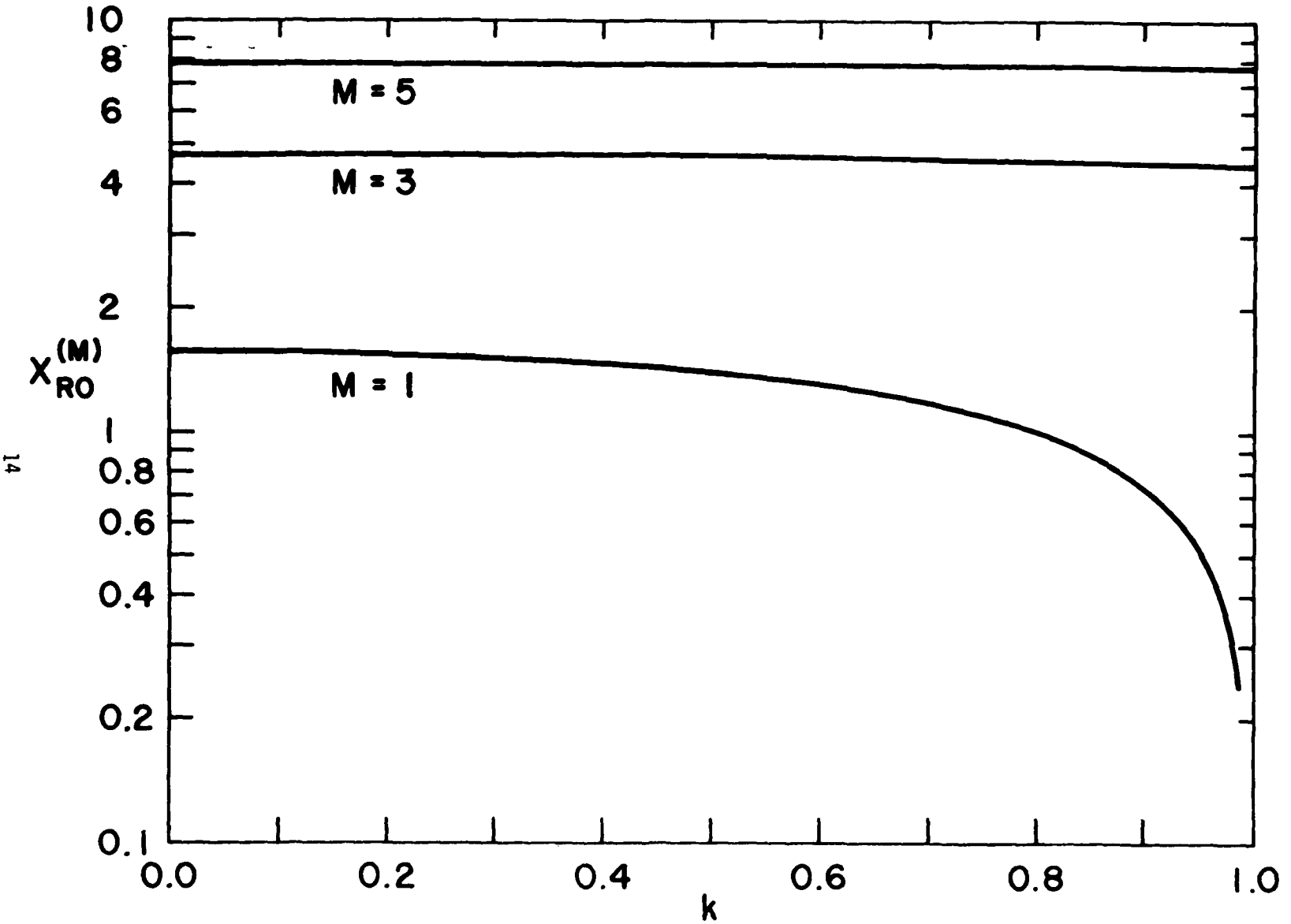

FIGURE 11. Normalized Resonance Frequency versus Coupling

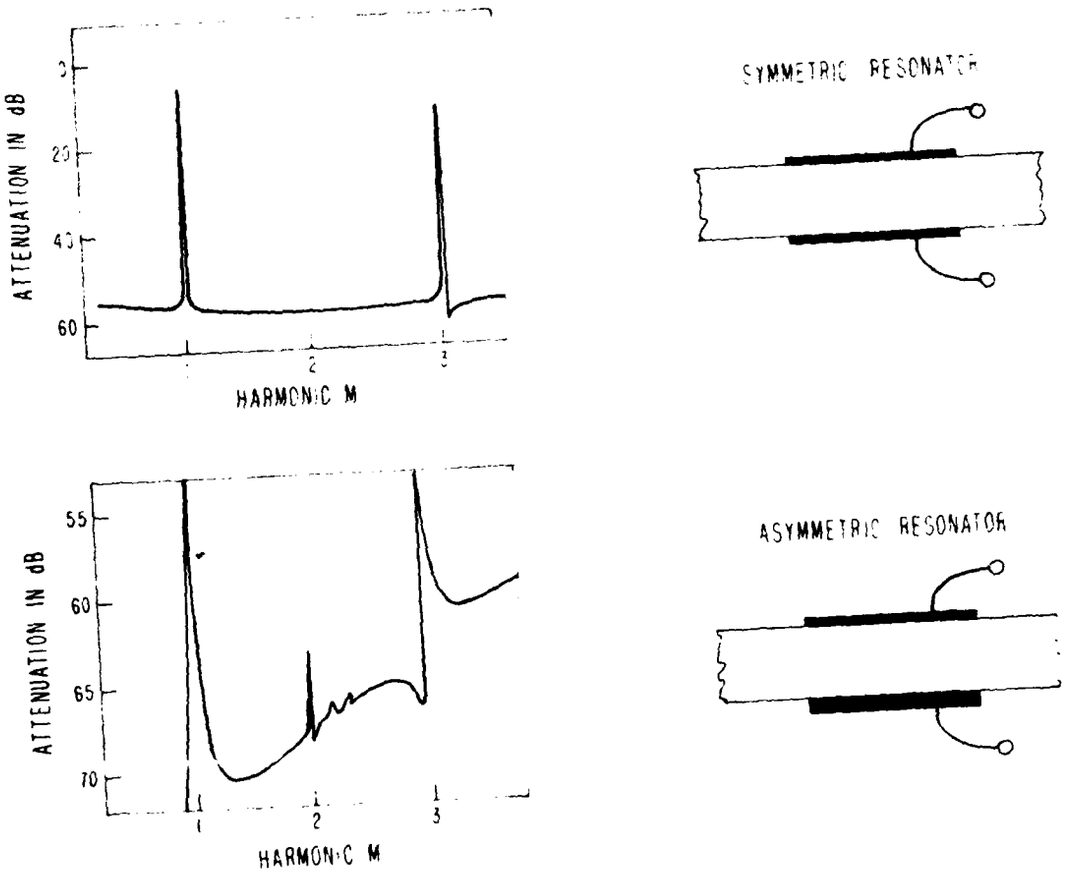

FIGURE 12. Symmetric and Asymmetric Resonators

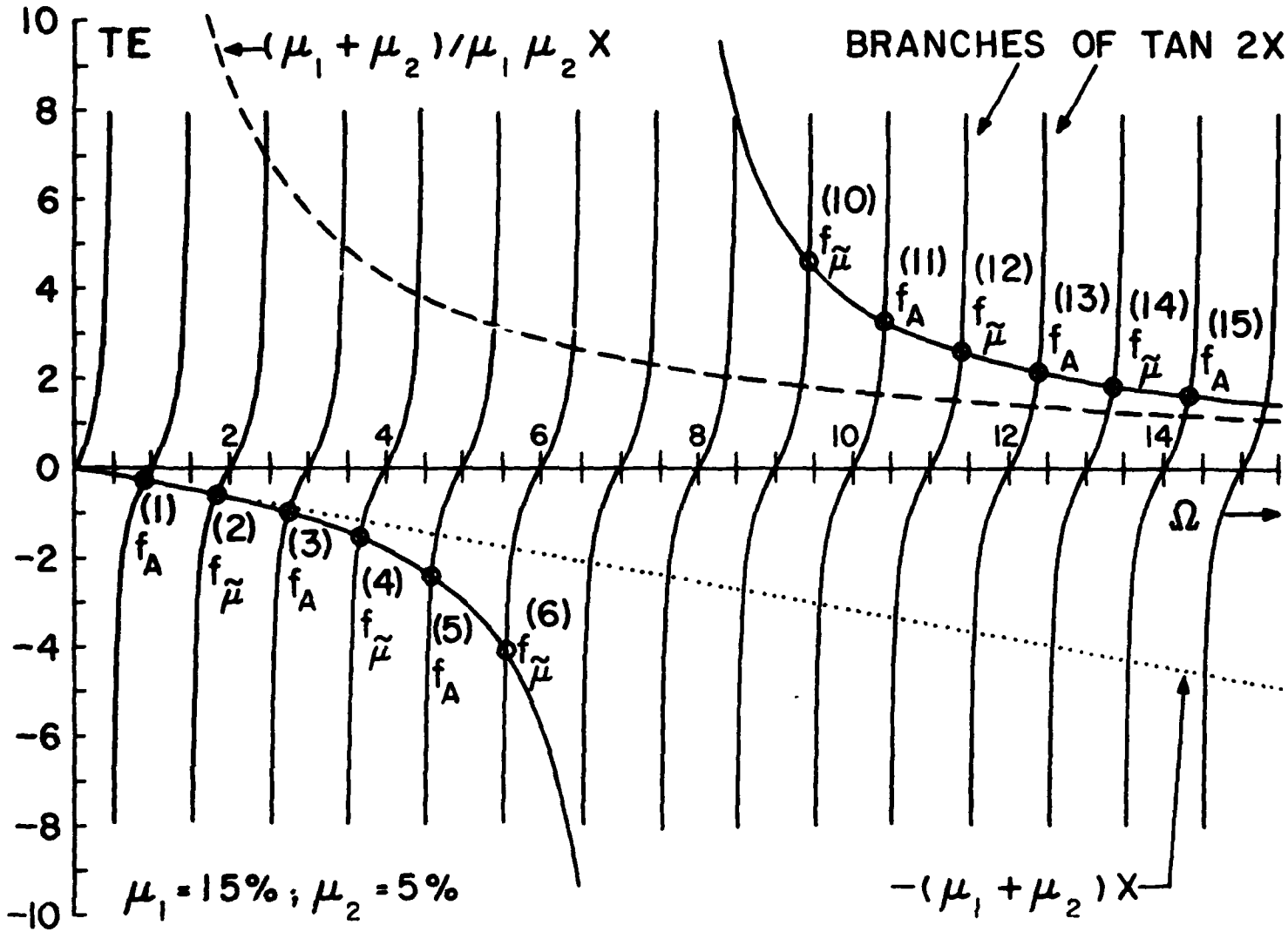

FIGURE 13. Construction for Antiresonant Frequencies with Imbalance

where $\Sigma = (\mu_1 + \mu_2)/2$ and $\Delta = (\mu_1 - \mu_2)/2$. Equation (8) has been written in terms of argument X for the tangent and cotangent functions. The antiresonant frequencies (denoted $f_A(M)$ for M odd, and $f_A(M)$ for M even) are found from the vanishing of the bracketed term in (8) as roots of

$$\tan 2X = \frac{-(\mu_1 + \mu_2)\, X}{(1 - \mu_1 \mu_2 X^2)} . \qquad (9)$$

These are shown in Fig. 13 along with the high and low frequency asymptotes of the right hand side of (9). The roots for the resonant frequencies are found from the zeros of (8).

The even-harmonic resonances produced by the unequal mass-loadings on the crystal plate surfaces ($\mu_1 \neq \mu_2$) are very sharp compared to the odd harmonics as may be seen from Fig. 14, which is drawn for a case with large piezo-coupling and large mass asymmetry in order to widen the resonance regions of both the even and odd harmonics. It is thus possible to use such resonances for stabilizing the frequency of an oscillator - at least in principle. Figure 15 shows a blow-up of the second harmonic of the case of Fig. 14; Fig. 16 shows the fourth harmonic, and Fig. 17 shows the fourteenth harmonic. Compare the width of the resonance in Fig. 17 with that of Fig. 18 showing the fifteenth harmonic. In general, for large M, the normalized frequency of response approaches (M-1).

When the resonator shown in the top of Fig. 12 was overcoated with electrode material on one side only, the mode spectrum shown in the bottom of the figure was produced. The second harmonic becomes present due to the imbalance, and it is sharp; however, it is also very weak. Figure 19 shows a photograph of the spectrograph given in the top of Fig. 12; Fig. 20 is a photograph of the spectrograph for the case of mass imbalance to the same scale as Fig. 20; Fig. 21 shows a magnified view of the photograph of Fig. 20; it corresponds to the lower drawing in Fig. 12.

Another unsymmetrical structure that leads to even harmonics is the composite resonator; (see Reference 5 for additional references). This structure is shown in Fig. 22, with the equivalent network given in Fig. 23. Here the quartz substrate must be represented by a transmission line because of its thickness; as it shrinks in size the situation of Fig. 6 with inductors is approached.

Apart from producing even harmonics, the presence of asymmetry in resonators (due to unequal electrodes, bevelling, contouring, etc.) is very probably a major cause of "activity dips," or "bandbreaks."[6-8] These are illustrated in Fig. 24, which is taken from Reference 8. Both the frequency versus temperature and the conductance versus temperature curves suffer anomalous dips as the interfering mode's influence is manifest at a particular temperature. The second harmonic mode "divided by two" via the nonlinear elastic constants[9] can produce dips at the fundamental.

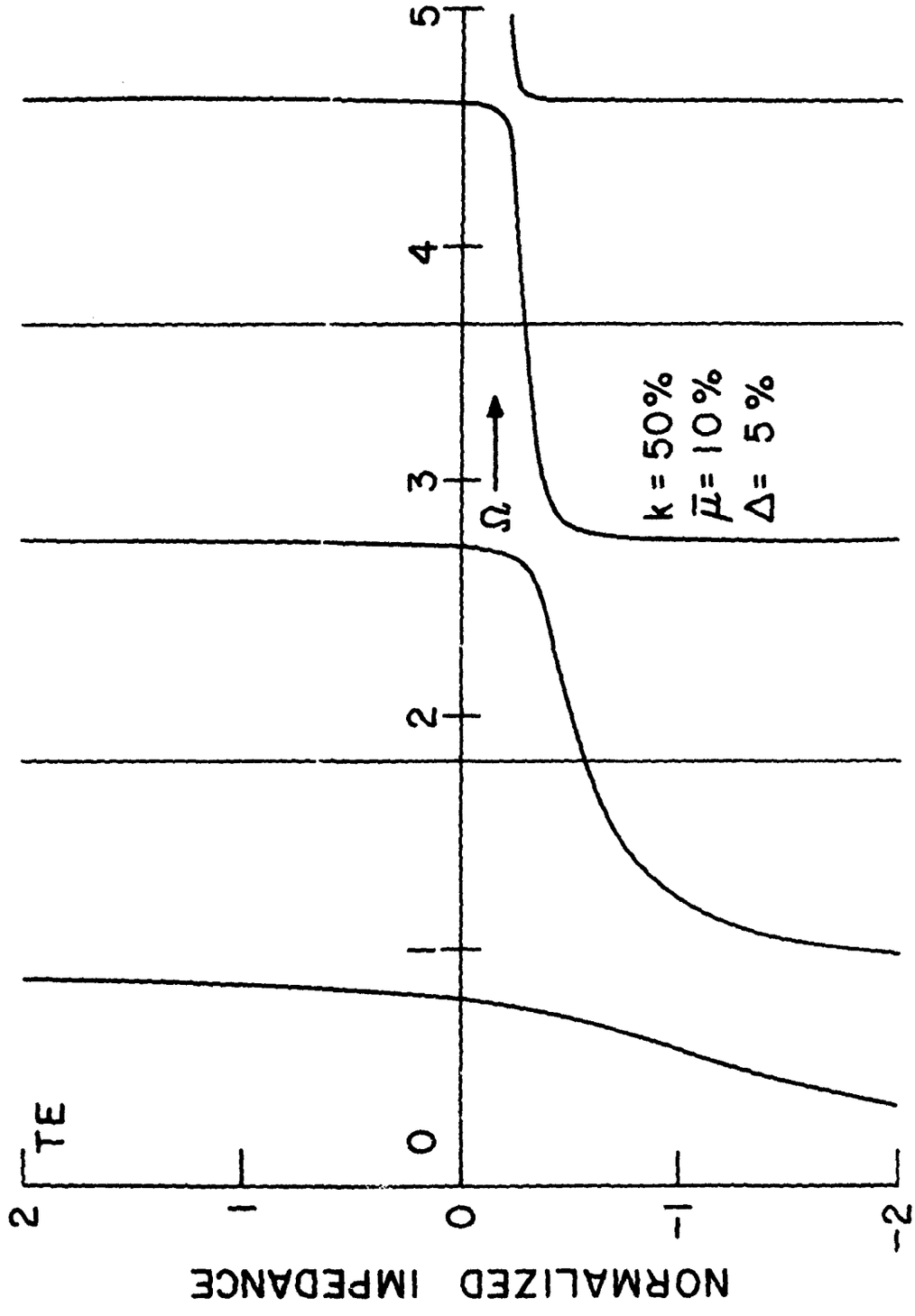

FIGURE 14. Wideband Spectrograph of Imbalanced Resonator

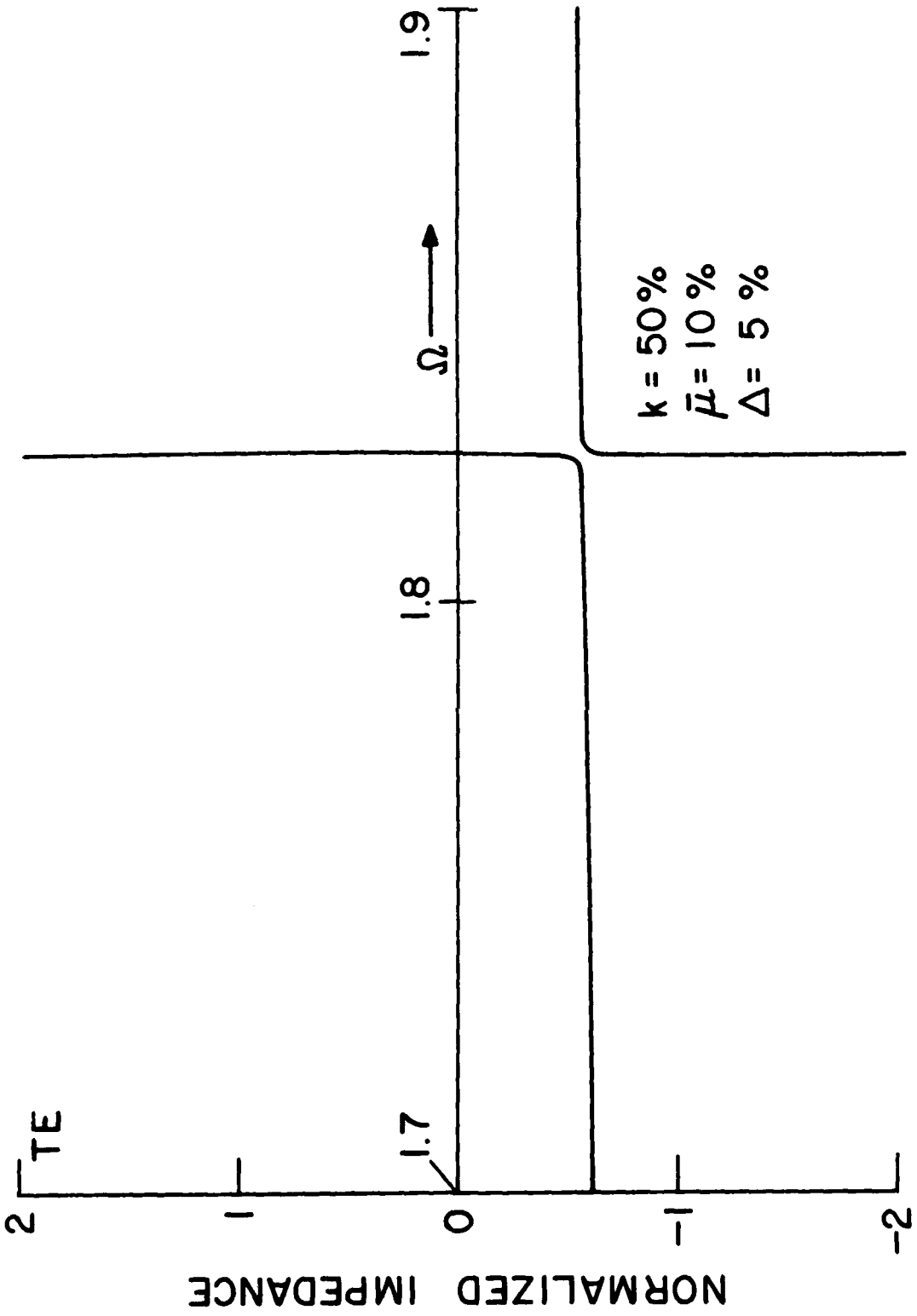

FIGURE 15. Spectrograph Near the Second Harmonic

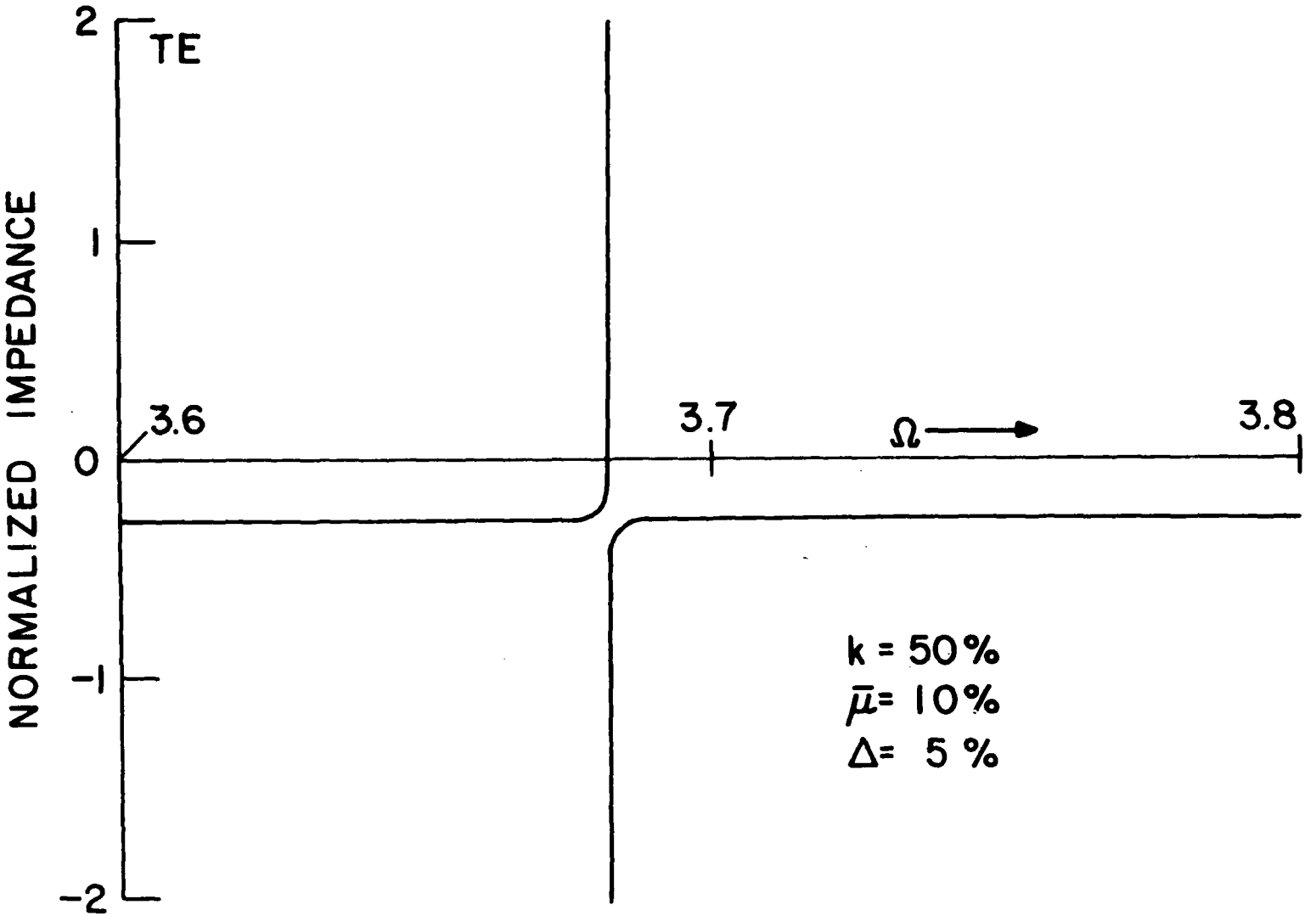

FIGURE 16. Spectrograph Near the Fourth Harmonic

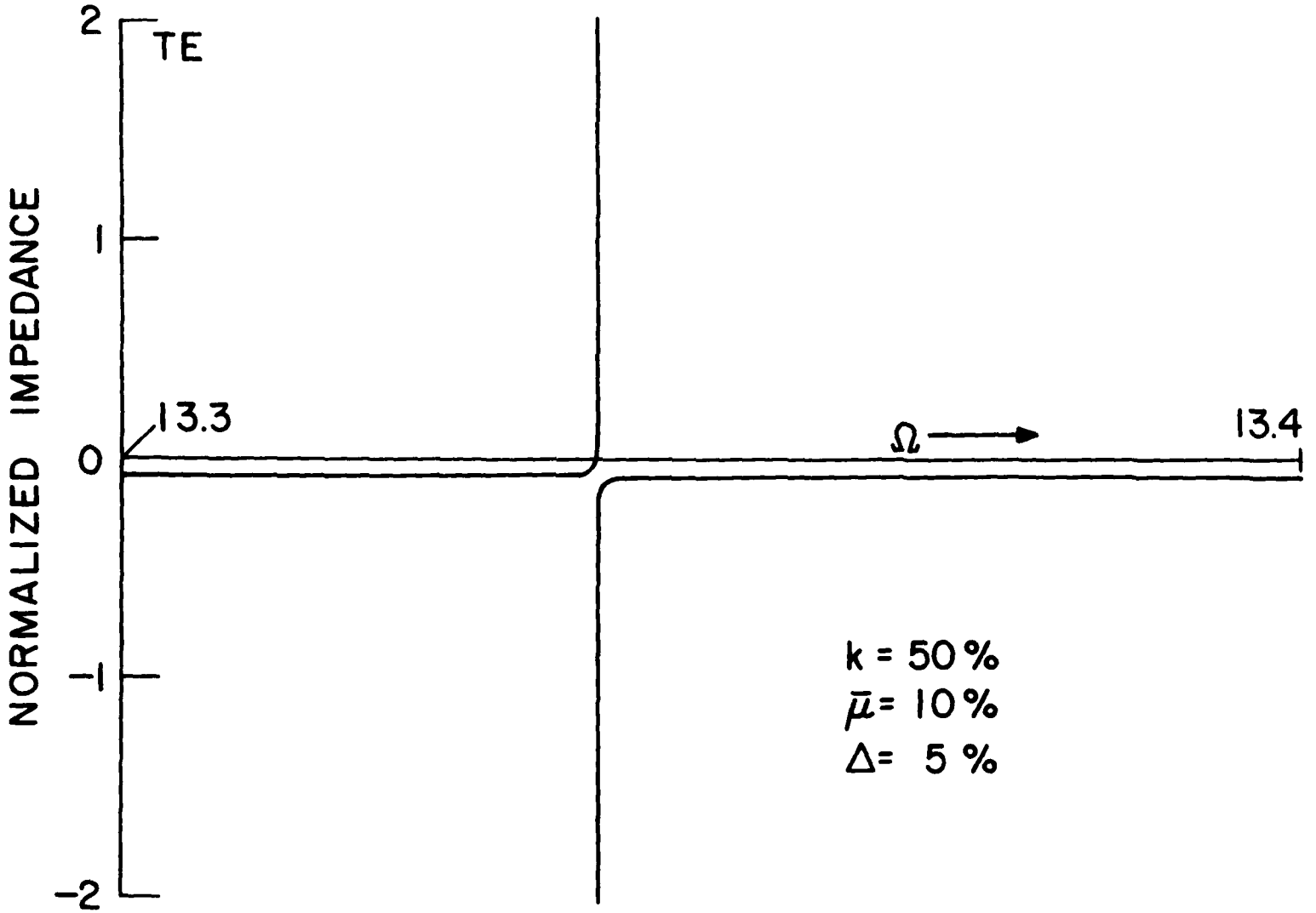

FIGURE 17. Spectrograph Near the Fourteenth Harmonic

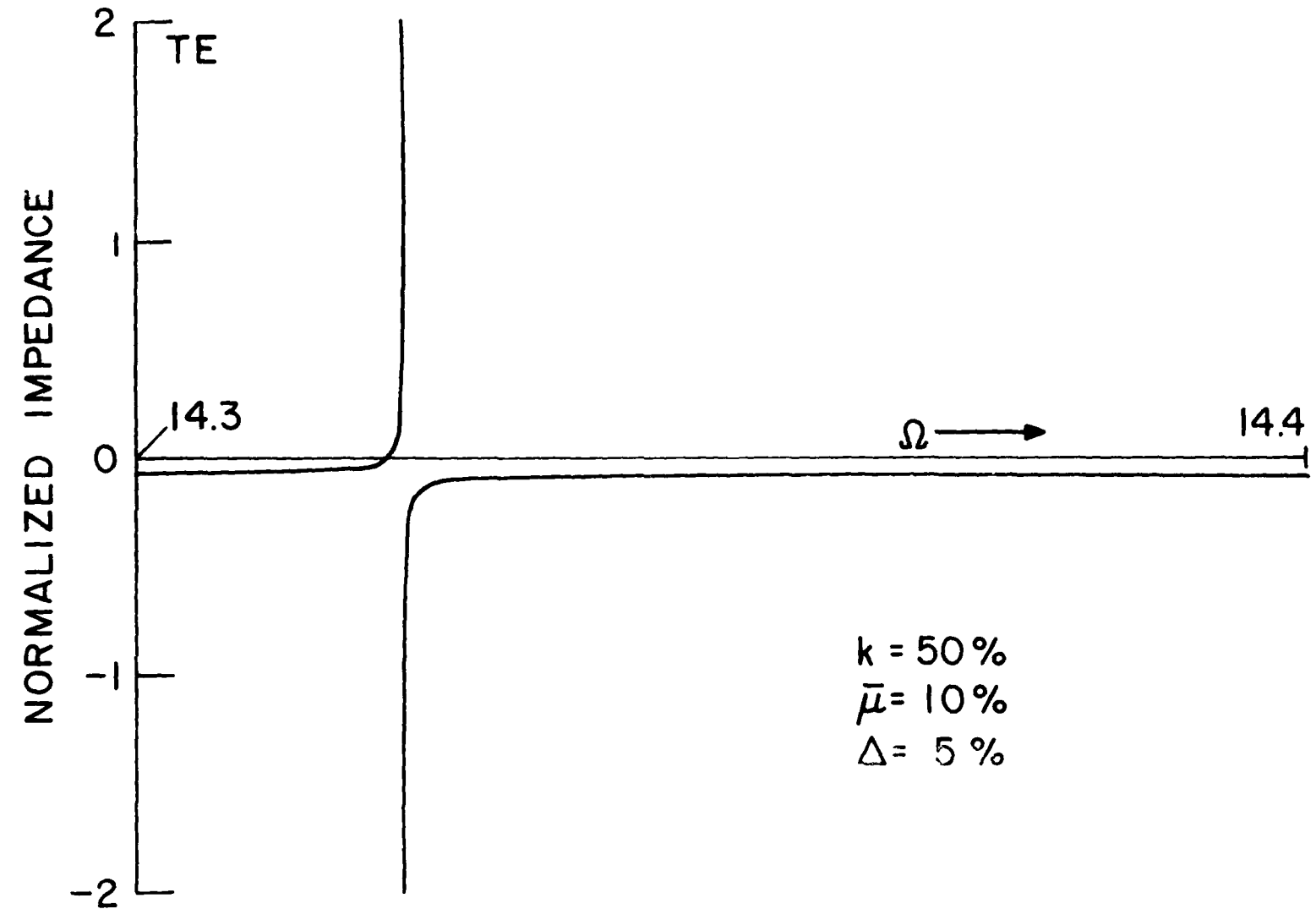

FIGURE 18. Spectrograph Near the Fifteenth Harmonic

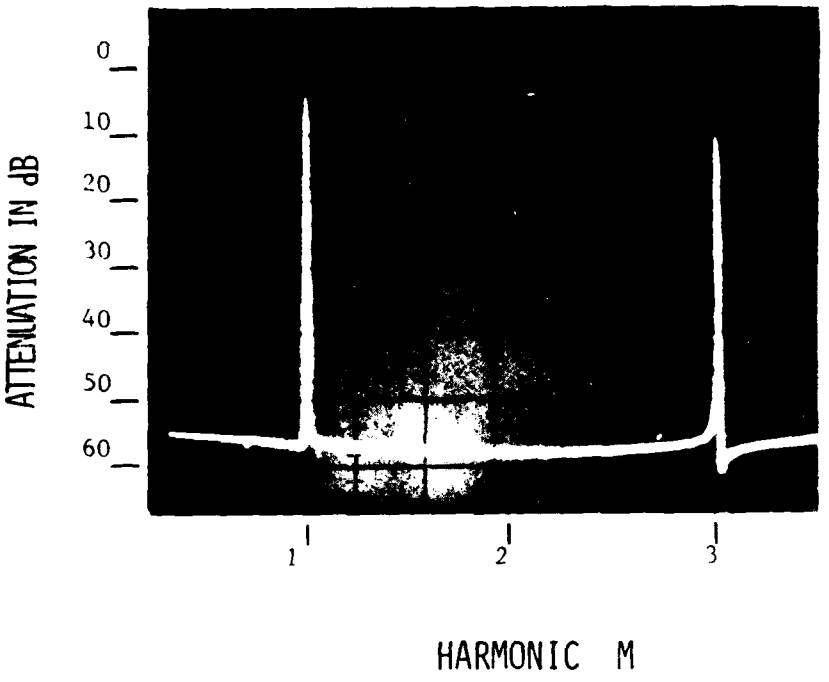

FIGURE 19. Photograph of Spectrum of Balanced Resonator

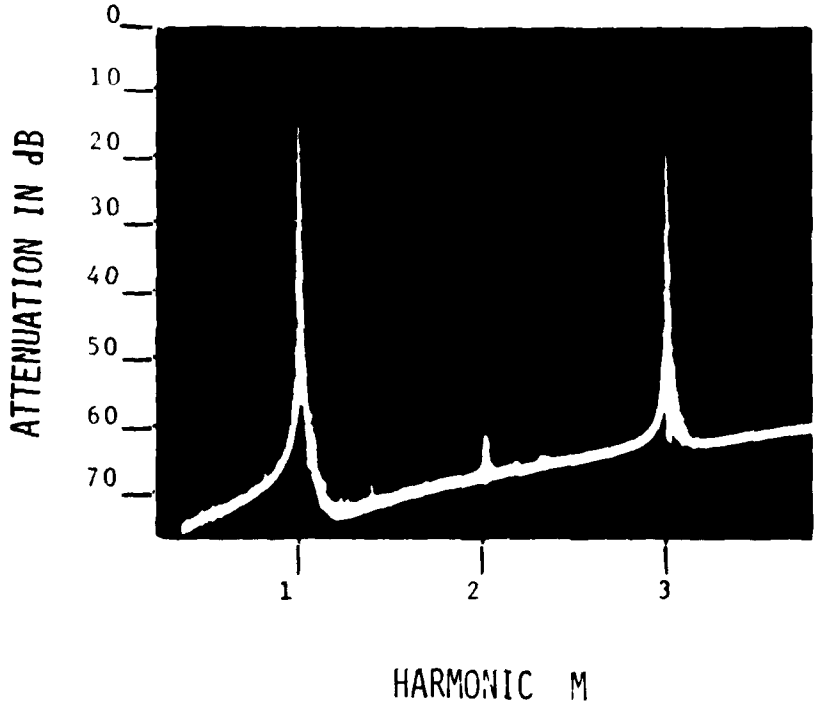

FIGURE 20. Photograph of Spectrum of Imbalanced Resonator

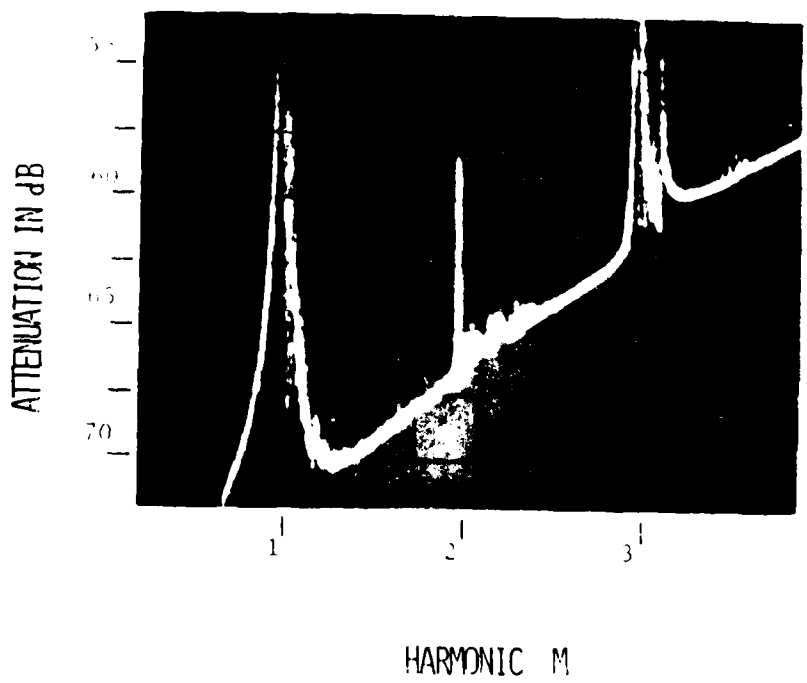

FIGURE 21. Magnification of Spectrum of Figure 20

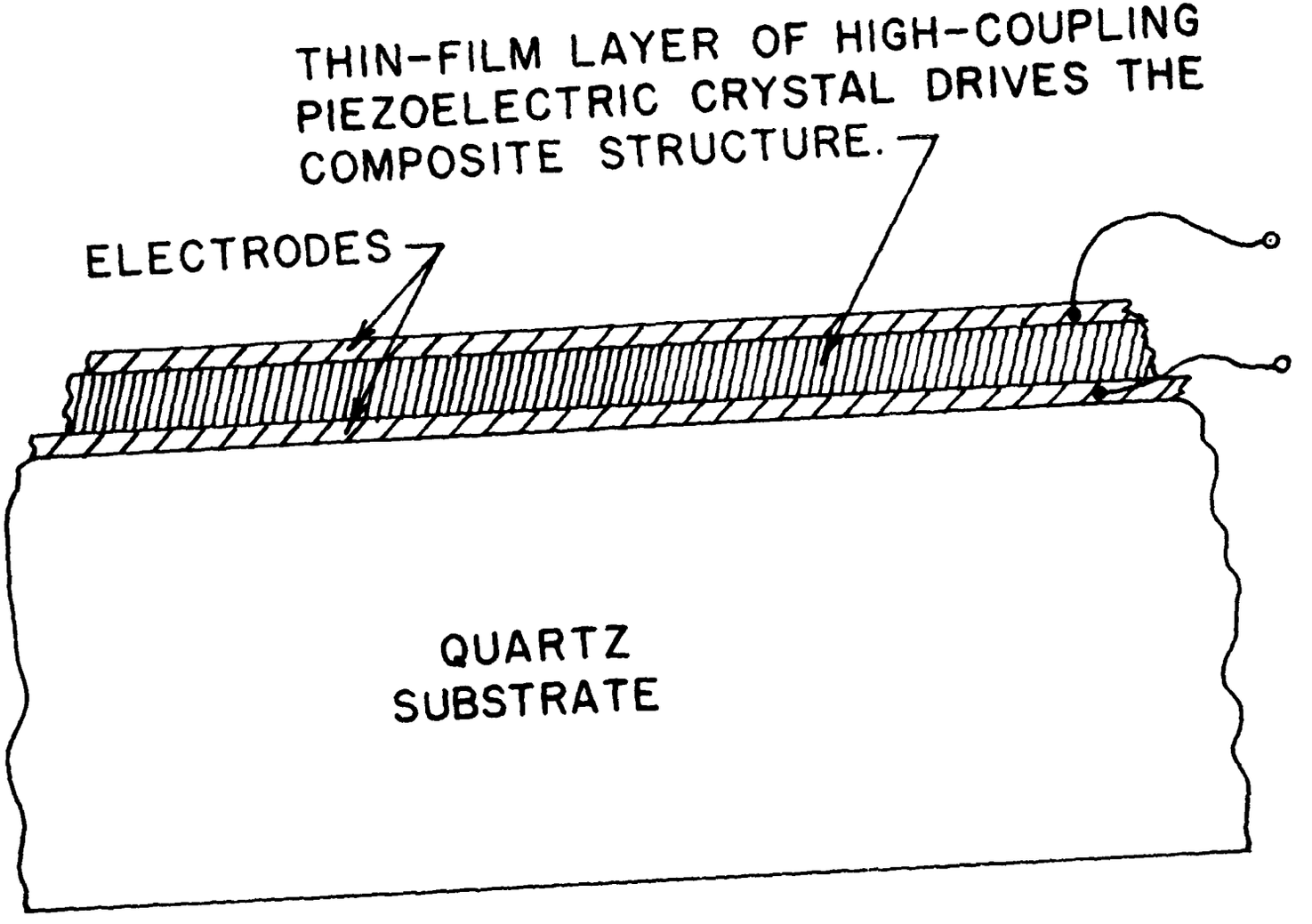

FIGURE 22. COMPOSITE RESONATOR STRUCTURE

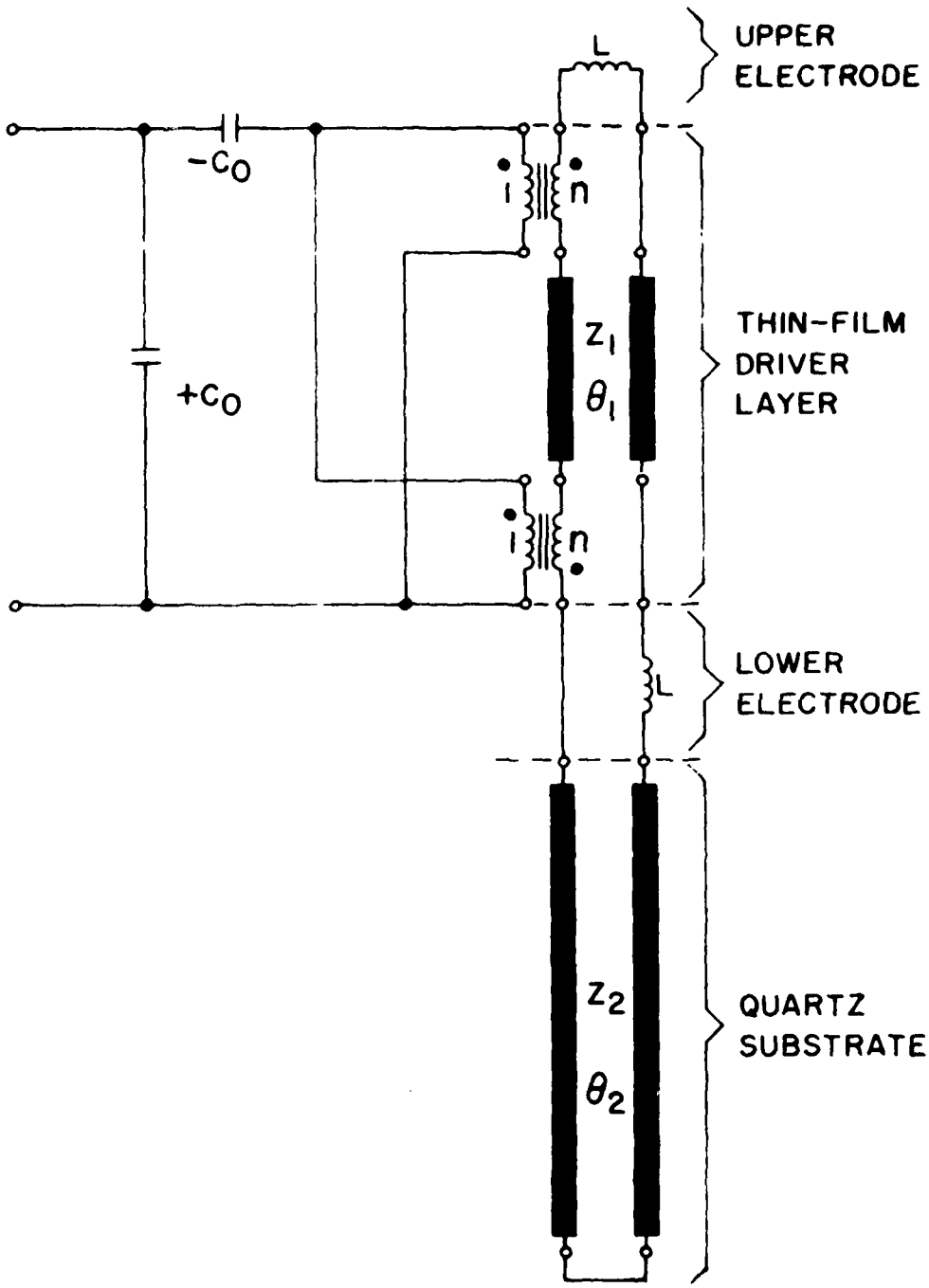

FIGURE 23. EQUIVALENT NETWORK OF COMPOSITE RESONATOR

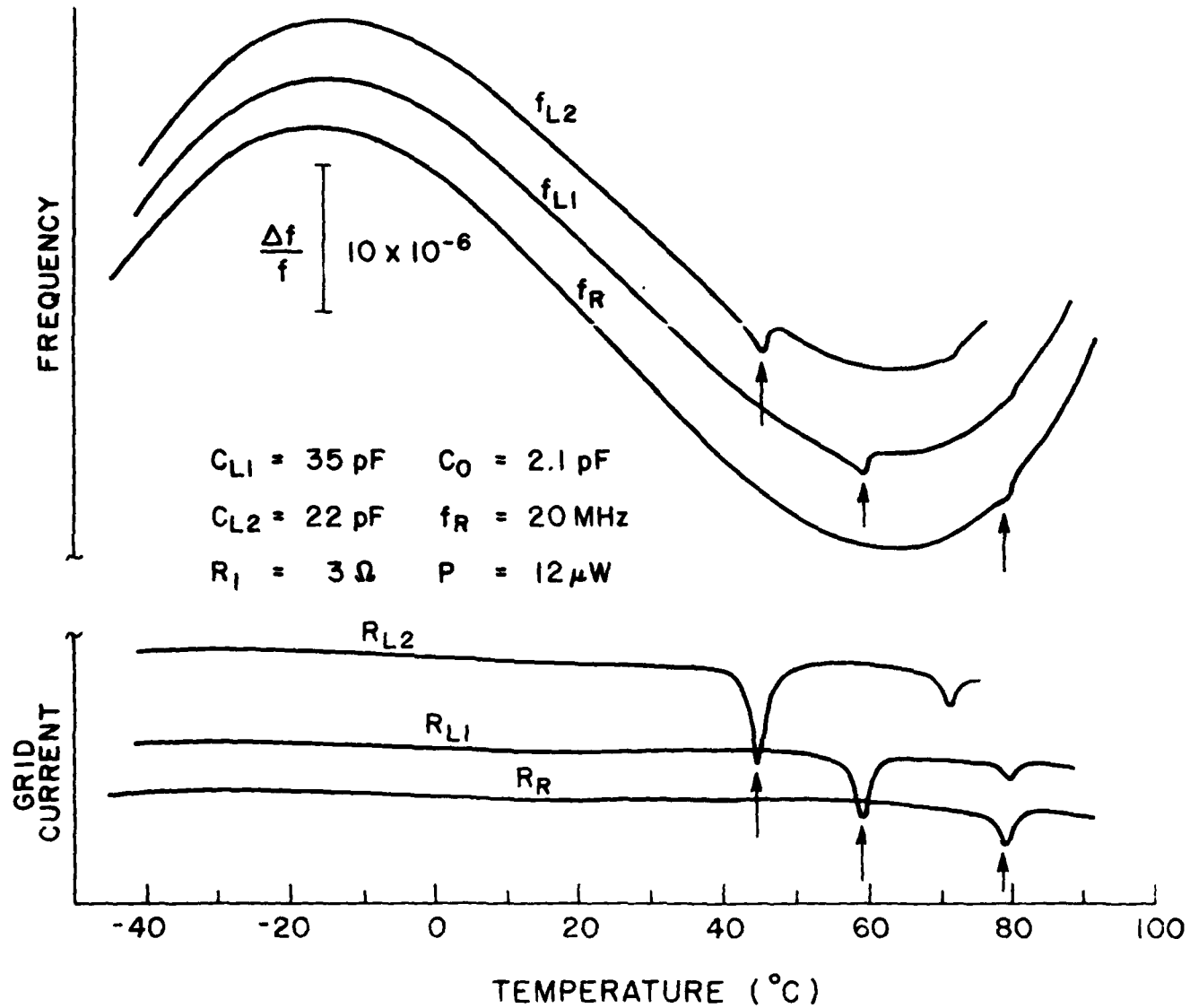

FIGURE 24. Frequency-Temperature Plots Showing Activity Dips

ELECTRODE INFLUENCES

It is well-known that the frequency-temperature (f-T) curve of an AT plate resonator measured sufficiently slowly assumes a cubic shape, as depicted in Fig. 25. Small changes in orientation angle θ, for rotation about the crystallographic X_1 axis, produce slope changes at the inflection point of $-5.08 \times 10^{-6}/K, ^\circ\theta$. A variety of other influences lead to nonnegligible slope variations as well. Figure 25 shows the effect of placing a load capacitor in series with the vibrator to produce frequency f_L, as is often done for frequency trimming. The slope shift reduces the peak-to-peak frequency deviation and must be taken into account in design of temperature compensated crystal oscillators (TCXOs); it comes about because of the temperature coefficient of the piezoelectric coupling factor.[10] A similar effect occurs when a resonator is operated at different harmonics, and for the same reason.

The mass of, and intrinsic stress in electrode coatings also affects the f-T curve. Some time ago the effect of equal electrode coatings was demonstrated in regard to frequency shift and rotation of the static frequency-temperature curve of a resonator.[11-13] The calculations dealt only with the influence of inertial mass; no elastic properties were assumed for the electrodes, nor were they presumed to apply any stresses to the crystal. This was done so that the inertial influence of the electrode could be subtracted from elastic and stress effects. Results from the one dimensional theory for the change in apparent orientation angle are given in Fig. 26 and Fig. 27 as function of harmonic number M and mass loading μ.

A comparison of apparent orientation angle shifts as function of mass loading and harmonic number is given in Fig. 28 for AT plates of 5MHz fundamental frequency, and plate/electrode diameters of 14 and 6 mm, respectively, coated with evaporated aluminum, sputtered chromium, and sputtered indium. The electrodes are of equal thicknesses. It is seen that Al and In have slopes that agree with inertial mass theory, but are displaced; the curves for Cr are consistent among themselves, but differ in sign from the theory. The results in Fig. 28 indicate the importance of electrode material, deposition method, and conditions of deposition on the behavior of the finished resonator. Figure 29 gives the experimental data for aluminum evaporated electrodes as function of μ and M. Figure 30 shows the decrease in inflection temperature with increasing mass of evaporated aluminum, for resonators with the parameters described above.

It should be borne in mind that stresses in the electrodes can also produce activity dips, even when the electrodes are of equal mass. Consequently, the practice of furnishing AT quartz plates with a thin layer of Ni or Cr to insure adhesion of gold, e.g., ought to be re-examined in view of the stress levels produced by these metals, both intrinsically, and as a function of temperature.

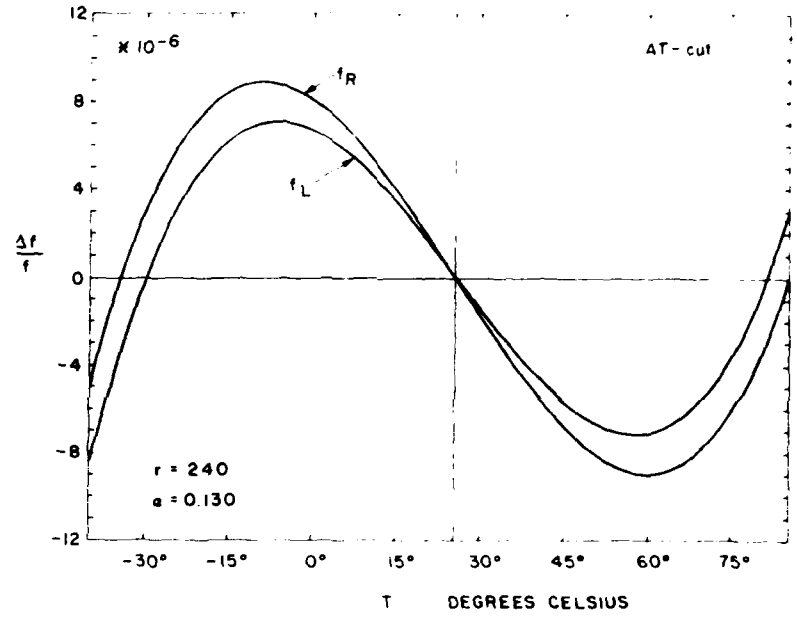

FIGURE 25. Frequency-Temperature Plots of AT-Cut Resonators

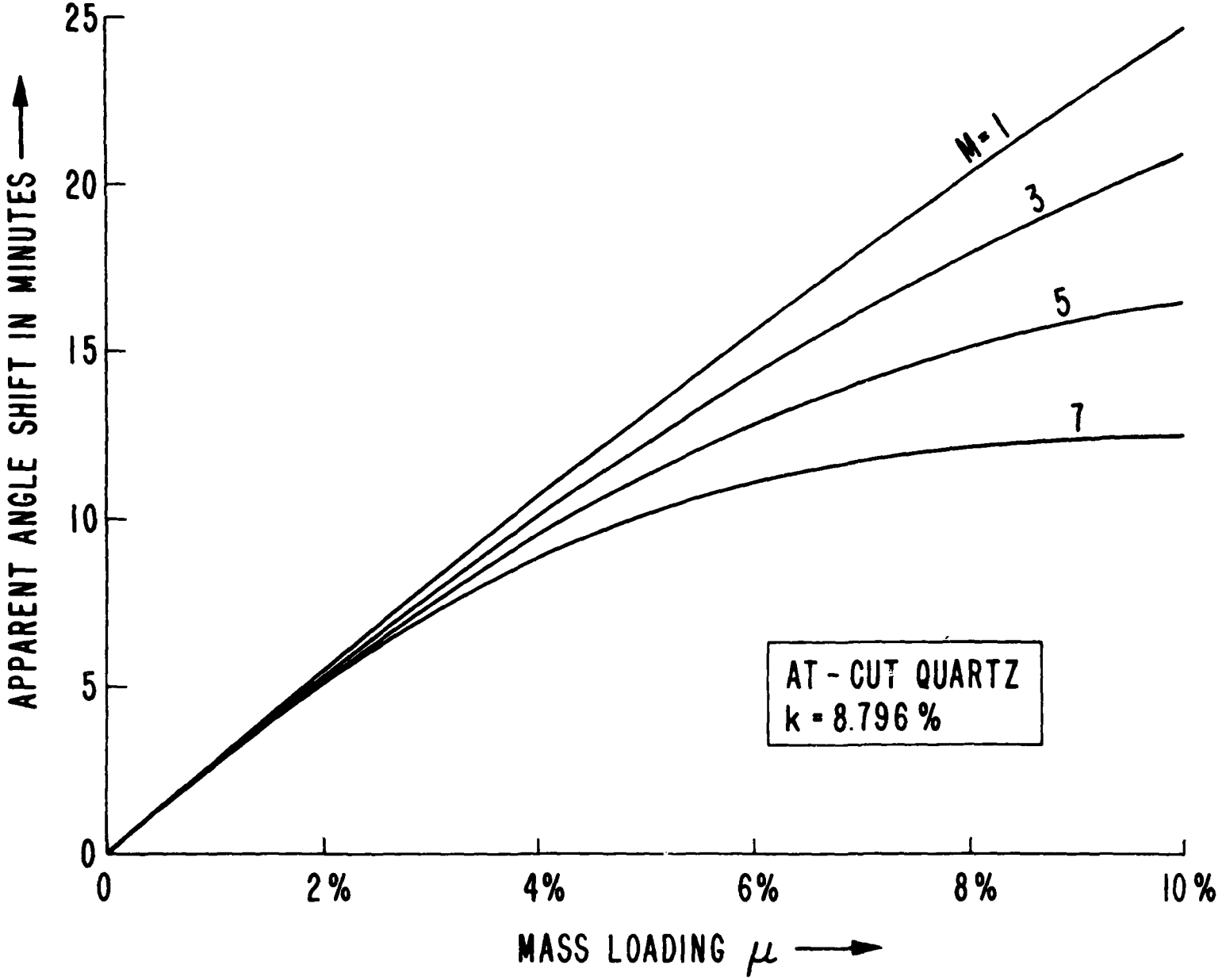

FIGURE 26. Apparent Angle Shift versus Mass Loading

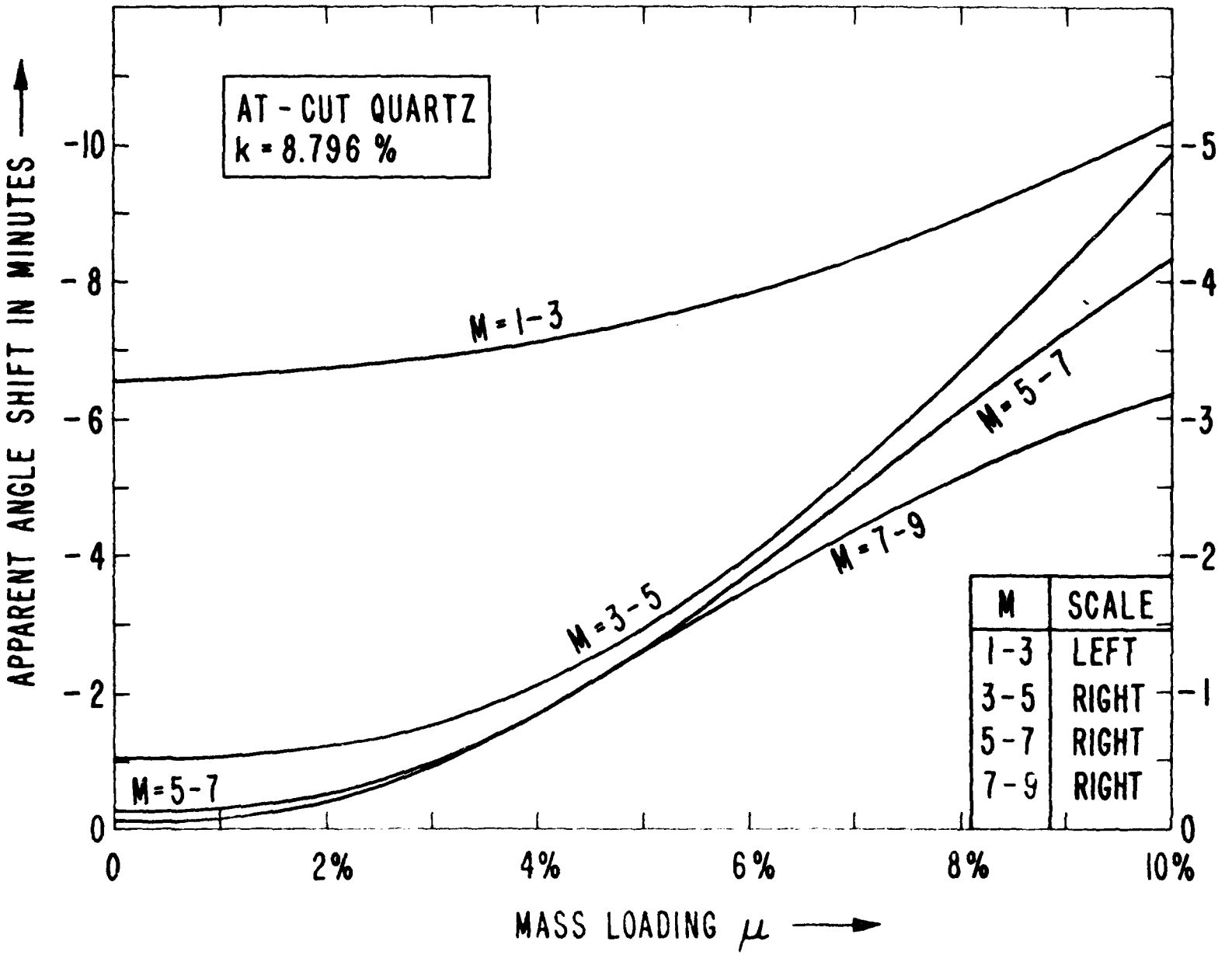

FIGURE 27. Angle Shift versus Loading for Harmonic Transitions

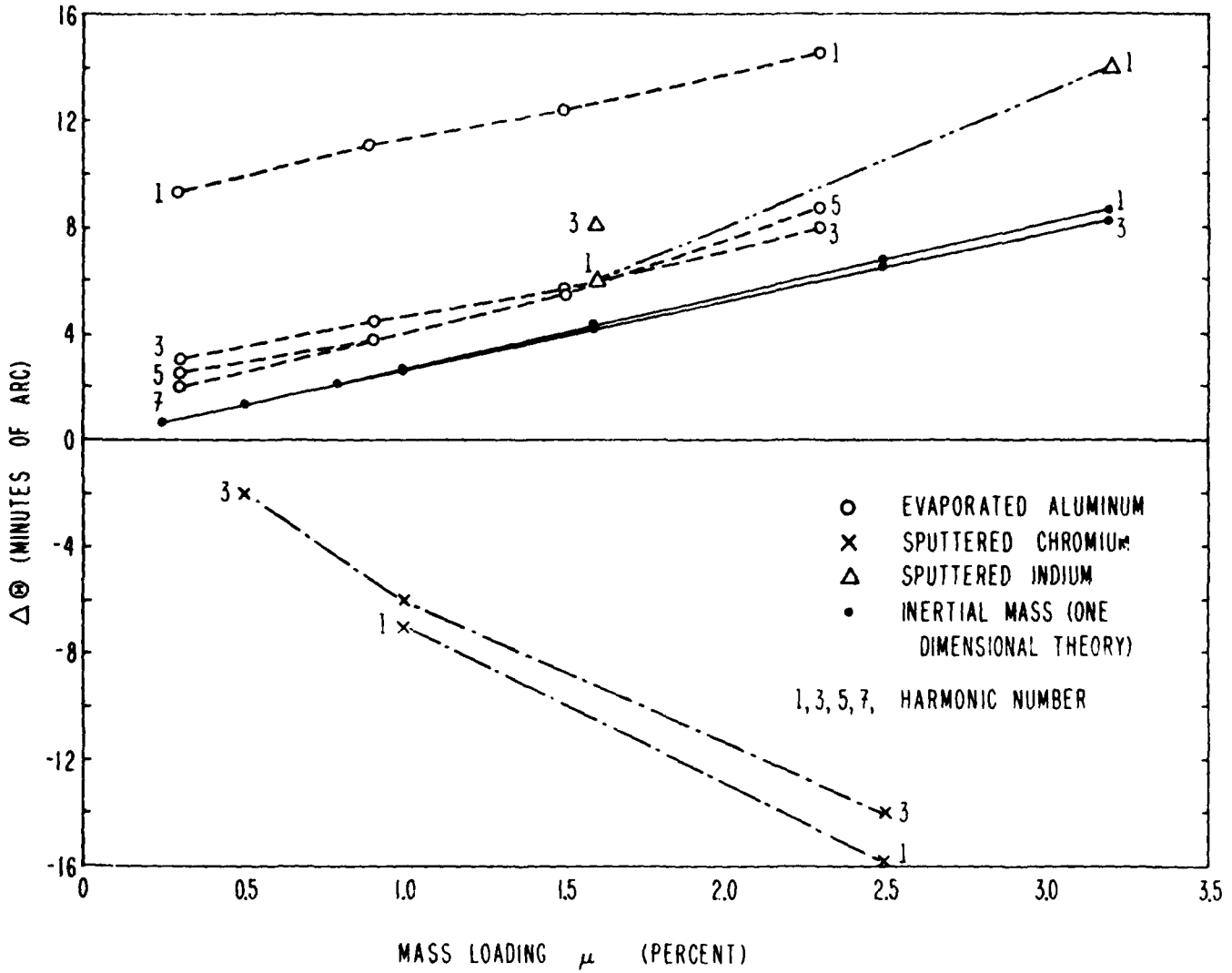

FIGURE 28. Experimental Angle Shifts versus Mass Loading

HARMONIC NUMBER

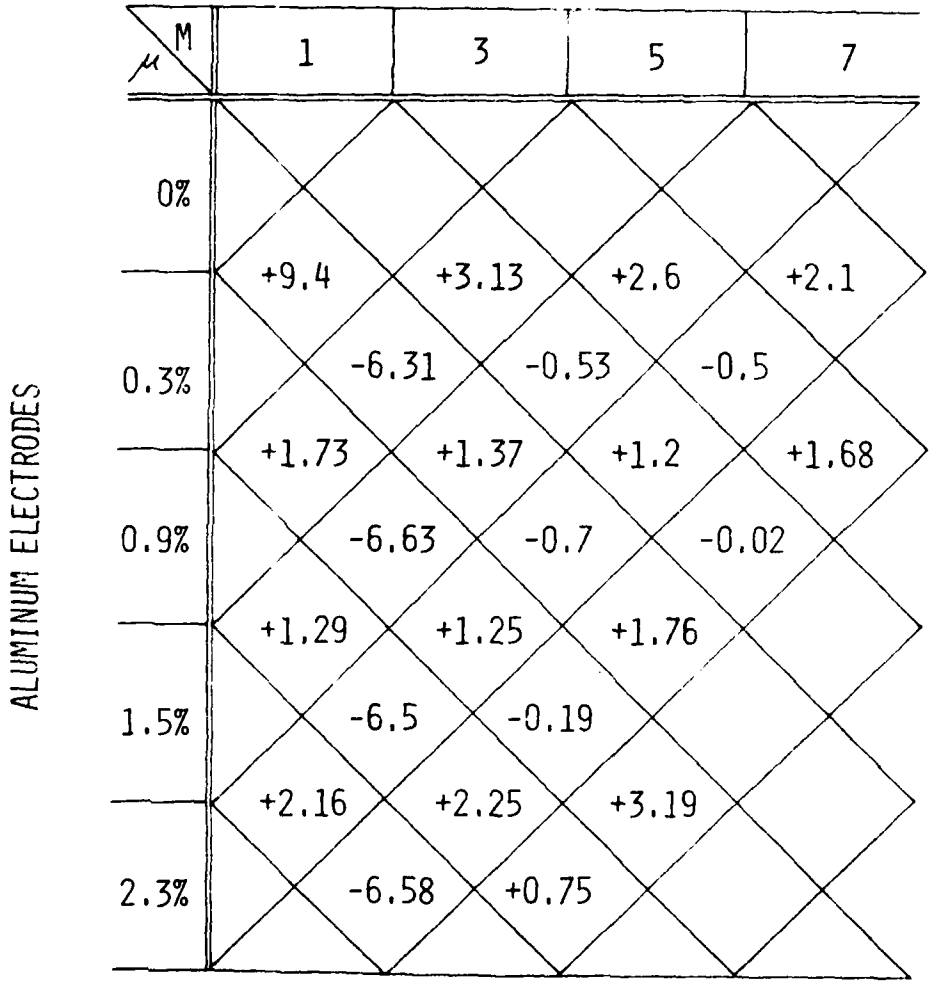

FIGURE 29. APPARENT ANGLE SHIFT IN MINUTES OF ARC

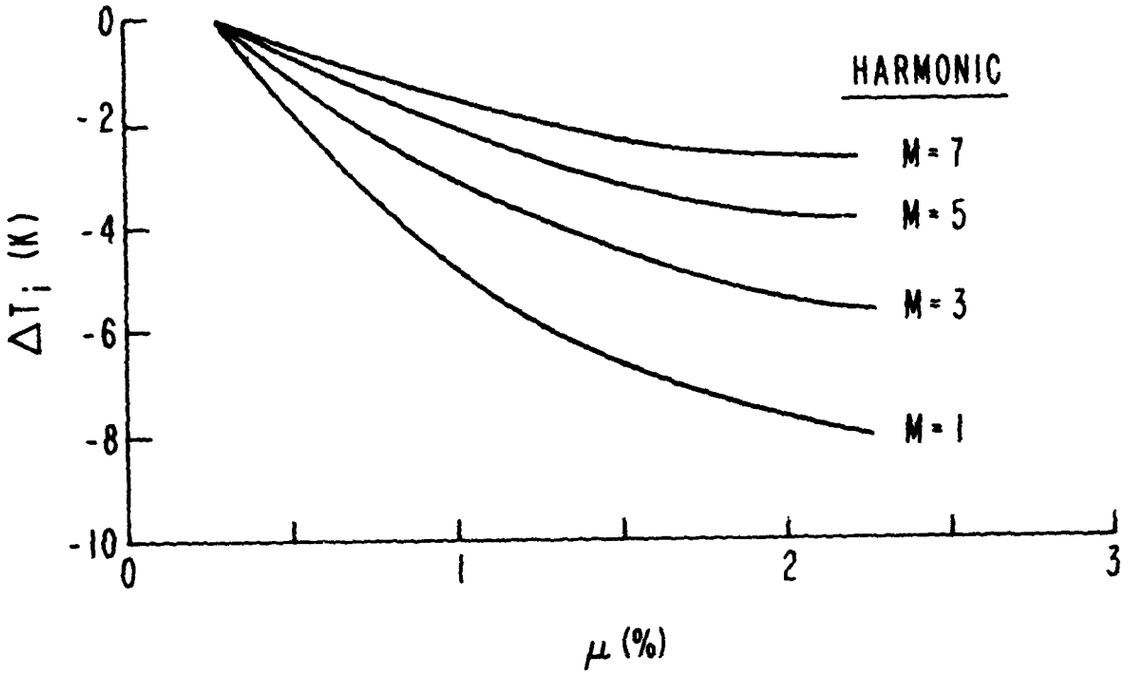

FIGURE 30. INFLECTION TEMPERATURE CHANGE WITH INCREASING MASS

ANGULAR MISORIENTATION

Subtle influences on the static frequency-temperature curve were briefly discussed in the previous section in terms of apparent orientation angle changes in θ, for AT resonators. The most general class of thickness mode plate resonators is the family of doubly rotated cuts.[14] These are compared in Fig. 31 with singly rotated cuts, of which the AT cut is the most often used. Also shown in the figure are the loci of zero temperature coefficient, and the angular coordinates of popular quartz cuts. The line $\phi = 0$ is a line of symmetry, so that singly rotated cuts are only quadratically sensitive to misorientations in ϕ. For the AT cut, misorientations $\pm\Delta\phi$ may be compensated for by changes $\Delta\theta$, obtained from

$$\Delta\theta = -1.77 \times 10^{-3} (\Delta\phi)^2,$$

with $\Delta\phi$ in minutes of arc, and $\Delta\theta$ in seconds of arc; this relationship is portrayed in Fig. 32.

X-RAY ANGLE CHANGES[15]

The angles locating the X-ray planes in a crystal are functions of temperature and external stress. For example, the plane at 38° 13' used for orienting AT cuts is only found at this angle at a certain temperature. For high precision applications the angle shift with temperature is not negligible. We give an approximate calculation to establish the order of magnitude of the angle change.

Consider a rotated-Y-cut plate of crystal in the rhombic, tetragonal, trigonal, hexagonal, or cubic systems. (These have no off-diagonal thermoelastic coefficients.) At temperature T the plate angle will be determined from

$$\tan \theta = (X_2/X_3). \tag{10}$$

With a change in temperature to $T+\Delta T$, the axes become, in the linear approximation

$$\begin{aligned} X_2' &= X_2 (1 + \alpha_{22} \Delta T) \\ X_3' &= X_3 (1 + \alpha_{33} \Delta T) \end{aligned} \tag{11}$$

We are thus led to a relation between $\Delta\theta$ and ΔT:

$$\tan \Delta\theta = \{(A-1) \tan \theta / (1 + A \tan^2 \theta)\} \tag{12}$$

where

$$A = (1 + \alpha_{22} \Delta T)/(1 + \alpha_{33} \Delta T). \tag{13}$$

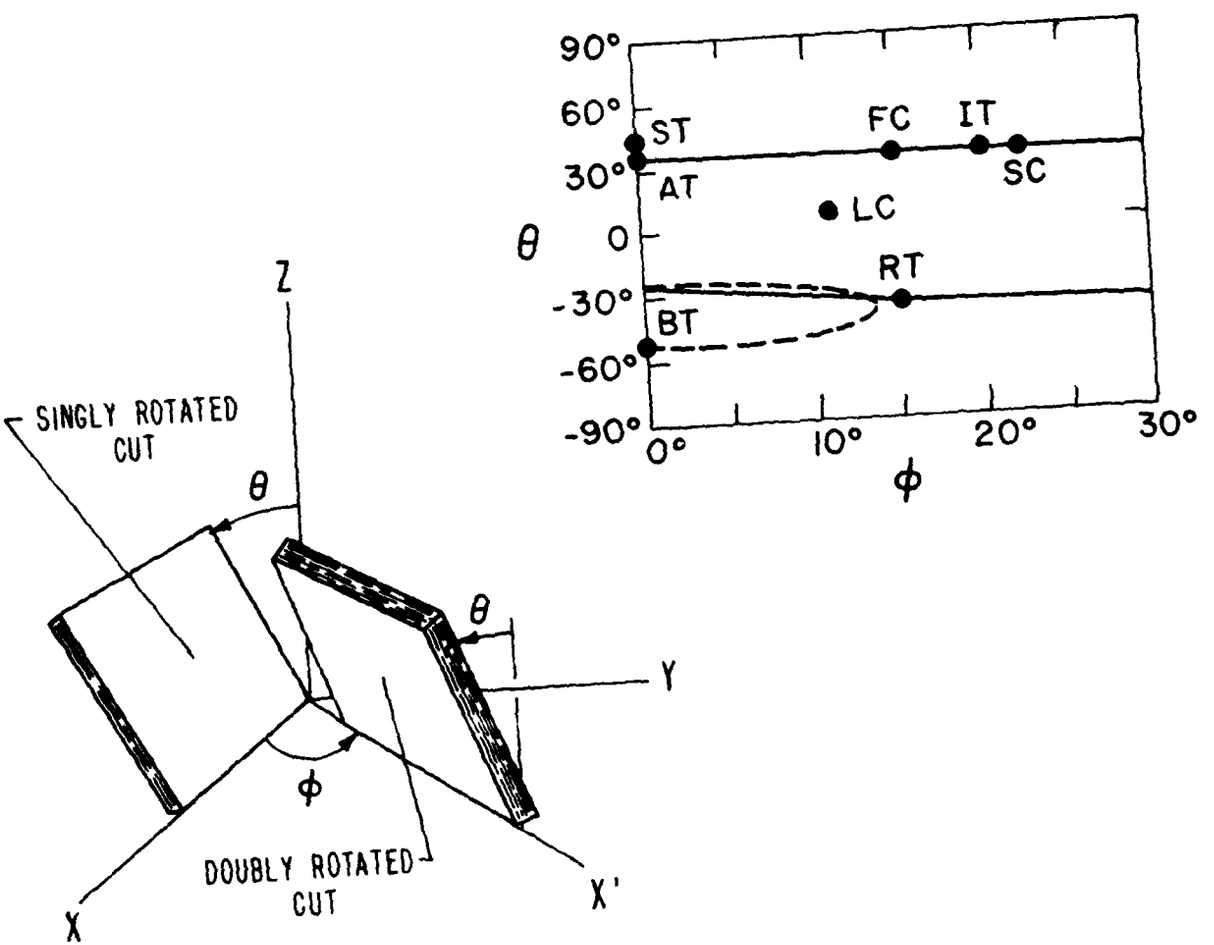

FIGURE 31. Doubly Rotated Cuts and Zero Temperature Coefficient Loci

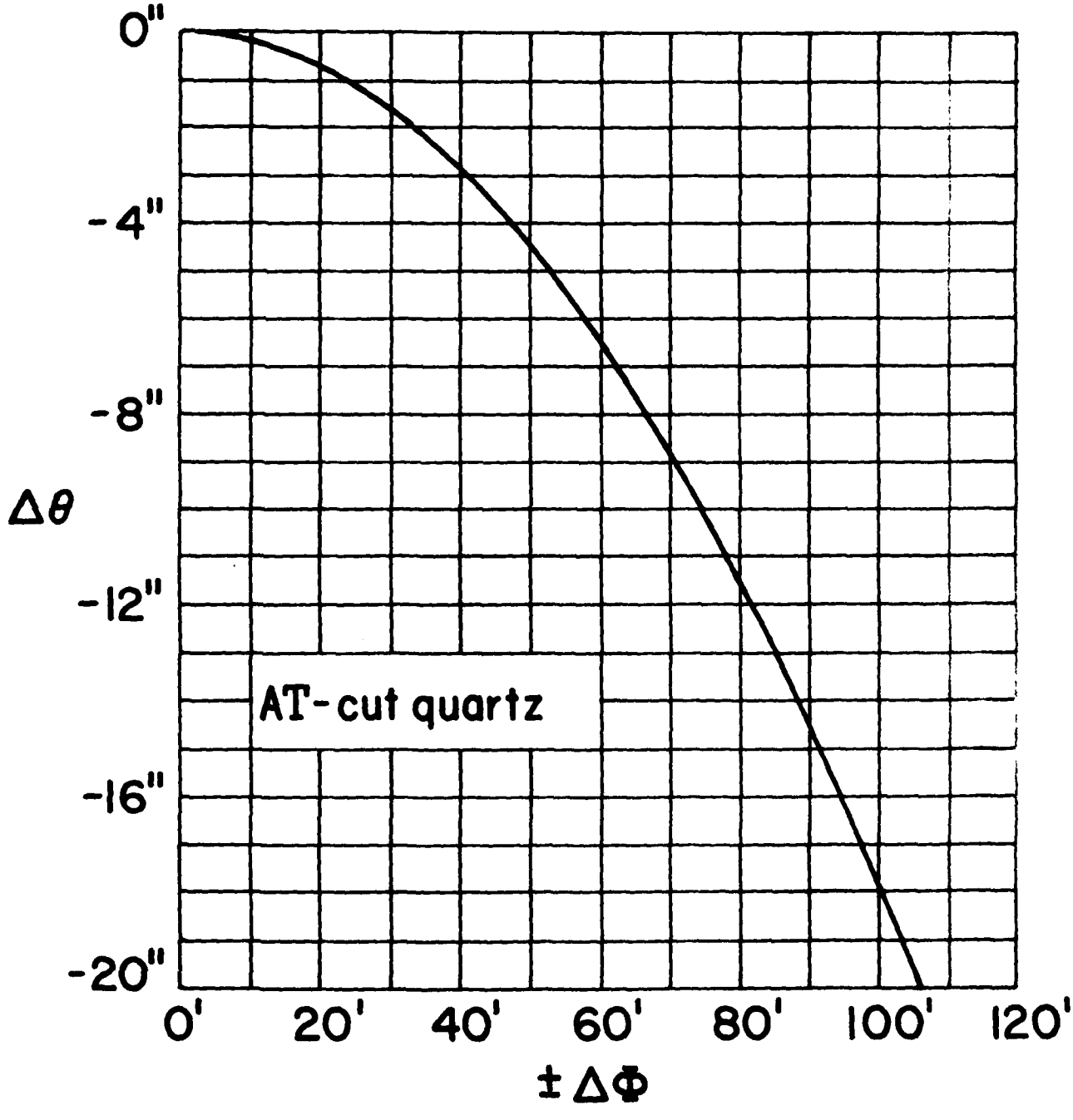

FIGURE 32. Delta Theta versus Delta Phi for AT Cuts

As a consequence of (12) and (13) we have

$$\Delta\theta \simeq \tfrac{1}{2}\,(\alpha_{11} - \alpha_{33}) \cdot \Delta T \cdot \sin 2\theta. \qquad (14)$$

Figure 33 gives the X-ray angle change with temperature; beyond about 10 kelvins the linear approximation is not accurate except as to order of magnitude. For the tetragonal, trigonal and hexagonal systems, since $\alpha_{22} = \alpha_{11}$, the result is independent of angle ϕ. In particular, for the upper zero temperature locus for thickness mode plates θ is approximately constant and the result holds therefore for the AT, FC, IT, and SC cuts (cf. Fig. 31). Relation (14) shows that $\Delta\theta$ depends on the difference between α_{11} and α_{33} for rotated-Y-cuts (or doubly rotated cuts when $\alpha_{22} = \alpha_{11}$). For the cubic system this difference is zero, so $\Delta\theta$ is always zero in this system. For quartz, the effective value of α in the thickness direction of rotated-Y-cut plates is shown in Fig. 34; it is given by

$$\alpha = \alpha_{11} \cos^2 \theta + \alpha_{33} \sin^2 \theta; \qquad (15)$$

for the Y cut, $\alpha = \alpha_{22} = \alpha_{11} = 13.72 \times 10^{-6}/K$, while for the Z cut ($\theta = \pm 90^{\circ}$), $\alpha = \alpha_{33} = 7.48 \times 10^{-6}/K$.

TWINNING

The types of twinning that may occur in quartz are shown in Fig. 35 along with the changes in axes and handedness.[16,17] We briefly explore the effects of twinning on the piezoelectric constants of crystals in Class 18, which includes quartz. For the three types of twinning considered, the operations involved are

(a) Dauphiné: $X_1 \to -X_1$; $X_2 \to -X_2$; $X \to +X_3$.

$e_{11} \to -e_{11}$; $e_{14} \to +e_{14}$.

(b) Brazil: $X_1 \to -X_1$; $X_2 \to +X_2$; $X \to +X_3$.

$e_{11} \to -e_{11}$; $e_{14} \to -e_{14}$.

(c) Combined: $X_1 \to +X_1$; $X_2 \to -X_2$; $X \to +X_3$.

$e_{11} \to +e_{11}$; $e_{14} \to -e_{14}$.

Consider e'_{26}, the piezoelectric constant driving the pure shear mode in rotated-Y-cuts of quartz:

Untwinned: $e'_{26} = (e_{11} \cos\theta + e_{14} \sin\theta) \cdot (-\cos\theta)$.

(a) Dauphine: $e'_{26} = (-e_{11} \cos\theta + e_{14} \sin\theta) \cdot (-\cos\theta)$.

(b) Brazil: $e'_{26} = (e_{11} \cos\theta + e_{14} \sin\theta) \cdot (+\cos\theta)$.

(c) Combined: $e'_{26} = (e_{11} \cos\theta - e_{14} \sin\theta) \cdot (-\cos\theta)$.

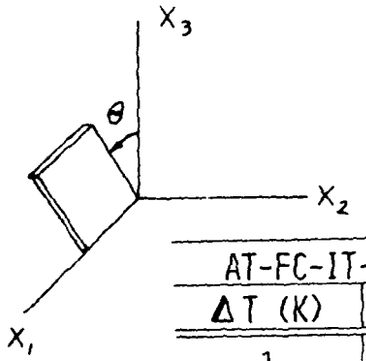

ANGLE θ AT TEMPERATURE T

ANGLE $\theta+\Delta\theta$ AT TEMPERATURE $T+\Delta T$

$$\Delta\theta \simeq \tfrac{1}{2}(\alpha_{11}-\alpha_{33})*\Delta T*\sin 2\theta$$

AT-FC-IT-SC CUTS		BT CUT	
ΔT (K)	$\Delta\theta$ (SEC.)	ΔT (K)	$\Delta\theta$ (SEC.)
1	0.6	1	-0.6
3	1.8	3	-1.9
10	6.1	10	-6.4
30	18.2	30	-19.1
100	60.6	100	-63.6

FIGURE 33. Change of Orientation with Angle

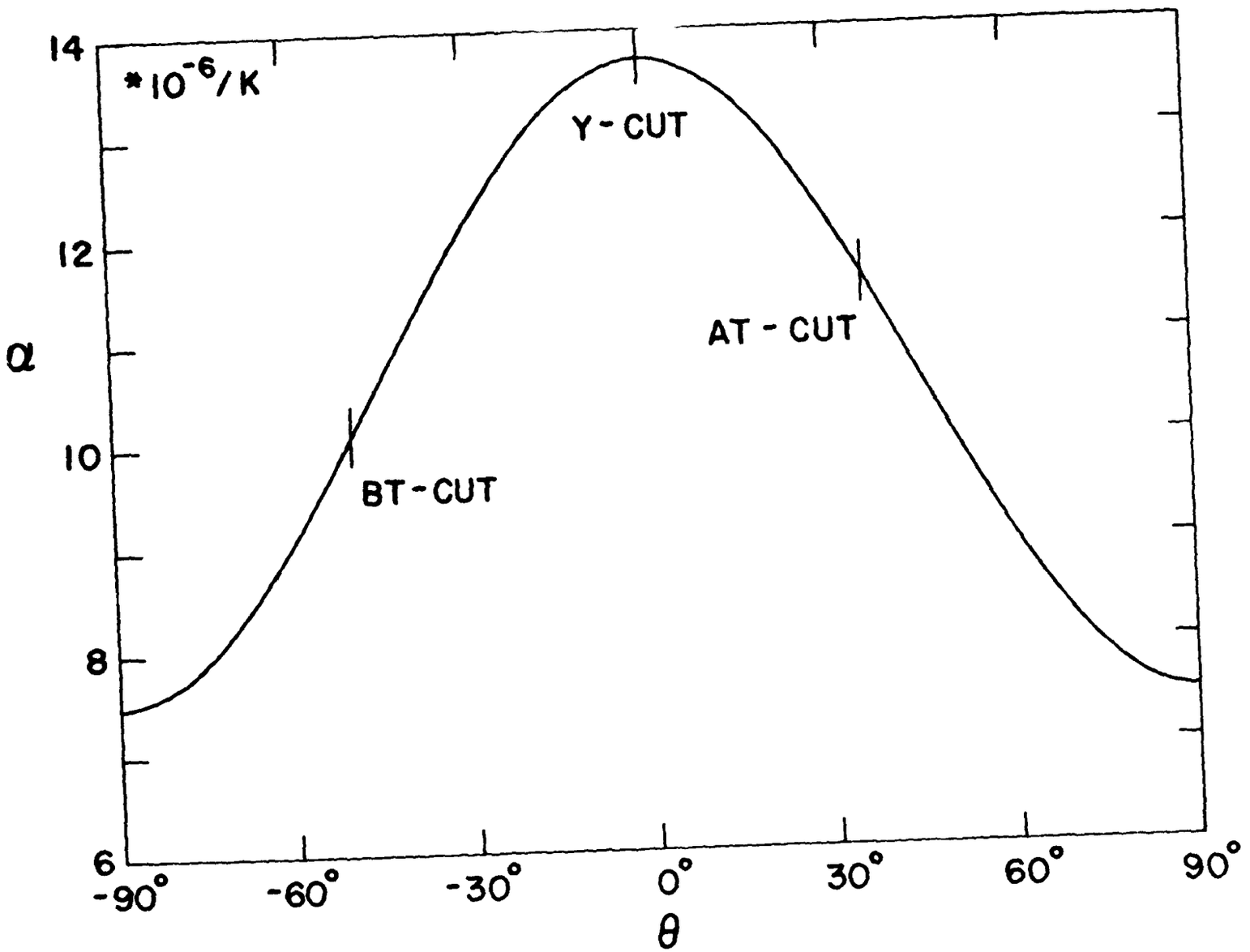

FIGURE 34. Thermoelastic Coefficient versus Theta

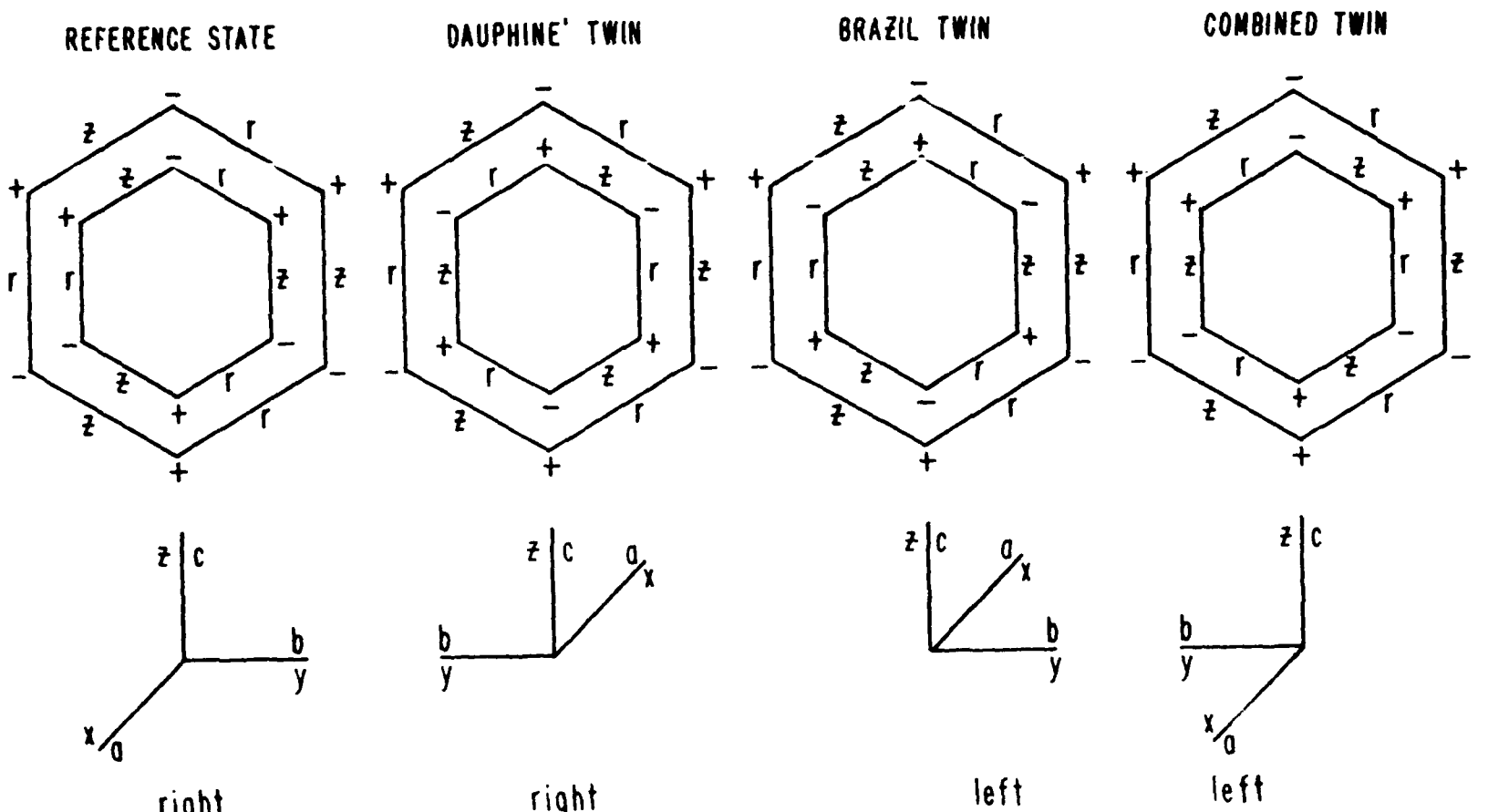

FIGURE 35. Electrical and Optical Twinning

Consider further a plate of unity area, with a fraction "a" of this area twinned. For simplicity, assume the twinning is complete throughout the thickness, and that the distribution of motion is uniform even though twinned (although we keep in mind Cady's remark, above). Then the composite e'_{26} should be:

(a) Dauphiné:

$$e'_{26} = \{(1-2a)\ e_{11}\ \cos\theta + e_{14}\ \sin\theta\} \cdot (-\cos\theta).$$

(b) Brazil:

$$e'_{26} = (1-2a)\ e_{11}\ \cos\theta + (1-2a)\ \sin\theta) \cdot (-\cos\theta).$$

(c) Combined:

$$e'_{26} = \{e_{11}\ \cos\theta + (1-2a)\ e_{14}\ \sin\theta\} \cdot (-\cos\theta).$$

In the case of Brazil twinning:

$$e'_{26}\ (\text{twinned}) = (1-2a) \cdot e'_{26}(\text{untwinned}). \qquad (16)$$

Equation (16), when written in terms of the resonator capacitance ratio becomes:

$$r\ (twinned) = r\ (untwinned)\ /\ (1-2a)^2. \qquad (17)$$

DYNAMIC THERMAL EFFECTS

It has been known for many years that abrupt temperature changes produce frequency changes in quartz vibrators that are unpredicted by static f-T characteristics such as those of Fig. 25. The dynamic thermal effect has been given a phenomenological explanation by a modification of the cubic curve to include time-dependent terms that take into account thermal gradients in the resonator and support structure.[18] The classical f-T equation

$$\frac{\Delta f}{f} = a_o\ \Delta T + b_o\ \Delta T + c_o\ \Delta T^3 \qquad (18)$$

is augmented by the addition of the term

$$(\hat{a}\ \Delta T + \hat{a}) \cdot dT/dt \qquad (19)$$

A temperature ramp (dT/dt = constant) applied to the resonator both rotates the f-T curve, through $\hat{a}$, and translates it, by means of $\hat{a}$. Figure 36 defines the desired reference temperature (which may be at either zero-slope point) at which the oven ought to be set, along with the actual oven setting point achieved, and the oven cycling range. The cycling range is

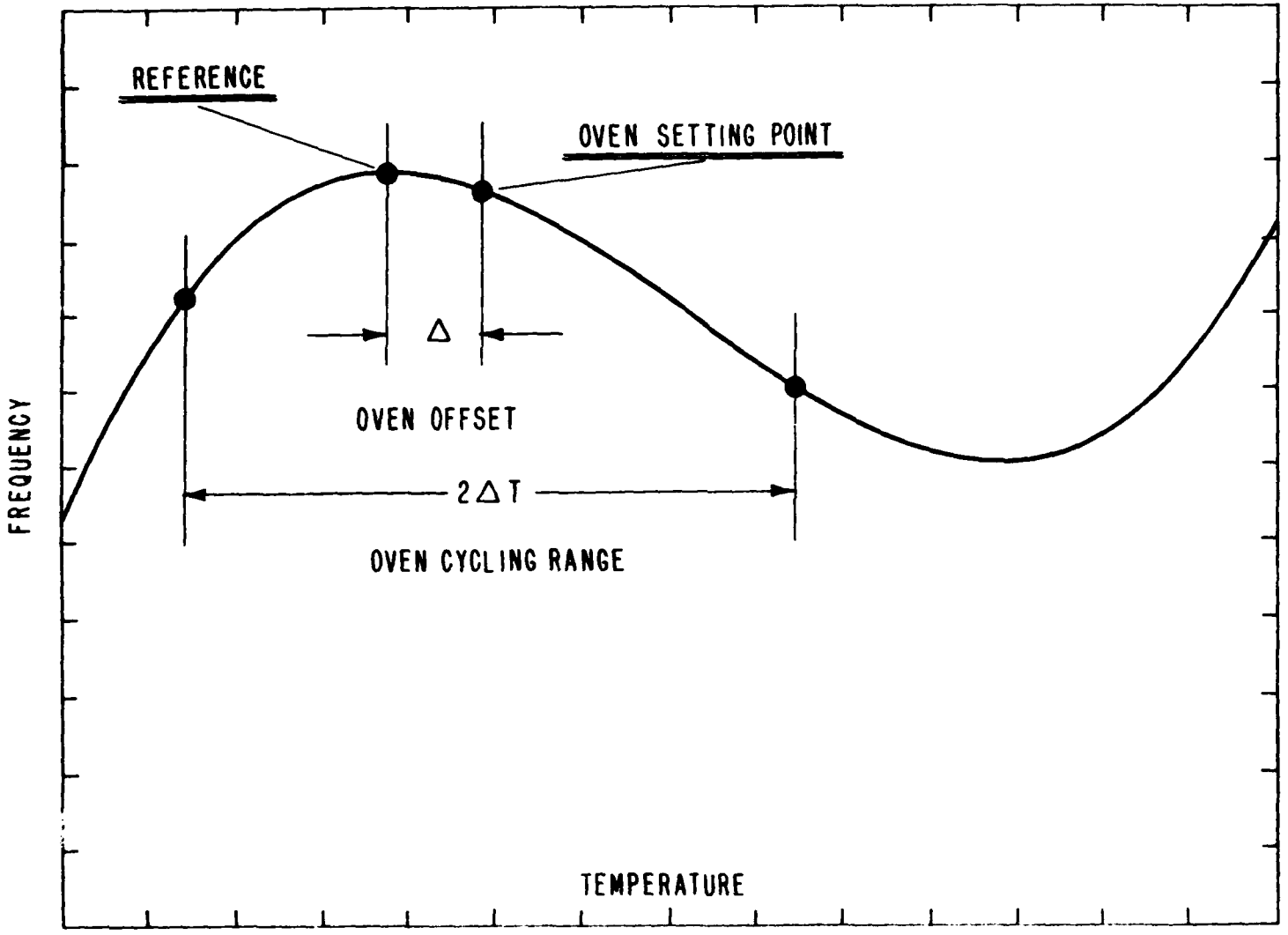

FIGURE 36. Defiritions Relating to Ovenized Oscillators

a measure of the quality of the crystal oven. The result of sinusoidal temperature variations of magnitude ΔT = 60K about the inflection temperature of the static AT cut f-T curve is shown in Fig. 37. Temperature varies as sin ωt; various ω values are shown. In Fig. 38 is given the result of variations for ΔT = 10K about the upper turning point. Figure 39 gives the result when the temperature magnitude is reduced to 5mK. In Fig. 40 the effects of ΔT = both $\frac{1}{2}$ and 1 mK on the orbit shapes is seen. Figure 41 shows the result of sinusoidal variations in temperature of magnitude $\pm\frac{1}{2}$ mK about the turning point of the static f-T curve of Fig. 25. With a period of 8 hours, the frequency change is about 3 x 10^{-1}; when the period is lengthened to 1 week, the change is still about 1 x 10^{-1}, whereas the static f-T curve would predict a change of only a few parts in 10^{-}, irrespective of cycling rate. Since thermal transients, temperature cyclings, and fluctuations cannot be entirely avoided, the dynamic temperature effect is a very important consideration for high precision resonators. The magnitude of the effect can fortunately be reduced by recourse to doubly rotated quartz cuts, specifically the SC-cut.[18,19]

AMBIENT VIBRATIONS

Insensitivity to acceleration is one of the most prominent criteria by which to judge high stability resonators. At present, the rule-of-thumb number relating frequency shift to applied acceleration is 2 x 10^{-} per g, although efforts are underway to reduce this value. (See references given in Reference 20.) It appears that a sensitivity of 1 x 10^{-11}/g is a reasonable goal for the next few years. These two sensitivity figures have been used in conjunction with published values for acceleration levels in various environments[21-26] to produce the frequency shift entries shown in Fig. 42 and Fig. 43.

From Fig. 42 and Fig. 43 it is seen that the decrease in acceleration sensitivity to parts in 10^{11} per g and beyond is highly desirable. The smallest entry in the figures is due to microseisms.[22-26] Figure 44, taken from Reference 24, shows the very interesting spectrum of microseisms observed at the earth's surface. It appears that the spectrum of displacement versus period plotted on equal log-log scales consists of portions of +2 and -2 slope peaking rather sharply at a period of about 7 seconds. The maximum amplitude of acceleration is approximately 4 micro-g's, and is constant along the +2 slope line. For oscillators with high acceleration sensitivity this source of disturbance would have to be eliminated by mounting supports even for isolated, underground installations. Building vibrations are far greater than microseisms, and their noise spectra must be considered in the installation of precision oscillators. In certain locations, the accelerations due to earthquakes must be allowed for, although the vibrations found in urban environments produce accelerations associated with earthquakes of magnitude 3-4 on the Richter scale.[23] This scale is defined, for shallow shocks, as the $\log_{10}$ of the maximum trace amplitude in micrometers with which the standard short-period torsion seismometer would register that earthquake at an epicentral distance of 100km.

Two crystal resonator structures having decreased acceleration sensi-

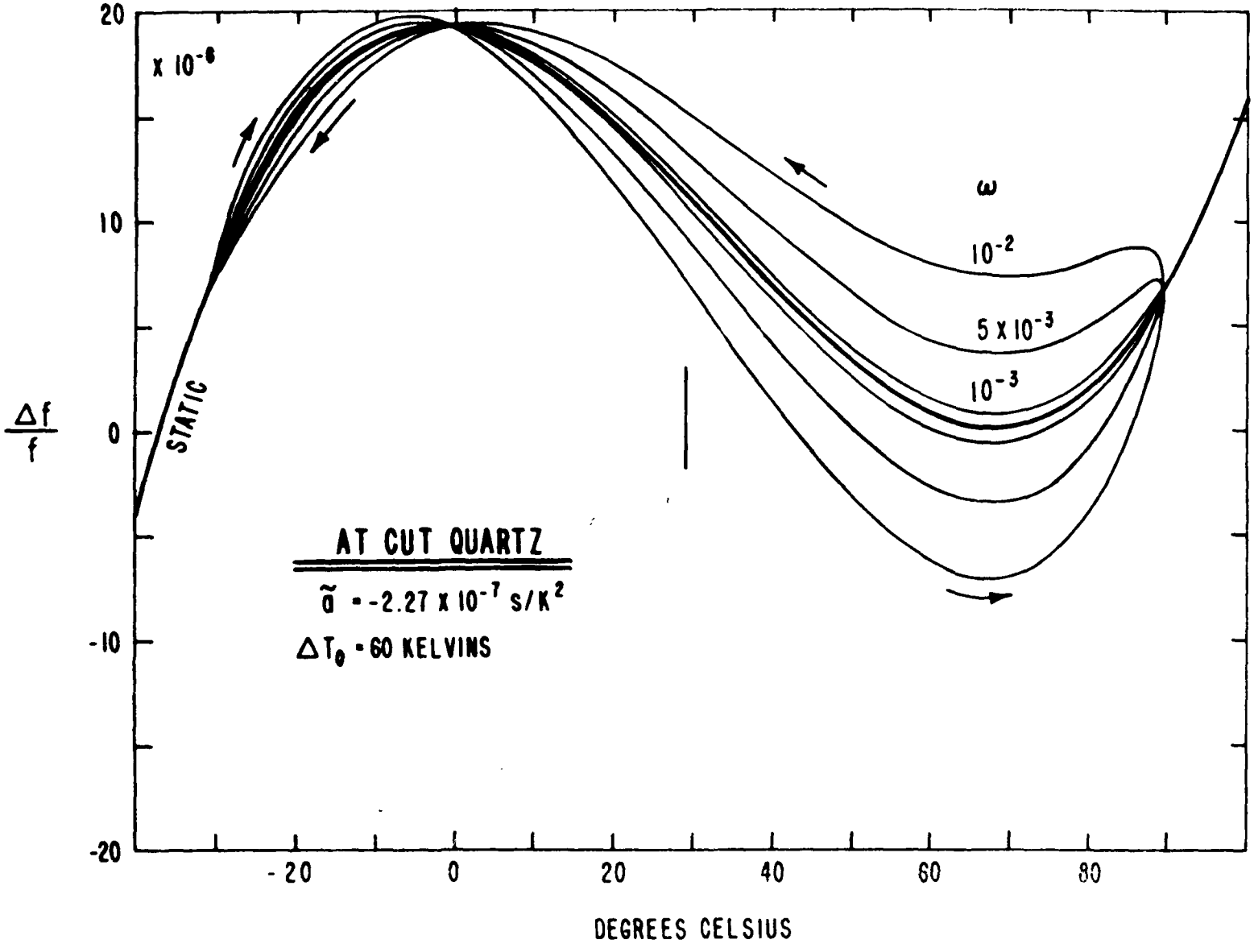

FIGURE 37. Dynamic Thermal Effect; ΔT_0 = 60K

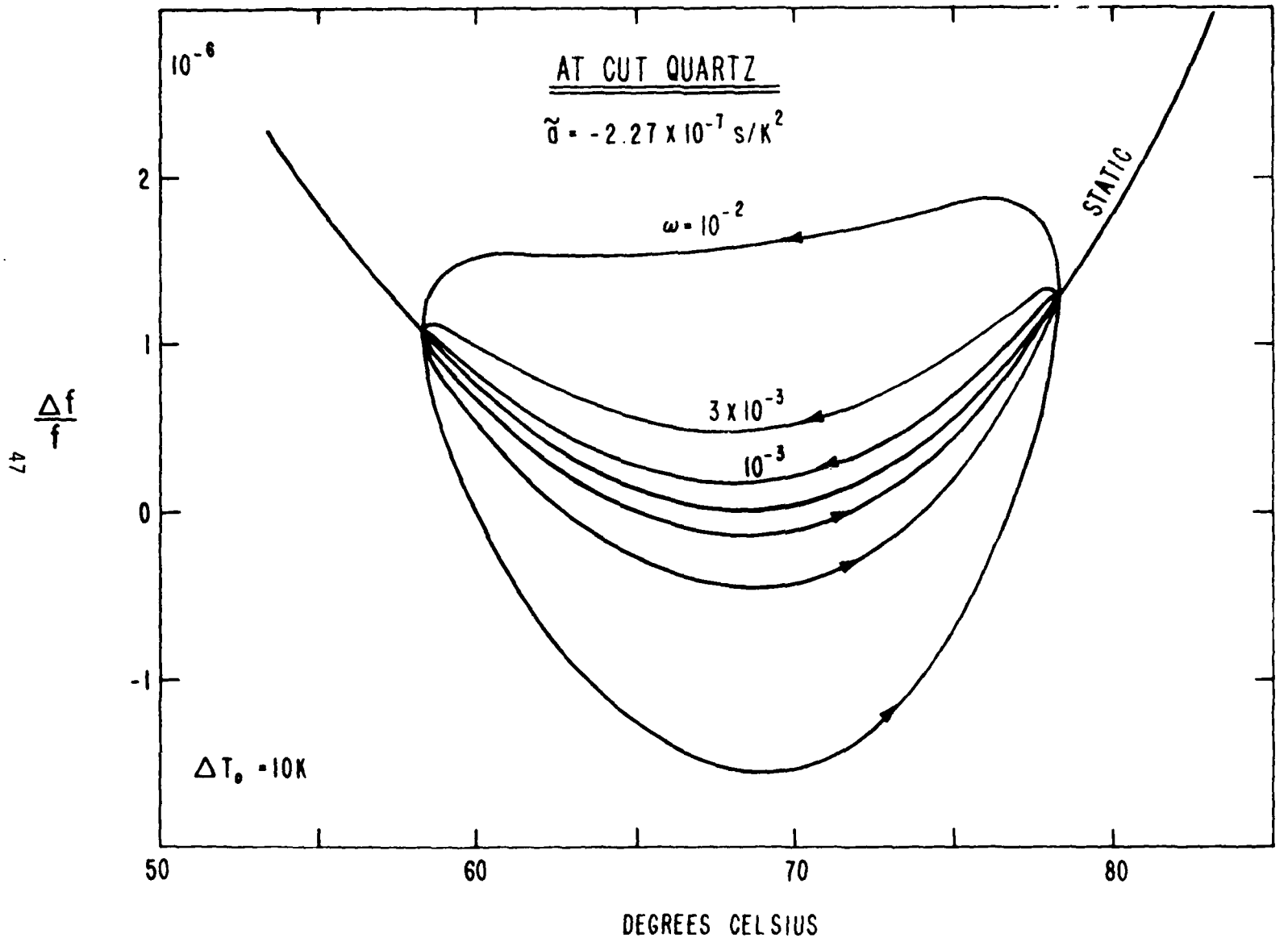

FIGURE 38. Dynamic Thermal Effect; ΔT_o = 10K

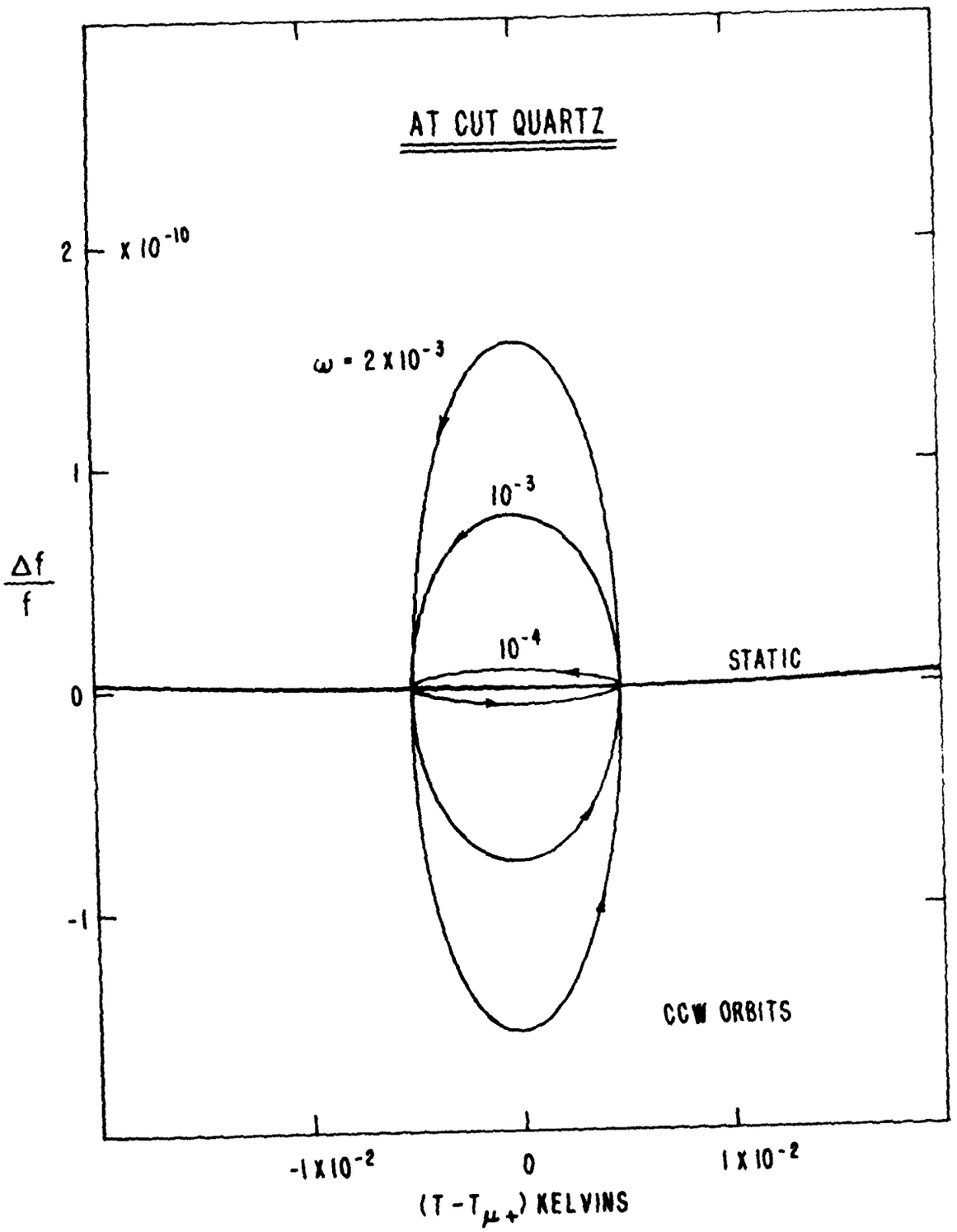

FIGURE 20 ... Thermal Effect; ΔT_0 = 5mK

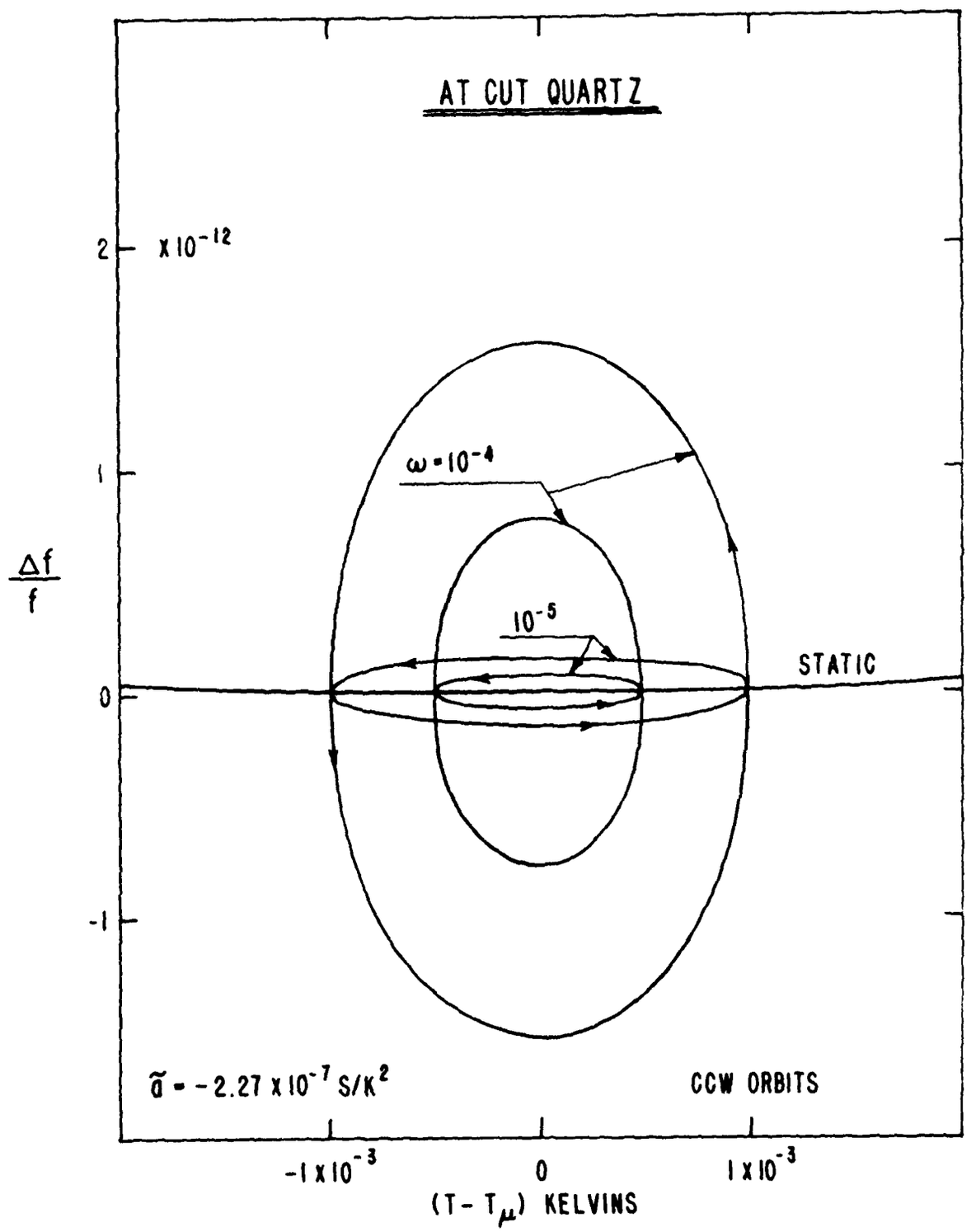

FIGURE 40. Dynamic Thermal Effect: ΔT_o = 0.5 and 1 mK

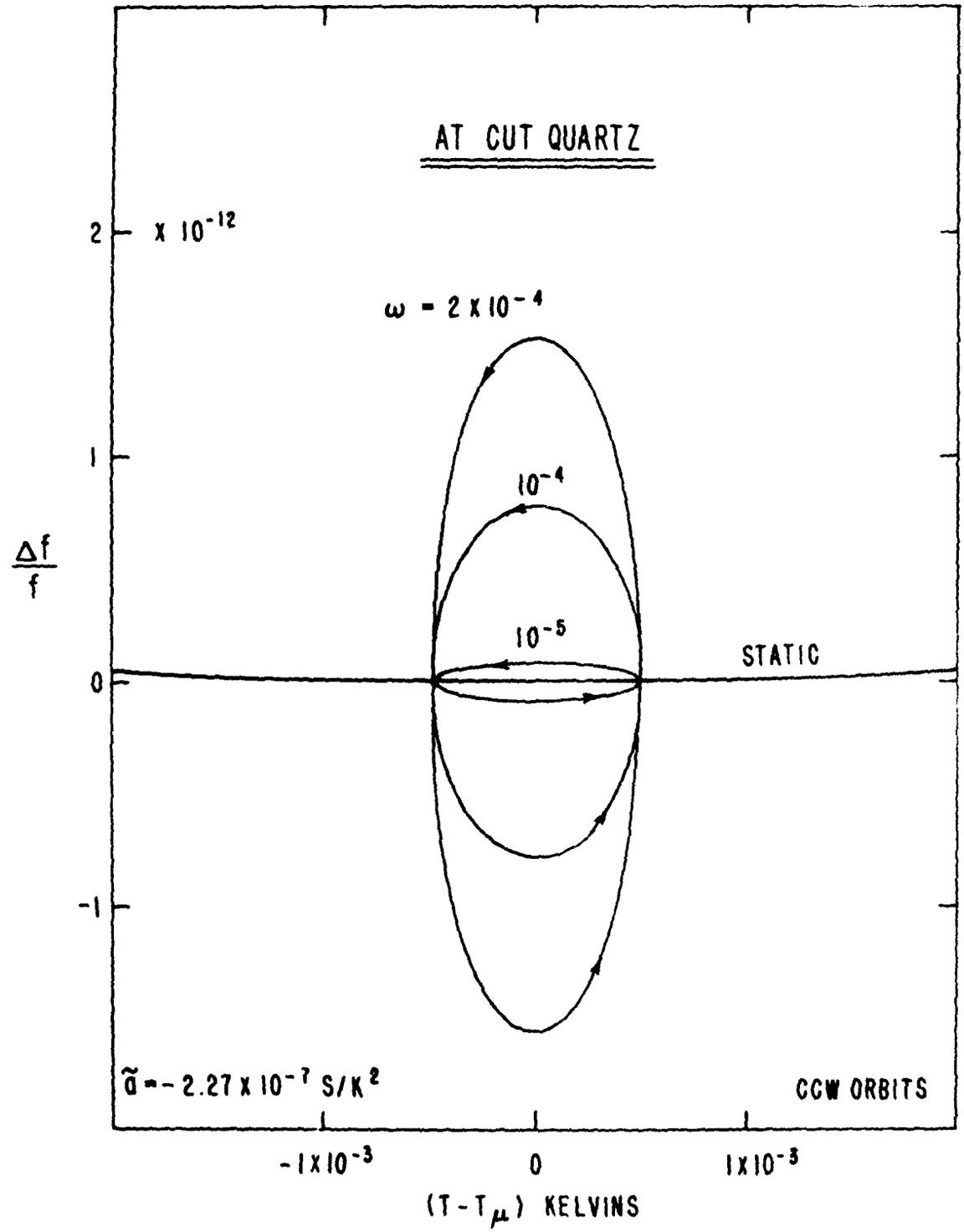

FIGURE 41. Dynamic Thermal Effect; ΔT_0 = 0.5mK

ENVIRONMENT	ACCELERATION G UNITS	OSCILLATOR SENSITIVITY	
		$2 \times 10^{-9}/G$	$1 \times 10^{-11}/G$
		FREQUENCY SHIFT	
ROAD VEHICLES			
TRACTOR-TRAILER (3-80 HZ)	0.2 PEAK	4 (-10)	2 (-12)
PANEL TRUCK	0.02 RMS	4 (-11)	2 (-13)
ARMORED PERSONNEL CARRIER	0.5 TO 3 RMS	6 (-9)	3 (-11)
RAILROADS			
STANDARD	1 PEAK	2 (-9)	1 (-11)
SOFT-RIDE	0.1 PEAK	2 (-10)	1 (-12)
CROSSING TRACK/SWITCHES	6 PEAK	1.2(-8)	6 (-11)
NORMAL COUPLING & SWITCHES	30 PEAK	6 (-8)	3 (-10)
SHIPS			
NORMAL CALM	0.02 TO 0.8	1.6 (-9)	8 (-12)
ROUGH SEAS	0.8	1.6 (-9)	8 (-12)
SLAM & EMERGENCY MANEUVERS	TO 3	6 (-9)	3 (-11)

FIGURE 42. Ambient Accelerations: Road/Rail/Ship

ENVIRONMENT	ACCELERATION G UNITS	OSCILLATOR SENSITIVITY	
		$2 \times 10^{-9}/g$	$1 \times 10^{-11}/g$
		FREQUENCY SHIFT	
AIRCRAFT			
PROPELLER	0.3 TO 5 RMS	1 (-8)	5 (-11)
HELICOPTER	0.1 TO 7 RMS	1.4(-8)	7 (-11)
JET	0.02 TO 2 RMS	4 (-9)	2 (-11)
ROCKETS			
MISSILES (BOOST PHASE)	15	3 (-8)	1.5(-10)
ABLE-I (MULTI-STAGE)	30	6 (-8)	3 (-10)
VENUS ENTRY	310 MAX.	6.2(-7)	3.1(-9)
SEISMIC			
EARTHQUAKE (EL CENTRO, CA, 1940)	0.33 MAX.	6.6(-10)	3.3(-12)
MICROSEISMS	4×10^{-6} MAX.	8 (-15)	4 (-17)
BUILDINGS (QUIESCENT)	0.02 RMS	4 (-11)	2 (-13)

FIGURE 43. Ambient Accelerations: Aircraft/Rocket/Seismic

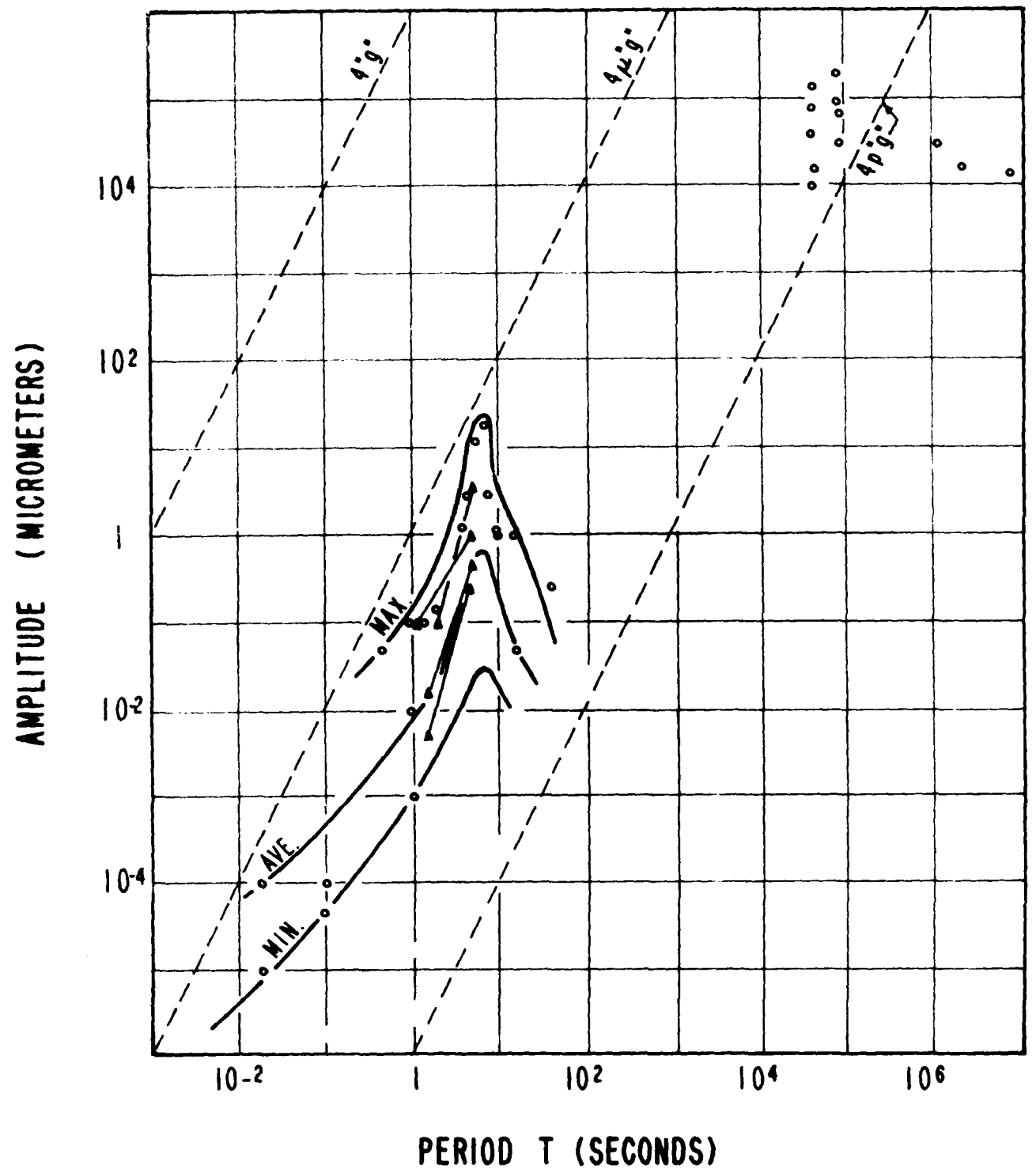

FIGURE 44. SEISMIC NOISE OF THE EARTH'S SURFACE

tivity for accelerations in the thickness direction are the ring-supported and grooved configurations.[20,27] Several varieties of these are displayed in Fig. 45 and Fig. 46; Fig. 45 gives the underlying rationale for using ring-supported resonators when the acceleration is applied in the thickness direction. The frequency shift is proportional to displacement of the central membrane, and because of the double cantilever edge conditions this displacement is smaller than in conventional simply supported resonators. Figure 47 defines the parameters pertinent to the geometry of the plano-convex ring-supported resonator. These parameters are listed below for resonator B-4: (in mm)

$$\phi_o = 7.950; \quad \phi_i = 6.020; \quad \phi_e = 4.064;$$

$$t_o = 1.000; \quad t_i = 0.662; \quad t_c = 0.700;$$

$$R = 120.$$

The measured frequency constant was N = 1.770 MHz - mm. In Fig. 48 is shown the experimental frequency shift versus acceleration for resonator I-4, an AT-cut, plano-convex, ring-supported resonator with acceleration applied along the X axis. The frequency shifts are seen to saturate at high g levels, leading to the conclusion that the acceleration-frequency sensitivity coefficient is nonlinear. Figure 49 gives the corresponding curves for resonator B-4. The concavo-convex ring-supported geometry in Fig. 46 is a preferred structure for unidirectional acceleration loads directed toward the radii of curvature. The resonator center is thicker than the junction to the ring to permit energy trapping.

ACOUSTIC VISCOSITY

One of the foremost reasons for using quartz as a vibrator material is its extremely low acoustic attenuation, as manifested in the large values of quality factor (Q) measured, typically as much as[28]

$$Q \approx 10^7 / f_o, \tag{20}$$

at room temperature, where f_o is the operating frequency in MHz. This is shown in Fig. 50. The values in (20) are met, and exceeded, only by very careful design of the mounting structure at frequencies below a few tens of MHz[28]; above these frequencies the intrinsic internal friction of the material predominates. Calculation of the intrinsic loss follows from the measurement of the elements η_{ij} of the acoustic viscosity tensor.[29]

For the rotated-Y-cuts of quartz, the piezoelectrically driven shear mode has an effective viscosity of

$$\eta' = \eta_{66} \cos^2\theta + \eta_{44} \sin^2\theta + 2\eta_{14} \sin\theta \cos\theta. \tag{21}$$

Substituting the elastic stiffness c_{ij} for the viscosities in (21) yields

CRYSTAL RESONATORS

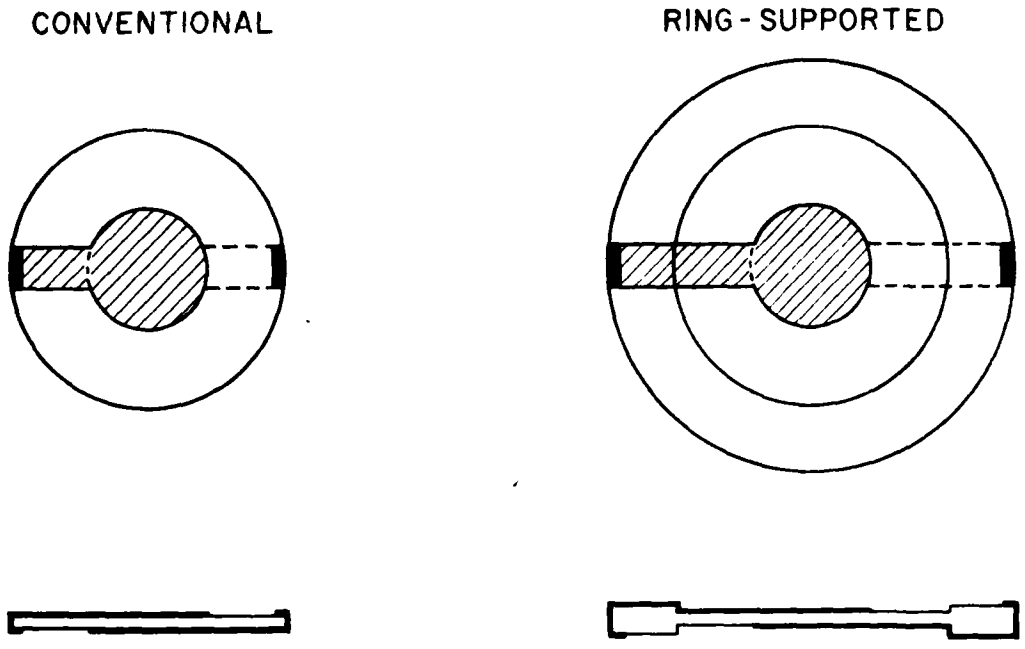

SIMPLY SUPPORTED:

(a) EDGE FORCES; ZERO DISPLACEMENTS

(b) NO EDGE TORQUES; NONZERO SLOPES

DOUBLE CANTILEVER:

(a) EDGE FORCES; ZERO DISPLACEMENTS

(b) EDGE TORQUES; ZERO SLOPES

FIGURE 45. Conventional and Ring-Supported Resonators

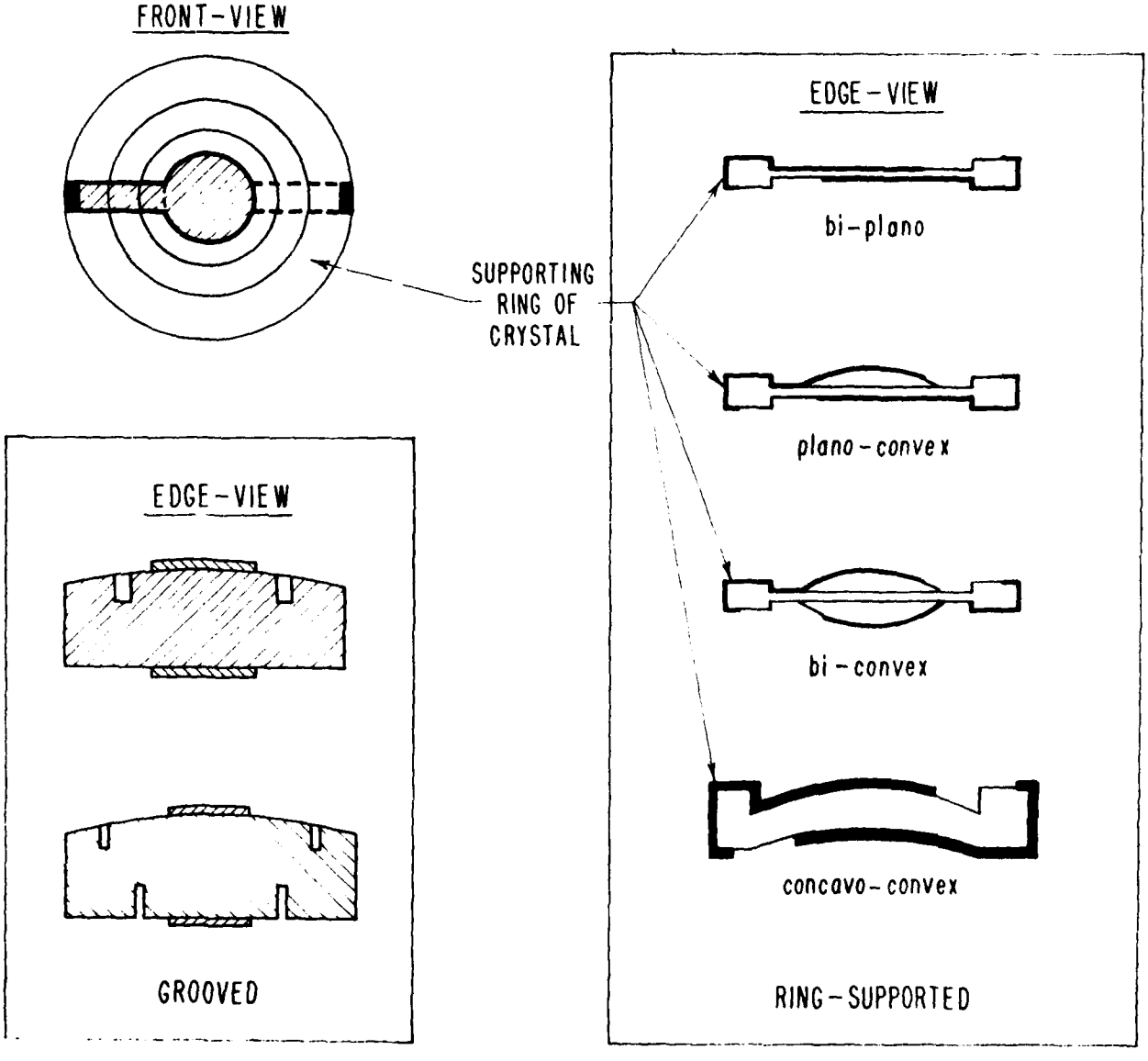

FIGURE 46. Ring-Supported and Grooved Crystal Resonators

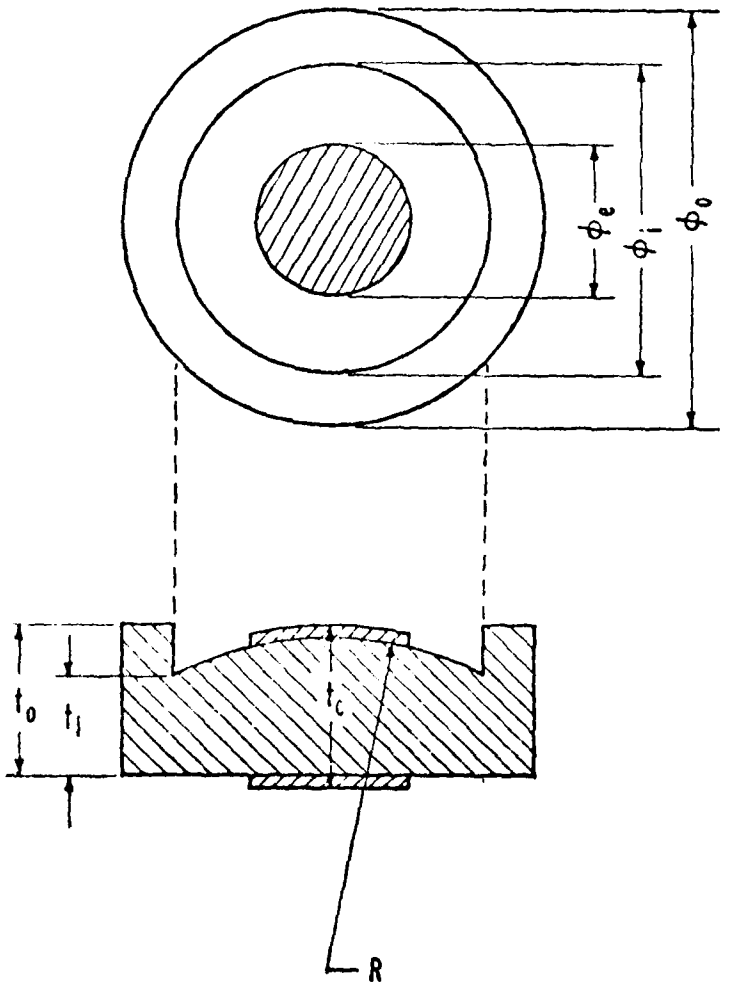

FIGURE 47. Definitions of Ring-Supported Resonator Parameters

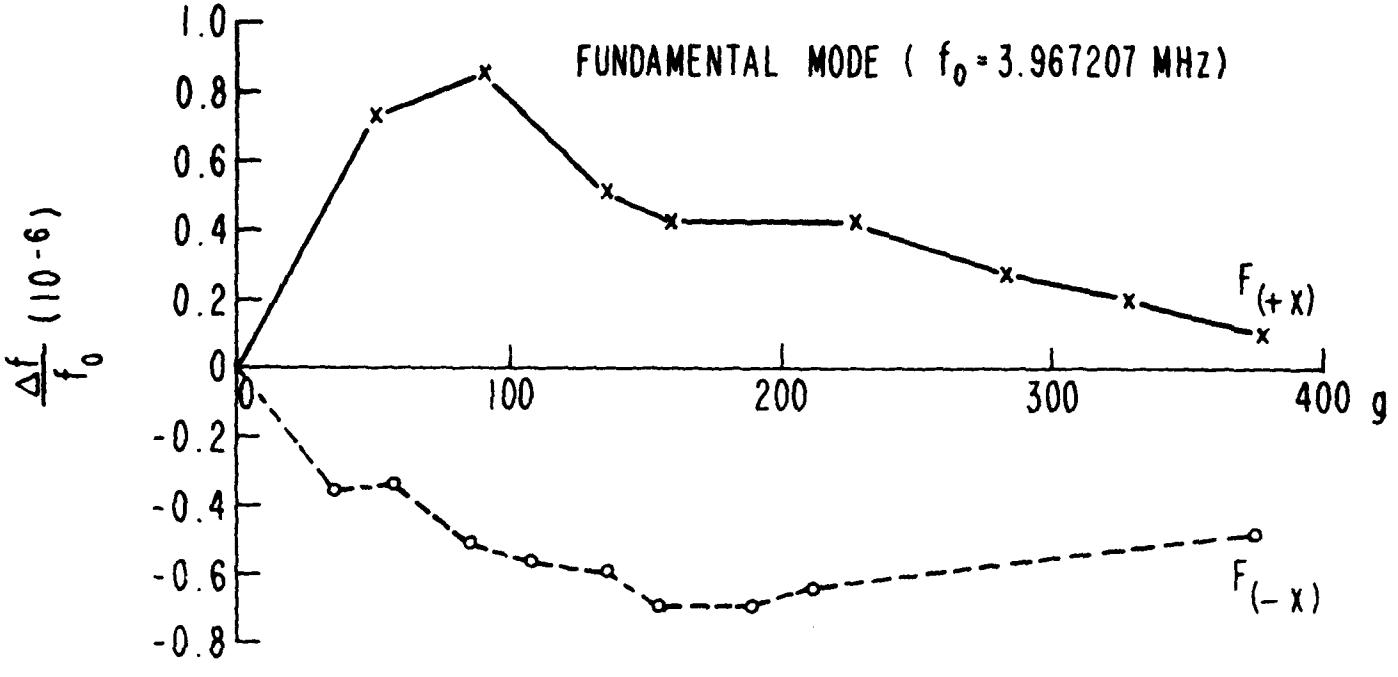

FIGURE 48. ACCELERATION FREQUENCY EFFECTS OF X-AXIS DIRECTION FOR SAMPLE NO. T-4

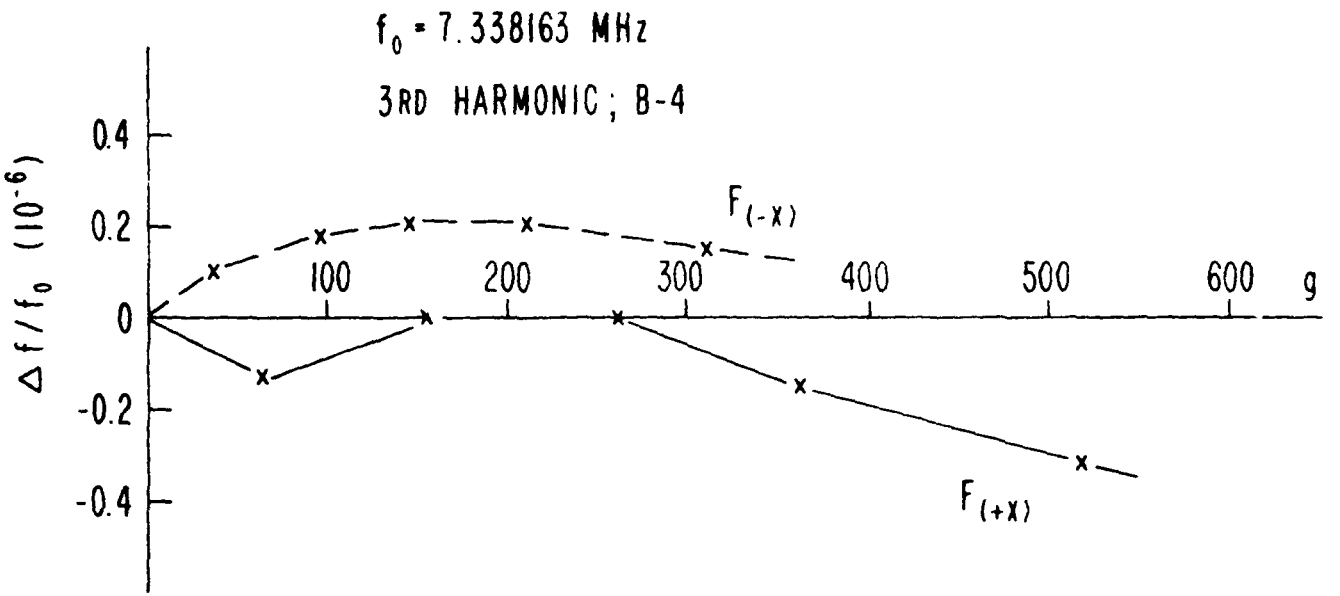

FIGURE 49.
ACCELERATION-FREQUENCY EFFECTS OF X-AXIS DIRECTION FOR SAMPLE NO. B-4

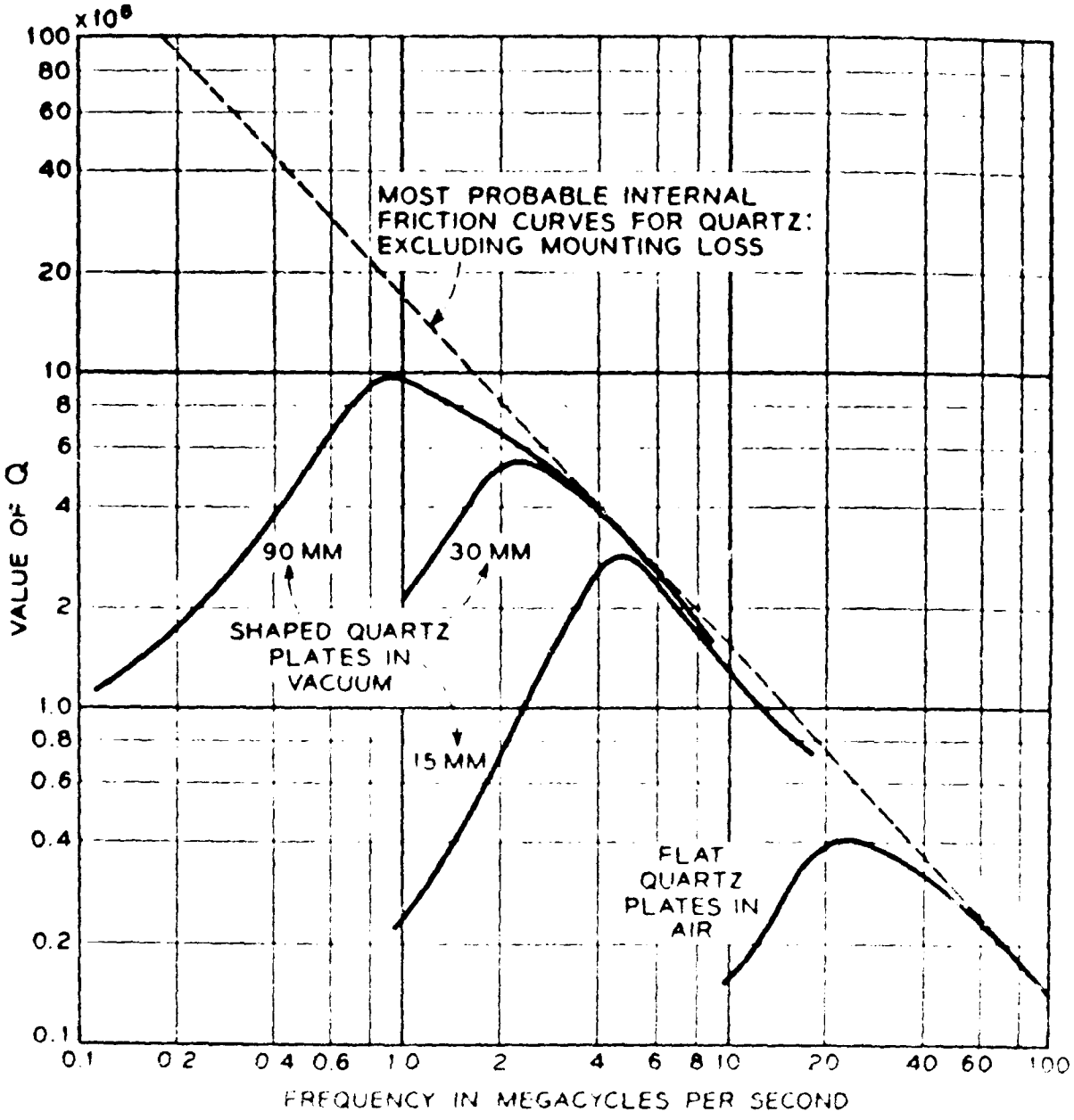

FIGURE 50. Experimental Values of Q versus Frequency for Quartz

the corresponding effective stiffness c' for this pure mode. Then the motional time constant τ_1 representing the intrinsic losses is [30,31]

$$\tau_1 = \eta' / c'. \tag{22}$$

Since τ_1 is also equal to

$$\tau_1 = R_1 C_1 = 1/(\omega_o Q), \tag{23}$$

both the intrinsic Q at an operating frequency $f_o = \omega_o /2\pi$ and the motional resistance R_1 of the equivalent electrical network may be computed, as the motional capacitance is separately calculated.

When mounting losses cannot be neglected, it is found that these losses depend upon the plate diameter-to-thickness ratio ζ in the following manner:

$$\tau_1 (\zeta) = \tau_{1_i} \left(1 + (\zeta/\zeta_o)^2\right) , \tag{24}$$

where τ_{1_i} is the intrinsic value of τ_1, and depends on the material used, being 10 to 15 femtoseconds for room temperature quartz, and ζ_o is a function of the resonator design, with ζ_o = 60 a good average. This is demonstrated by Fig. 51 and Fig. 52, where the data of Fig. 50 and additional data are plotted against ζ. It is seen that for $\zeta < \zeta_o$ the loss, as reflected in τ_1 is governed by a curve with -2 slope; beyond ζ_o, the curve is constant, with zero slope. The calculation of η has been extended to the general doubly rotated thickness mode case.[14]

COSMIC RAYS

Cosmic rays, and other unshieldable radiation sources, produce cumulative contributions to long-term aging. Knowing the radiation sensitivity of natural and cultured quartz under a variety of treatments permits an evaluation of resonator performance due to this source.

The raw data[32] are contained in Fig. 53, Fig. 54 and Fig 55. Using the values for the photon flux given and a number of simplifying assumptions, the frequency shift due to this source is given in Fig. 56 for two values of quartz sensitivity. The unit "rad" is defined as "The standard unit of absorbed dose, equal to energy absorption of 100 ergs per gram (0.01 joules per kilogram)."[40] The assumptions used are (a) unprotected crystal, (b) total incident energy is absorbed, and (c) sea level flux. $\mathcal{F}_p$ is the photon flux in photons / cm^2 - sec. The fractional frequency shift $\Delta f/f$ is specified as 10^{-S}; the time $\tau(s)$ for this shift to occur is

$$\tau(s) \approx 5 \times 10^{12-S} \text{ years.} \tag{25}$$

Similarly for neutrons, assumptions (a) and (b) listed above, plus the sensitivity value $\Delta f/f \sim 10^{-21}$ cm^2/n. lead to the order-of magnitude figures given in Fig. 57 for three values of altitude. $\mathcal{F}_n$ is the neutron

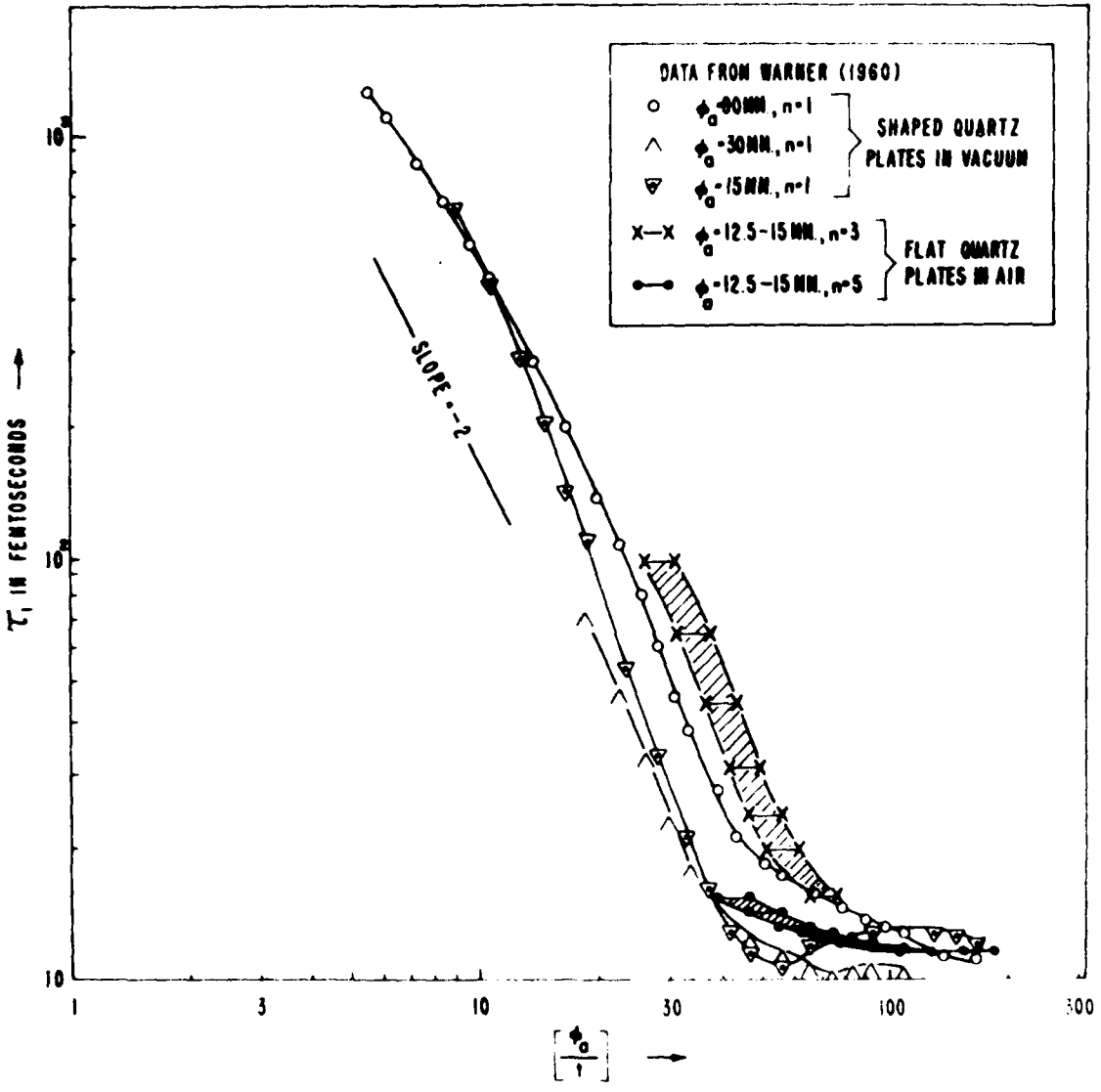

FIGURE 51. TIME CONSTANT, τ_1, FOR AT-CUT QUARTZ PLATES AS A FUNCTION OF DIAMETER-THICKNESS RATIO, $\frac{\phi_o}{t}$, AVERAGE VALUES

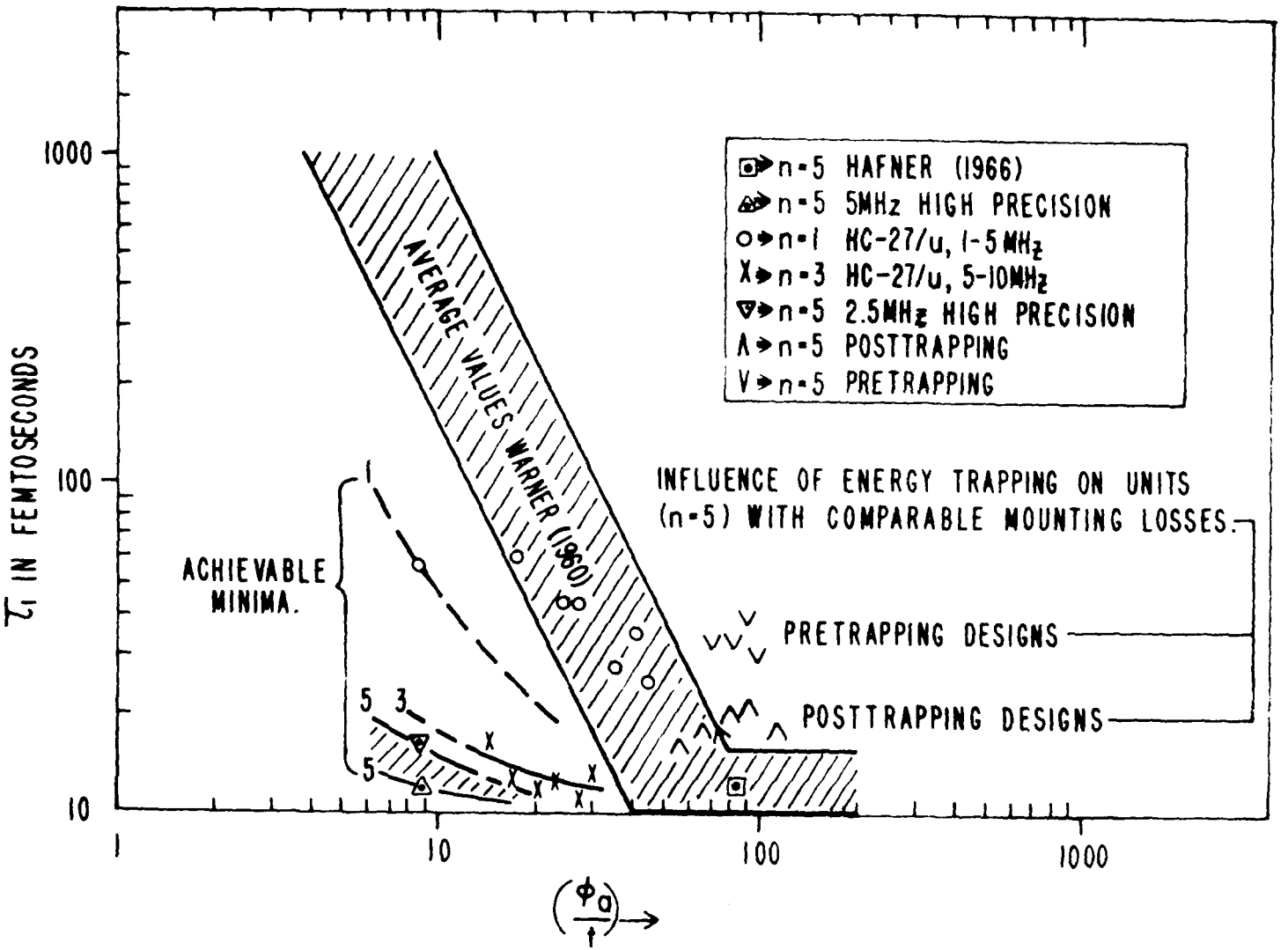

FIGURE 52. TIME CONSTANT, τ_1, FOR AT-CUT QUARTZ PLATES IN VACUUM AS A FUNCTION OF DIAMETER-THICKNESS RATIO, ϕ_a/t.

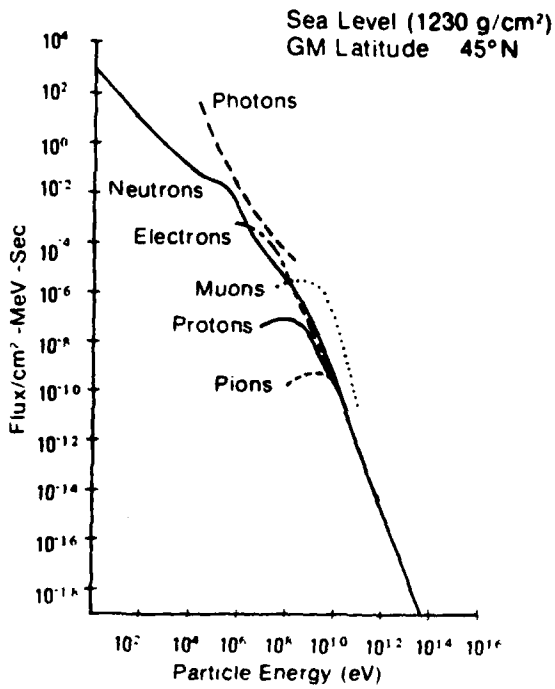

FIGURE 53. Cosmic Ray Flux versus Particle Energy at Sea Level

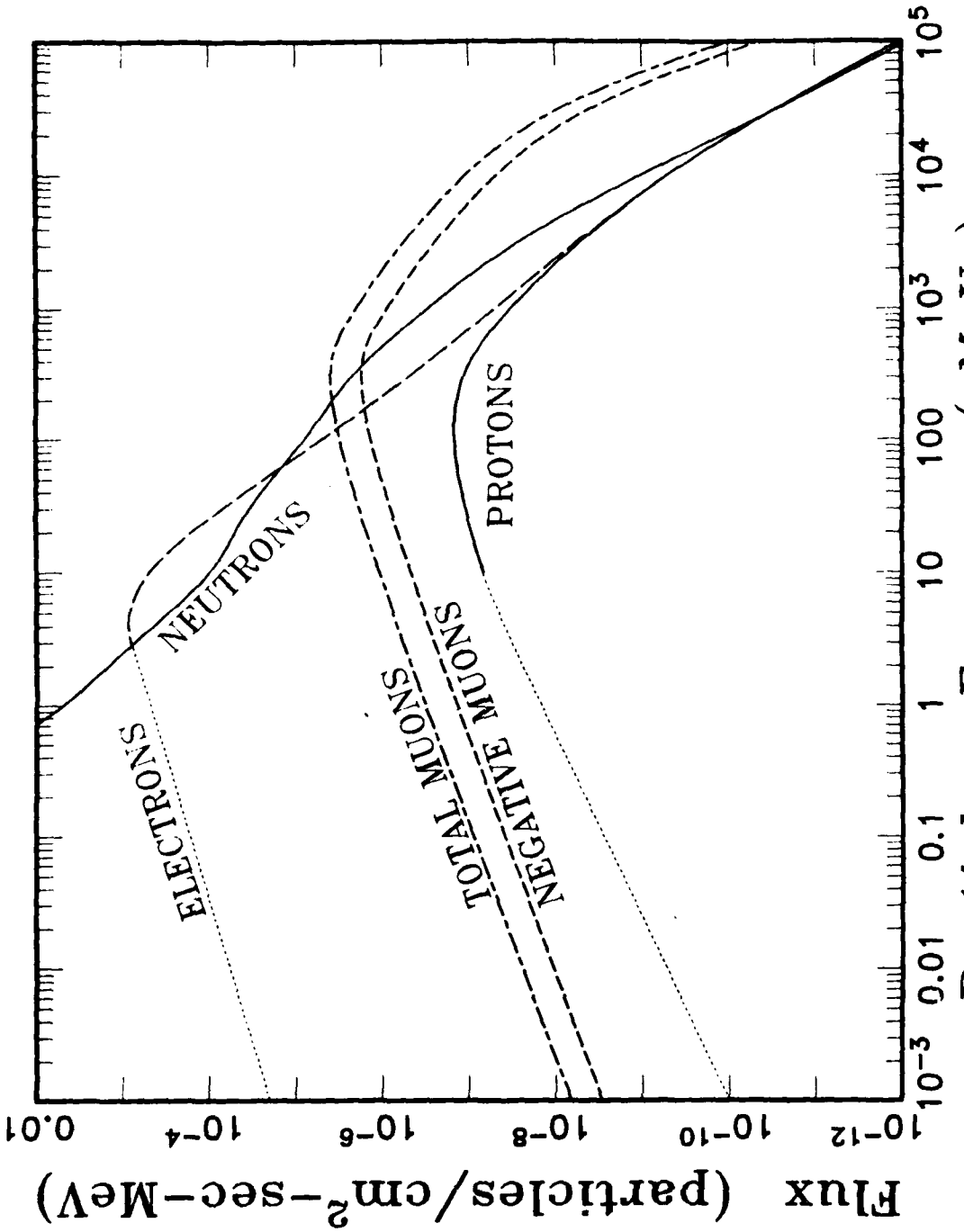

FIGURE 54. Flux versus Energy in MeV at Sea Level

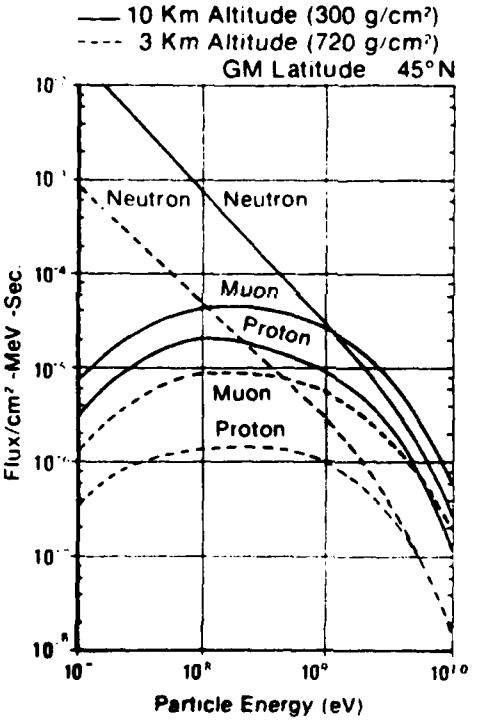

FIGURE 55. Flux versus Energy at 3 and 10 km Height

SPECIFICATION: $\Delta F/F = 10^{-S}$

TIME FOR SPECIFIED SHIFT: $\tau(s) \simeq 5*10^{12-S}$ YEARS

	NATURAL QUARTZ	SWEPT CULTURED
$\Delta F/F$	$\sim 10^{-11}$/RAD	$\sim 10^{-12}$/RAD
$\mathcal{F}_P$	$\sim$ 1	$\sim$ 1
$\tau(12)$	$\sim$ 5 YRS.	$\sim$ 50 YRS.
$\tau(14)$	$\sim$ 5 HOURS!	$\sim$ 0.5 YRS.

NOTES: 1/ UNPROTECTED CRYSTAL

2/ TOTAL ENERGY ABSORBED

3/ SEA LEVEL

4/ $\mathcal{F}_P$ IN PHOTONS/CM^2-SEC

FIGURE 56. Frequency Shift for Photons

SPECIFICATION: $\Delta F/F = 10^{-S}$

TIME FOR SPECIFIED SHIFT: $\tau(s) \simeq 10^{14-S}/4\mathcal{F}_N$ YEARS

	SEA LEVEL	3 KM	10 KM
$\mathcal{F}_N$	$\sim 10^{-3}$	$\sim 10^{-2}$	$\sim$ 0.6
$\tau(12)$	$\sim$ 25,000 YRS.	$\sim$ 2,500 YRS.	$\sim$ 4 YRS.
$\tau(14)$	$\sim$ 250 YRS.	$\sim$ 25 YRS.	$\sim$ 16 DAYS!

NOTES: 1/ UNPROTECTED CRYSTAL

2/ TOTAL ENERGY ABSORBED

3/ $\Delta F/F \sim 10^{-21}$ CM^2/NEUTRON

4/ $\mathcal{F}_N$ IN NEUTRON-SEC/CM^2

FIGURE 57. Frequency Shift for Neutrons

flux in neutron-sec/cm^2. The fractional frequency shift is specified as 10^{-S}, and the time $\tau(s)$ to reach this shift is

$$\tau(s) \simeq 10^{14-S} / 4\mathcal{F}_n \text{ years.} \qquad (26)$$

CONCLUSION

Over the years, the stabilities of precision quartz oscillators have improved according to a simple law. With frequency stability written as $\Delta f/f = 10^{-S}$, s is given by $s = 6 + 0.1(Y-X)$; Y is the year date and $x = 1920$ for large-scale production models; this is seen in Fig. 58. Laboratory oscillators, therefore, can be projected to have stabilities in the 10^{-14} range in the time frame 2000 if the current rate of improvement is maintained. There do not appear to be intrinsic impediments to achieving 10^{-14} stabilities with quartz elements by 2000, but in order to do so the various "subtle" effects affecting stability will have to be subjected to increasingly fine scrutiny. Figure 59 gives a broad view of technology progression for crystal resonators from 1945 onward.[42] The most interesting developments are yet to come.

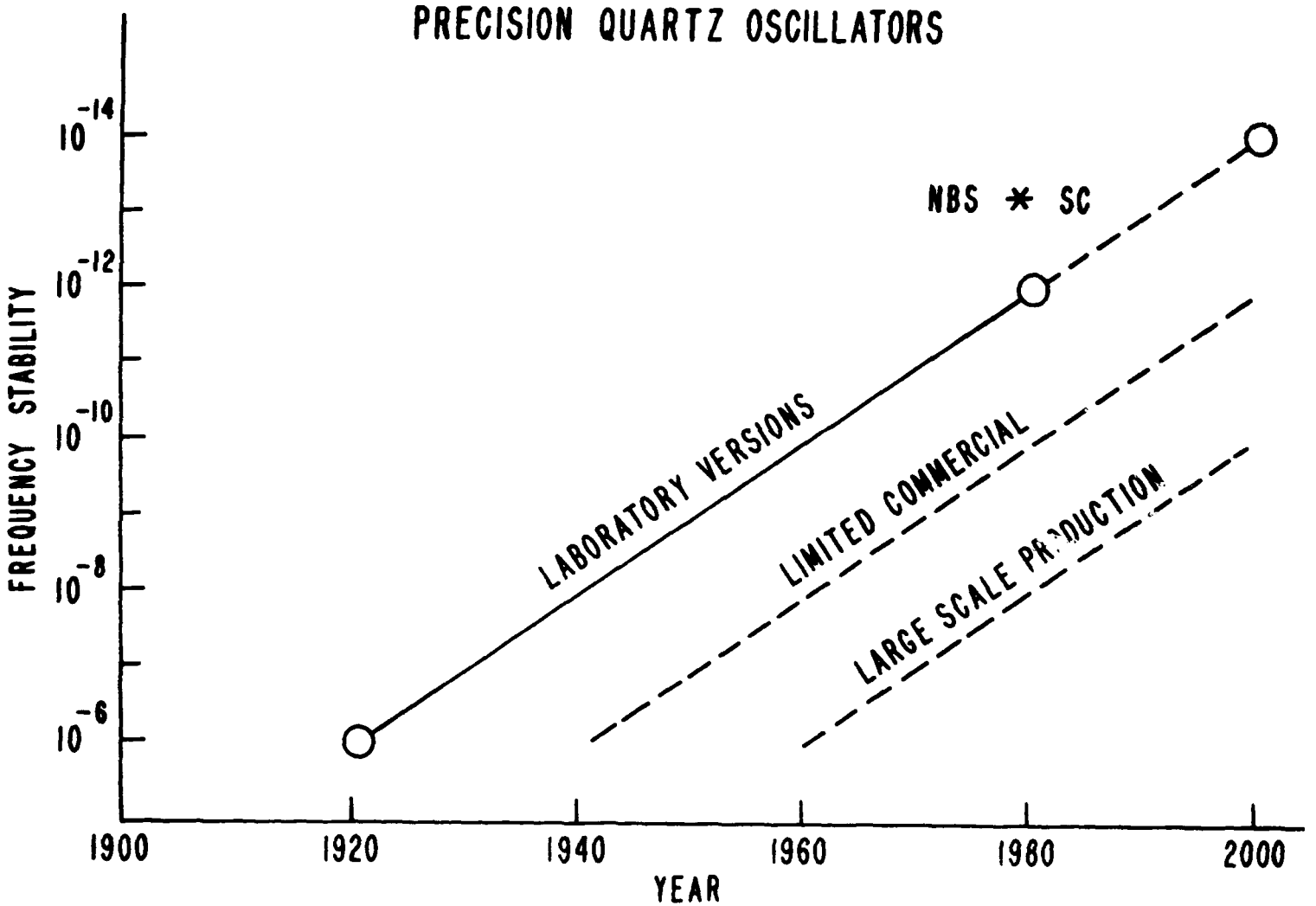

FIGURE 58. Frequency Stability versus Year

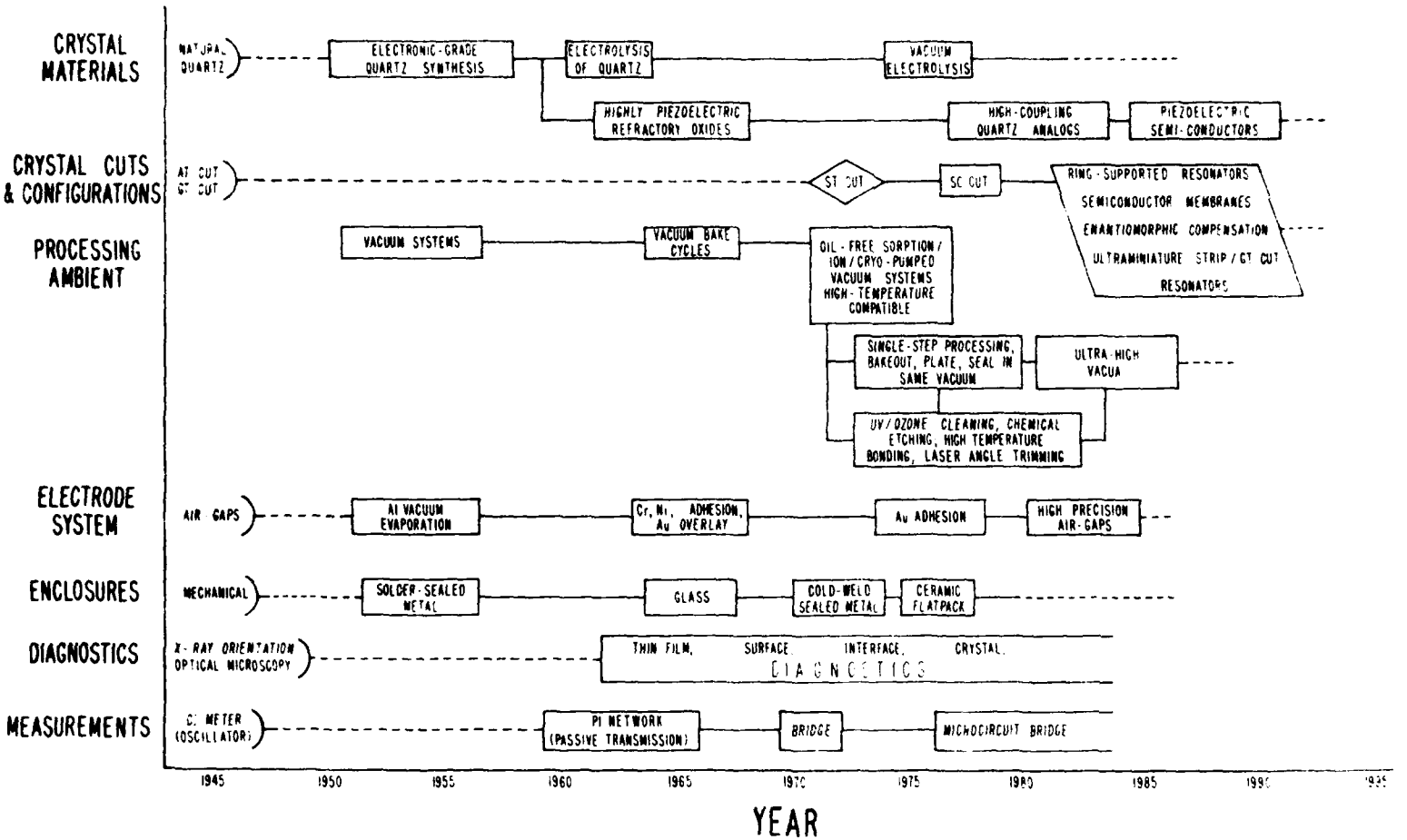

FIGURE 59. Progression in Crystal Technology

REFERENCES

1. W.G. Cady, Piezoelectricity, McGraw-Hill, New York, 1946; Dover, New York, 1964, p. 287.

2. J.A. Barnes, "Basic Concepts of Precise Time and Frequency", in Time and Frequency: Theory and Fundamentals, (B.E. Blair, ed.), National Bureau of Standards Monograph 140, Washington DC 20402, May 1974, Chapter 1, pp. 1-40.

3. A. Ballato and T.J. Lukaszek, "Mass-Loading of Thickness-Excited Crystal Resonators Having Arbitrary Piezo-Coupling," IEEE Trans. Sonics Ultrason., vol. SU-21, October 1974, pp. 269-274.

4. A. Ballato, "Quartz Resonators in Magnetic Fields," to be published.

5. A. Ballato and T. Lukaszek, "Distributed Network Modeling of Bulk Waves in Crystal Plates and Stacks," Technical Report ECOM-4311, US Army Electronics Command, Fort Monmouth, NJ 07703, May 1975, 19 pp.

6. B.J. Isherwood and C.A. Wallace, "The Analysis of Unwanted-Mode Vibration Patterns in AT-Cut Quartz Oscillator Crystals, Revealed by X-Ray Diffraction Topography: I. Interpretation of the X-Ray Topographs," J. Phys. D., vol. 8, 1975, pp. 1827-1842.

7. F.N. Goodall and C.A. Wallace, "The Analysis of Unwanted-Mode Vibration Patterns in AT-Cut Quartz Oscillator Crystals, Revealed by X-Ray Diffraction Topography: II. A Partial Theoretical Description of the Unwanted Mode," J. Phys. D., vol. 8, 1975, pp. 1843-1850.

8. A. Ballato and R. Tilton, "Electronic Activity Dip Measurement," IEEE Trans. Instrum. Meas., vol. IM-27, March 1978, pp. 59-65.

9. M. Planat and D. Hauden, "Nonlinear Properties of Bulk and Surface Acoustic Waves in Piezoelectric Crystals," Ferroelectrics, in press.

10. A. Ballato, "Frequency-Temperature-Load Capacitance Behavior of Resonators for TCXO Application," IEEE Trans. Sonics Ultrason., vol. SU-25, July 1978, pp. 185-191.

11. A. Ballato and T. Lukaszek, "Mass-Loading of Thickness-Excited Crystal Resonators Having Arbitrary Piezo-Coupling," IEEE Trans. Sonics Ultrason., vol. SU-21, October 1974, pp. 269-274.

12. A. Ballato and T. Lukaszek, "Higher-Order Temperature Coefficients of Frequency of Mass-Loaded Piezoelectric Crystal Plates," Proc. 29th Ann. Freq. Control Symp., May 1975, pp. 10-25.

13. A. Ballato, "Apparent Orientation Shifts of Mass-Loaded Plate Vibrators," Proc. IEEE, vol. 64, September 1976, pp. 1449-1450.

14. A. Ballato, "Doubly Rotated Thickness Mode Plate Vibrators," in Physical Acoustics (W.P. Mason and R.N Thurston, eds.), vol. 13, 1977, pp. 115-181. Academic Press, New York.

15. E. Knolmayer, "Exact Netplane Data for Quartz, $LiTaO_3$, $LiNbO_3$ and berlinite," Proc. 34th Ann. Freq. Control Symp., May 1980, pp. 102-111.

16. C. Frondel, The System of Mineralogy. Wiley, New York, 1962, Seventh Edition, vol. 3.

17. J. Gualtieri and A. Ballato, "Evaluation of Alpha $AlPO_4$ for Advanced Acoustic Wave Devices," Technical Report DELET-TR-81-15, US Army Electronics R&D Command, Fort Monmouth, NJ 07703, August 1981, 46 pp.

18. A. Ballato, "Static and Dynamic Behavior of Quartz Resonators," IEEE Trans. Sonics Ultrason., vol. SU-26, July 1979, pp. 299-306.

19. A. Ballato and J.R. Vig, "Advances in the Stability of High Precision Crystal Resonators," Proc. 11th Ann. Precise Time and Time Interval Applications and Planning Meeting, Greenbelt, MD 20771, November 1979, pp. 403-438.

20. A. Ballato, "Crystal Resonators with Increased Immunity to Acceleration Fields," IEEE Trans. Sonics Ultrason., vol. SU-27, July 1980, pp. 195-201.

21. AMC Pamphlet 706-117, Engineering Design Handbook, "Environmental Series, Part Three, Induced Environmental Factors," HQ, US Army Materiel Command, Alexandria, VA 22333, January 1976, Chapters 4, 5, & 6.

22. C.M. Harris and C.E. Crede, Eds., Shock and Vibration Handbook, McGraw-Hill, New York 1961. Volume 1, Basic Theory and Measurements; Volume 2, Data Analysis, Testing, and Methods of Control; Volume 3, Engineering Design and Environmental Conditions.

23. C.F. Richter, "Instrumental Earthquake Magnitude Scale," Bull. Seismol. Soc. Amer., vol. 25, January 1935, pp. 1-32.

24. J.N. Brune and J. Oliver, "The Seismic Noise of the Earth's Surface," Bull. Seismol. Soc. Amer., vol. 49, October 1959, pp. 349-353.

25. J.W. Guyton, "Review of Seismological Information on Ground Vibrations," Technical Report No. 63-50, The Geotechnical Corporation, Garland, TX, May 1963, 13 pp.

26. United Kingdom Atomic Energy Authority, The Detection and Recognition of Underground Explosions, Whitefriars Press, London, 1965, 118 pp.

27. M. Nakazawa, T. Lukaszek, and A. Ballato, "Force- and Acceleration-Frequency Effects in Grooved and Ring-Supported Resonators," Proc. 35th Ann. Freq. Control Symp., Ft. Monmouth, NJ 07703, in press.

28. A.W. Warner, "Design and Performance of Ultraprecise 2.5-mc Quartz Crystal Units," Bell Syst. Tech. J., vol. 39, Sept. 1960, pp. 1193-1217.

29. J. Lamb and J. Richter, "Anisotropic Acoustic Attenuation with New Measurements for Quartz at Room Temperature," Proc. Roy. Soc. London, vol. 293A, 1966, pp. 479-492.

30. G.K. Guttwein, T.J. Lukaszek, and A. Ballato, "Practical Consequences of Modal Parameter Control in Crystal Resonators," Proc. 21st Ann. Frequency Control Symp., US Army Electronics Command, Fort Monmouth, NJ 07703, April 1967, pp. 115-137.

31. G.K. Guttwein, T.J. Lukaszek, and A. Ballato, "Practical Consequences of Modal Parameter Control in Crystal Resonators," Technical Report ECOM-2847, US Army Electronics Command, Fort Monmouth, NJ 07703, June 1967, 21 pp.

32. J.F. Ziegler and W.A. Lanford, "Effect of Cosmic Rays on Computer Memories," Science, vol. 206, 16 November 1979, pp. 776-788.

33. T.C. May, "Soft Errors in VLSI: Present and Future," IEEE Trans. Components, Hybrids, and Mfg. Technol., vol. CHMT-2, No. 4, December 1979, pp. 377-387.

34. J.A. Woolley, L.E. Lamar, N.H. Stradley, and D.M. Harshbarger, "Low Alpha-Particle-Emitting Ceramics: Whats the Lower Limit?," IEEE Trans. Components, Hybrids, and Mfg. Technol., vol. CHMT-2, No. 4, December 1979, pp. 388-390.

35. S.W. Levine, "Alpha Emission Measurements of Lids and Solder Preforms on Semiconductor Packages," IEEE Trans. Components, Hybrids, and Mfg. Technol., vol. CHMT-2, No. 4, December 1979, pp. 391-395.

36. D.H. Phillips, "Cosmic Radiation Effects in Spacecraft Microelectronics: Part I," Military Electronics/Countermeasures, vol. 5, August 1979, pp. 88-92.

37. D.H. Phillips, "Cosmic Radiation Effects in Spacecraft Microelectronics: Part II," Military Electronics/Countermeasures, vol. 5, September 1979, pp. 87-93.

38. D.J. Redman, R.M. Sega, and R. Joseph, "Alpha Particle-Induced Soft Errors in Microelectronic Devices, Part I," Military Electronics/Countermeasures, vol. 6, March 1980, pp. 42-47.

39. D.J. Redman, R.M. Sega, and R. Joseph, "Alpha Particle-Induced Soft Errors in Microelectronic Devices, Part I," Military Electronics/ Countermeasures, vol. 6, April 1980, pp. 40-48.

40. D.N. Lapedes, Ed., Dictionary of Scientific and Technical Terms, McGraw-Hill, New York, 1974.

41. R. Bechmann, "Radiation Effects in Quartz - A Bibliography," Nucleonics, vol. 16, March 1958, pp. 122, 138.

42. T. Lukaszek and A. Ballato, "What SAW Can Learn From BAW: Implications for Future Frequency Control, Selection, and Signal Processing," Proc. IEEE Ultrasonics Symp., November 1980, pp. 173-183.


FILMED
4-8